



Description of the MIROC-ES2L Earth system model and evaluation of its climate–biogeochemical processes and feedbacks

5 Tomohiro Hajima¹, Michio Watanabe¹, Akitomo Yamamoto¹, Hiroaki Tatebe¹, Maki
A. Noguchi¹, Manabu Abe¹, Rumi Ohgaito¹, Akinori Ito¹, Dai Yamazaki², Hideki
Okajima¹, Akihiko Ito^{3,1}, Kumiko Takata³, Koji Ogochi¹, Shingo Watanabe¹, Michio
Kawamiya¹

10 ¹Research Center for Environmental Modeling and Application, Japan Agency for Marine-Earth Science and
Technology, 3173-25 Showamachi, Kanazawaku, Yokohama, Kanagawa 236-0001, Japan

²Research Center for Advanced Science and Technology, The University of Tokyo, Tokyo, 153-8505, Japan

³National Institute for Environmental Studies, Tsukuba, 305-8506, Japan

15 *Correspondence to:* Tomohiro Hajima (hajima@jamstec.go.jp)

Abstract

This study developed a new Model for Interdisciplinary Research on Climate, Earth System version2 for Long-term
simulations (MIROC-ES2L) Earth system model (ESM) using a state-of-the-art climate model as the physical core. This
20 model embeds a terrestrial biogeochemical component with explicit carbon–nitrogen interaction to account for soil
nutrient control on plant growth and the land carbon sink. The model’s ocean biogeochemical component is largely
updated to simulate biogeochemical cycles of carbon, nitrogen, phosphorus, iron, and oxygen such that oceanic primary
productivity can be controlled by multiple nutrient limitations. The ocean nitrogen cycle is coupled with the land
component via river discharge processes, and external inputs of iron from pyrogenic and lithogenic sources are considered.
25 Comparison of a historical simulation with observation studies showed the model could reproduce reasonable historical
changes in climate, the carbon cycle, and other biogeochemical variables together with reasonable spatial patterns of
distribution of the present-day condition. The model demonstrated historical human perturbation of the nitrogen cycle
through land use and agriculture, and it simulated the resultant impact on the terrestrial carbon cycle. Sensitivity analyses
in preindustrial conditions revealed modeled ocean biogeochemistry could be changed regionally (but substantially) by
30 nutrient inputs from the atmosphere and rivers. Through an idealized experiment of a 1%CO₂ increase scenario, we found
the transient climate response (TCR) in the model is 1.5 K, i.e., approximately 70% that of our previous model. The
cumulative airborne fraction (AF) is also reduced by 15% because of the intensified land carbon sink, resulting in an AF
close to the multimodel mean of the Coupled Model Intercomparison Project Phase 5 (CMIP5) ESMs. The transient
climate response to cumulative carbon emission (TCRE) is 1.3 K EgC⁻¹, i.e., slightly smaller than the average of the



35 CMIP5 ESMs, suggesting “optimistic” model performance in future climate projections. This model and the simulation results are contributing to the Coupled Model Intercomparison Project Phase 6 (CMIP6). The ESM could help further understanding of climate–biogeochemical interaction mechanisms, projections of future environmental changes, and exploration of our future options regarding sustainable development by evolving the processes of climate, biogeochemistry, and human activities in a holistic and interactive manner.

40

1. Introduction

Originally, global climate projections using climate models were based on simulations by atmosphere-only physical models (Manabe et al., 1965). Numerical climate models evolved through the integration or improvement of component models on ocean circulation (Manabe and Bryan, 1969), land hydrological processes (Sellers et al., 1986), sea ice
45 dynamics (e.g., Meehl and Washington, 1995), and aerosols (e.g., Takemura et al., 2000), most of which focus on physical aspects that affect how climate is formed. Cox et al. (2000) attempted to couple a carbon cycle model and a climate model to investigate the roles of biophysical and biogeochemical (carbon cycle) feedbacks on climate. Their results showing that such interactions are significant in projecting future climate aroused interest in the processes and feedbacks beyond those incorporated in traditional climate models. Models that incorporate biogeochemical processes, such as the one by Cox et al.
50 (2000), are often called Earth system models (ESMs). Currently, the most comprehensive state-of-the-art ESMs include component models of the land and ocean carbon cycle, atmospheric chemistry, dynamic vegetation, and other biogeochemical cycles (e.g., Watanabe et al., 2011, Collins et al., 2011).

Among many processes and possible interactions in the Earth system, the carbon cycle and its feedback on climate remain the focus of simulation studies using ESMs because of the importance of anthropogenic CO₂ as the primary driver
55 for climate change and the complexity of the natural carbon cycle that determines its fate. As ESMs simulate explicit climate–carbon interactions, ESMs can simulate the temporal evolution of atmospheric CO₂ concentration and the resultant climate change using anthropogenic CO₂ emissions as an input (Friedlingstein et al., 2006, 2014). It is also possible to make climate projections using prescribed CO₂ concentrations, and the diagnosed CO₂ fluxes in the simulations can be used for calculating the level of anthropogenic CO₂ emissions compatible with prescribed CO₂
60 pathways (Jones et al., 2013). Furthermore, simulation results can be diagnosed in terms of the relationship between anthropogenic CO₂ emissions and global temperature rise, i.e., the so-called transient climate response to cumulative carbon emissions (TCRE) (Allen et al., 2009; Matthews et al., 2009). The ESMs of the Coupled Model Intercomparison Project Phase 5 (CMIP5) revealed that the relationship is approximately linear (Gillett et al., 2013), which facilitates estimation of the total amount of anthropogenic CO₂ emissions to restrict global warming to below a specific mitigation
65 target.

The feedback of the carbon cycle on climate is manifest through regulation of the atmospheric CO₂ concentration, which can be decomposed into two feedback processes. The first process is the carbon cycle response to CO₂ increase. Elevated CO₂ concentration accelerates vegetation growth that intensifies the land carbon sink. In addition, increased levels of atmospheric CO₂ accelerate CO₂ dissolution into the surface water of the ocean, which eventually propagates into
70 the deeper ocean via ocean circulation and biological processes. Consequently, an increase of atmospheric CO₂ triggered by external forcing (e.g., anthropogenic emissions) can be mitigated partly by natural CO₂ uptake, forming a negative feedback loop between atmospheric CO₂ concentration and natural carbon uptake, i.e., the so-called CO₂–carbon feedback (Gregory et al., 2009) or carbon–concentration feedback (Boer and Arora et al., 2009). The second feedback process is the



75 carbon cycle response to global warming. Global warming induces loss of carbon from the land to the atmosphere by
accelerating ecosystem respiration (Arora et al., 2013; Todd-Brown et al., 2014; Friedlingstein et al., 2014), while ocean
surface warming reduces the solubility of CO₂ in seawater. Intensification of upper-ocean stratification and weakening of
the biological pump by global warming also prevent effective transportation of dissolved carbon into the deeper ocean
(Frölicher et al., 2015; Yamamoto et al., 2018). Global warming might lead to localized intensification of the natural
carbon sink (e.g., lengthening of the growing season and exposure of the ocean surface through melting of sea ice).
80 However, state-of-the-art ESMs have projected global natural carbon loss due to warming, suggesting a positive feedback
loop between climate change and natural carbon uptake, i.e., the so-called climate–carbon feedback (Friedlingstein et al.,
2006; Arora et al., 2013).

Quantification of the strength of the carbon cycle feedbacks and their comparison among ESMs were first made by
Friedlingstein et al. (2006), who showed that all ESMs agreed with the positive sign of the climate–carbon feedbacks for
85 both land and ocean. The latest comparison using CMIP5 ESMs was made by Arora et al. (2013). They found that the
widest spread between the models was in the land carbon response to CO₂ increase, while the second greatest spread was
in the land carbon response to warming. Two of the ESMs in their analysis employed explicit carbon–nitrogen (C–N)
interactions in the land component for considering the limitation of soil N on land CO₂ uptake, and these two models
showed the smallest land carbon response to CO₂ increase. Although it was pointed out later that the lowest response of
90 the two C–N models was not necessarily induced by N limitation (Hajima et al., 2014b), the comparison study by Arora et
al. (2013) aroused interest in terrestrial biogeochemical feedbacks other than the carbon cycle. The importance of N
limitation on the land carbon sink has also been suggested following simulation studies using offline land models (e.g.,
Thornton et al., 2007; Sokolov et al., 2008; Zaehle and Friend, 2010) and diagnostic analyses using the simulation output
of ESMs (e.g. Wieder et al., 2015).

95 Compared with land, the oceans showed better agreement among the CMIP5 ESMs (Arora et al., 2013) in terms of the
strength of both CO₂–carbon and climate–carbon feedbacks. However, the ESMs showed substantial discrepancies in the
spatiotemporal patterns of ocean CO₂ uptake, even in historical simulations. In particular, in the Southern Ocean, although
the models indicated dominance of the region in relation to anthropogenic carbon uptake (Frölicher et al., 2015), the
seasonality of the atmosphere–ocean CO₂ flux and the cumulative values in that region showed divergent patterns among
100 the models (Anav et al., 2013; Frölicher et al., 2015).

The ecological response of the ocean in ESMs remains far from certain. A benchmark study by Anav et al. (2013)
revealed that all CMIP5 ESMs underestimate net primary productivity (NPP) in the high latitudes of the Northern
Hemisphere, where seawater temperature and N availability likely limit primary production (e.g., Moore et al., 2013).
They also found that most models overestimate NPP in the Southern Hemisphere high latitudes, where nutrient supply is
105 sufficient because of strong upwelling but iron supply is limited (Moore et al., 2013). Globally, the CMIP5 ESMs simulate
NPP with different magnitudes, even in the preindustrial condition, and the global NPP response among the models to past
and future climate change is largely divergent (Laufkötter et al., 2015), as is the sinking particle flux (Fu et al., 2016).
Although such problems regarding oceanic NPP might be attributable partly to inaccurate reproduction of oceanic physical
fields by the models (Frölicher et al., 2015; Laufkötter et al., 2015), it is critical in simulations to reproduce accurately the
110 relative abundances of nutrients in the euphotic zone and their availability to microorganisms. In particular, nutrients in
the upper ocean are sustained by upwelling from the deeper ocean and nutrient inputs from external sources. Some studies
suggest that nutrient availability to marine ecosystems could decline in the future through reduction of nutrient upwelling
because of intensified stratification (e.g., Ono et al., 2008; Whitney et al., 2013; Yasunaka et al., 2016). Conversely, other



115 studies suggest that nutrient supply through atmospheric deposition and river discharge processes could be amplified in
the future because of human activities (Gruber and Galloway, 2008; Mahowald et al., 2009) unless robust mitigation
policies are adopted. Thus, to project the effects of biogeochemical feedback on climate, it is necessary to consider the
response of ecological processes to changing nutrient inputs as well as the response to climate change.

120 On the basis of the above, we previously reviewed the CMIP5 exercises and we discussed the perspective for new ESM
development (Hajima et al., 2014a). In our ESM development, we prioritized the incorporation of explicit C–N interaction
in the land biogeochemical component. The terrestrial nitrogen cycle regulates the carbon cycle by modulating soil
nutrient availability to plants, regulating leaf N concentration and photosynthetic capacity, and changing the C:N ratio in
plants and soils. In particular, CO₂ stimulation of plant growth (the so-called CO₂ fertilization effect) is the main driver of
terrestrial CO₂–carbon feedback, while N limitation on plant growth might regulate the feedback strength (Arora et al.,
2013; Hajima et al., 2014a; Hajima et al., 2014b). Thus, consideration of C–N coupling in the terrestrial ecosystem in an
125 ESM will enable change in the capacity of the land carbon sink following a change of N dynamics induced by human
perturbation (e.g., fertilizers) and/or atmospheric N deposition.

For the ocean, the biogeochemical component in our previous model (the MIROC-ESM; Watanabe et al., 2011) was
unchanged from that used for the first stage of the Coupled Climate Carbon Cycle Model Intercomparison Project
(C4MIP: Friedlingstein et al., 2006; Yoshikawa et al., 2008). The ocean component simulated C and N cycles only, using
130 simple parameterizations of ocean ecosystem dynamics with four types of N tracer and five C tracers (Watanabe et al.,
2011) with fixed C:N ratios of the organic components. Furthermore, the ocean N cycle in the model was closed to other
subsystems, i.e., there was no N input into the ocean (e.g., biological N fixation, atmospheric N deposition, and riverine N
input) or flux out of the system (e.g., outgassing and sedimentation). To account for changing inputs of N nutrients into
the ocean in the simulations, we gave second priority to the coupling of the ocean N cycle to other subsystems by
135 incorporating N exchange processes between the ocean and other components in the new ESM. The ocean N fixer (i.e.,
diazotrophs) can be regulated strongly by P availability (Shinozaki et al., 2018); therefore, inclusion of the ocean P cycle
should be adopted together with improvement of the N cycle. In addition, as the denitrification process is regulated
strongly by the level of oxygen in seawater, it was also decided to include the oxygen cycle in the new model. Inclusion of
the oxygen cycle provides potential to project future oceanic deoxygenation that is likely to threaten the habitable zone of
140 marine ecosystems, driven by changes in oxygen solubility, mixing, circulation, and respiration due to global warming
(Oschlies et al., 2018; Yamamoto et al., 2015).

The third priority in developing a new ESM was incorporation of Fe cycle processes. Fe is an essential micronutrient
for phytoplankton. Thus, any model lacking consideration of the Fe cycle potentially overestimates primary productivity,
especially in regions where subsurface macronutrient supply is enhanced but Fe availability is limited, e.g., the main
145 oceanic upwelling “high-nutrient, low-chlorophyll” regions (Martin and Gordon, 1988; Moore et al., 2013). Similar to the
N cycle, the ocean Fe cycle is also an open system. One of its main external sources is dissolved Fe from continental
margins and from hydrothermal vents along mid-ocean ridges (Tagliabue et al., 2017). Thus, continental and hydrothermal
Fe supply is important in terms of determining the background Fe concentration in seawater. In addition, the ocean Fe
cycle is also connected to the land through the atmosphere (Jickells et al., 2005; Mahowald et al., 2009; Ito et al., 2019).
150 Fe-containing aerosols are emitted from dry land surfaces, open biomass burning, and fossil fuel combustion, and they are
delivered to marine ecosystems via dry and wet deposition processes. These processes have been perturbed by climate
change, land use change (LUC), and air pollution (Jickells et al., 2005; Mahowald et al., 2009; Ito et al., 2019). Thus,



consideration of atmospheric Fe deposition in particular is necessary to reflect the anthropogenic impact on future marine ecosystem dynamics via Fe cycle processes.

155 Here, we present a description of a new ESM, the Model for Interdisciplinary Research on Climate, Earth System
version2 for Long-term simulations (MIROC-ESL2), which considers explicit carbon and nitrogen cycles for land, and
carbon, nitrogen, iron, phosphate, and oxygen cycles for the ocean. In the model, the biogeochemical components are
coupled interactively with physical climate components, enabling consideration of climate–biogeochemical feedbacks.
The model description and experimental settings are presented in Sect. 2. The basic performance of the model, evaluated
160 by executing a historical simulation and comparison of the results with observation-based studies, is presented in Sect. 3.1.
To evaluate the sensitivity of the biogeochemical processes, experiments for sensitivity analysis were performed and the
results compared with existent studies. In particular, global temperature response to cumulative anthropogenic CO₂
emissions in the new model was quantified and compared with that of the CMIP5 ESMs, to characterize the general
features of the new model in relation to existing ESMs. The results of the sensitivity analyses are presented in Sect. 3.2.
165 Finally, a summary and perspectives obtained from this study are summarized in Sect. 4.

2. Methods

2.1. Model configurations

To describe comprehensively the MIROC-ESL2 structure (Fig. 1), we first present the physical core of MIROC5.2,
170 which is an updated version of MIROC5 used for the CMIP5 exercises. Only a brief summary is presented here because a
detailed description on the modeling of MIROC5 can be found in Watanabe et al. (2010) and an account of a simulation
study performed by MIROC5.2 can be found in Tatebe et al. (2018). In addition, a description of MIROC6, which shares
almost the same structure and many of the characteristics of MIROC5.2, except for the atmospheric spatial resolution and
cumulus treatments, can be found in Tatebe et al. (2019). In this paper, description of the land and ocean biogeochemistry
175 is presented in detail because those two components represent the main modifications from the previous version of the
ESM (i.e., the MIROC-ESM; Watanabe et al., 2011).

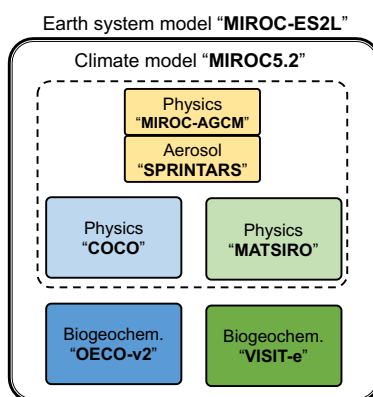


Figure 1



180 Schematic of component models in the new MIROC-ES2L Earth system model. The physical core of the model is
MIROC5.2, which consists of an atmospheric climate model (CCSR-NIES AGCM or MIROC-AGCM) with an aerosol
module (SPRINTARS), an ocean physics model (COCO) with a sea ice model, and a land physics model (MATSIRO)
with a river routine. The land biogeochemistry component (VISIT-e) simulates carbon and nitrogen cycles with an LUC
routine, and the ocean biogeochemistry component (OECO) simulates the cycles of carbon, nitrogen, iron, phosphorus,
185 and oxygen.

2.1.1. Physical core

190 The MIROC5.2 physical core comprises component models of the atmosphere, ocean, and land. The atmospheric
model is based on a spectral dynamical core, originally named the Center for Climate System Research–National Institute
for Environmental Studies atmospheric general circulation model (CCSR-NIES AGCM; Numaguchi et al., 1997), which is
coupled interactively with an aerosol component model called the Spectral Radiation-Transport Model for Aerosol
Species (SPRINTARS; Takemura et al., 2000, 2005). For the ocean, the CCSR Ocean Component (COCO) model
195 (Hasumi, 2006) is used in conjunction with a sea ice component model. For land, the Minimal Advanced Treatments of
Surface Interaction and Runoff (MATSIRO) model (Takata et al., 2003) is coupled to simulate the atmosphere–land
boundary conditions and freshwater input into the ocean. Considering the application possibility of the ESM to long-term
climate simulations of more than hundreds of years, e.g., paleoclimate studies (Ohgaito et al., 2013; Yamamoto et al.,
2019), the horizontal resolution of the atmosphere is set to have T42 spectral truncation, which is approximately 2.8°
200 intervals for latitude and longitude. The vertical resolution is 40 layers up to 3 hPa with a hybrid σ – p coordinate, as in
MIROC5. The horizontal coordination for the ocean is changed from the bipolar system employed in MIROC5 to a
tripolar system in MIROC5.2. The vertical levels are increased from 44 to 62 with a hybrid σ – z coordinate system. For
land, the same horizontal resolution as used for the atmosphere is employed, and the vertical soil structure of the model
has six layers down to the depth of 14 m. Subgrid fractions for two land use types (agriculture plus managed pasture and
205 others) are considered for the physical processes.

For the AGCM, the schemes used for the dynamical core, radiation, cumulus convection, and cloud microphysics are
mostly the same as in MIROC5; the major update of processes mainly concerns the aerosol module. The version used here
treats atmospheric organic matter (OM) as one of the prognostic variables, and emission of primary OM and precursors for
secondary OM are diagnosed in the component. For land, the scheme for subgrid snow distribution is replaced by one
210 incorporating a physically based approach (Nitta et al., 2014; Tatebe et al., 2019), and snow-derived wetland is newly
considered to reduce the hot bias found in the European region during spring–summer (Nitta et al., 2017; Tatebe et al.,
2019). The ocean and sea ice components are mostly the same as in MIROC5.

2.1.2. Land biogeochemical processes

215 The model of the land ecosystem/biogeochemistry component in MIROC-ES2L is the Vegetation Integrative Simulator
for Trace gases model (VISIT; Ito and Inatomi, 2012a). This model simulates carbon and nitrogen dynamics on land
(schematics can be found in Ito and Oikawa 2002 for the carbon cycle and Supplementary Fig. 1 for the nitrogen cycle). It



has been used for ecological studies of site–global scale (e.g., Ito and Inatomi, 2012b), impact assessments of climate change (e.g., Warszawski et al., 2013; Ito et al., 2016), prior to CO₂ flux inversion studies (e.g., Maksyutov et al., 2013; 220 Niwa et al., 2017), and contemporary assessments of CO₂, CH₄, and N₂O emissions in the Global Carbon Projects (Le Quéré et al., 2016; Saunois et al., 2016; Tian et al., 2018). The early version of the model (Sim-CYCLE; Ito and Oikawa, 2002) was actually used as the land carbon cycle component in the first stage of the C4MIP project (Friedlingstein et al., 2006; Yoshikawa et al., 2008). The model covers major processes relevant to the global carbon cycle. Photosynthesis or gross primary productivity (GPP) is simulated based on the Monsi–Saeki theory (Monsi and Saeki, 1953), which provides 225 a conventional scheme to simulate leaf-level photosynthesis in a semiempirical manner and for upscaling to canopy-level primary productivity. The allocation of photosynthate between carbon pools in vegetation (e.g., leaf, stem, and root) is regulated dynamically following phenological stages. Transfer of vegetation carbon into litter/soil pools is simulated using constant turnover rates and, in deciduous forests, seasonal leaf shedding occurs at the end of the growing period. The model focuses on biogeochemical processes and it does not explicitly simulate dynamic change in vegetation composition; 230 therefore, these processes are simulated using a static biome distribution. The carbon stored in litter (i.e., foliage, stem, and root litter) and humus (i.e., active, slow, and passive) pools is decomposed and released as CO₂ to the atmosphere, under the influence of soil water and temperature. Further details on the carbon cycle processes in the model can be found in Ito and Oikawa (2002).

For the nitrogen cycle, the model considers two major nitrogen influxes into the ecosystem: biological nitrogen fixation 235 (BNF) simulated based on the scheme of Cleveland et al. (1999) and external nitrogen sources such as fertilizer and atmospheric nitrogen deposition, which are prescribed in forcing data. The fluxes of nitrogen out of the land ecosystem are N₂ and N₂O production processed by nitrification and denitrification in soils, based on the scheme of Parton et al. (1996), leaching of inorganic nitrogen from soils, which is affected by the amount of soil nitrate and runoff rate, and NH₃ volatilization from soils (Lin et al., 2000; Thornley, 1998). Within the vegetation–soil system, organic nitrogen in the soil 240 is supplied from litter fall, whereas inorganic nitrogen is released through soil decomposition processes (soil mineralization) and stored as two chemical forms (NO₃⁻ and NH₄⁺). Inorganic nitrogen is taken up by plants, allocated to two vegetation pools (canopy and structural pools), and immobilized into a microbe pool. Finally, mineral nitrogen is lost via biotic/abiotic processes as mentioned above.

Although the original land component model covers most major carbon/nitrogen processes, for the purposes of 245 inclusion in the new ESM and making fully coupled climate–carbon/nitrogen projections, the land model was modified for this study (hereafter, the modified version is called VISIT-e). Thus, the modified model represents the tight interaction between carbon and nitrogen in plants. This is because the original model has only loose interaction between these two cycles and thus it cannot predict precisely the nitrogen limitation on primary productivity. To achieve this, the photosynthetic capacity in VISIT-e is modified to be controlled by the amount of nitrogen in leaves (leaf nitrogen 250 concentration), which is determined by the balance between the nitrogen demand of plants and potential supply from the soil. Thus, if sufficient inorganic nitrogen is not available for plants, leaf nitrogen concentration is gradually lowered, leading to the reductions of photosynthetic capacity and the plant production rate. This process is required to simulate the observed down-regulation in elevated CO₂ experiments (e.g., Norby et al., 2010; Zaehle et al., 2014). Other modifications regarding the nitrogen cycle are described in Appendix A.

255 Although the original VISIT incorporates LUC and associated CO₂ emission processes, to take full advantage of the latest LUC forcing dataset (Land-use harmonization 2; Ma et al., 2019), additional LUC-related processes have been newly introduced in VISIT-e. The model assumes five types of tile in each land grid (i.e., primary vegetation, secondary



260 vegetation, urban, cropland, and pasture) with the same structure of carbon/nitrogen pools. All processes are calculated separately for each tile (i.e., no lateral interaction), and then the variables in the tile are summed after weighting by the areal fraction of each land use type. The LUC impact is modeled assuming two types of land use impact on the biogeochemistry. The first impact considers status-driven LUC processes, which affect land biogeochemistry even when the areal fractions of the tiles are fixed. For example, even when a simulation is conducted with fixed areal fractions (e.g., a spin-up run under 1850 conditions), crop harvesting, nitrogen fixation by N-fixing crops, and the decay of OM in product pools occur. The second type of land use impact includes transition-driven processes that happen only when areal changes occur among the tiles. For example, when an areal fraction is changed within a year (e.g., conversion of forest to urban land use), carbon and nitrogen in the harvested biomass are translocated between product pools. When cropland is abandoned and the area is reclassified as secondary forest, the apparent mean mass density of secondary forest is first diluted because of the increase in less-vegetated area, and then secondary forest starts regrowth toward a new stabilization state. Further detailed description on LUC modeling is given in Appendix A.

270 The land ecosystem component runs with a daily time step in the ESM. It has fixed spatial distribution patterns of 12 vegetation categories (see Supplementary Fig. 2), and the land biogeochemistry is affected by daily averaged atmospheric conditions (CO_2 concentration, downward shortwave radiation, air temperature, and air pressure) and land abiotic conditions (soil water, soil temperature, and runoff rate as the base flow) simulated by the physical core of the ESM. In turn, daily averaged land variables simulated by VISIT-e are used by other components of the ESM. For example, the simulated leaf area index (LAI) is referenced in the physical core of the model to simulate physical dynamics on the land surface (e.g., evapotranspiration, albedo, and surface roughness). Furthermore, the rate of net atmosphere–land CO_2 fluxes is used in the calculation of the atmospheric CO_2 concentration, and inorganic N leached from the soil is transported rivers and subsequently used as an input of N nutrients to the ocean ecosystem. We note that the chemical state of N in rivers is assumed conserved during transportation, and that biogeochemical processes such as outgassing or sedimentation in freshwater systems are neglected in the present model. In addition, although the model can simulate terrestrial carbon loss by erosion and the dissolution of organic carbon in the ocean, to close the global mass conservation of carbon and nitrogen in simulations, the processes are forced to be inactive in this study. Finally, although N_2O and NH_3 emissions are simulated, the emission fluxes are simply diagnosed and they do not produce any changes in the atmospheric radiation balance or air quality.

285

2.1.3. Ocean biogeochemical processes

The new ocean biogeochemical component model OECO2 (see Supplementary Fig. 3 for a schematic), is a nutrient–phytoplankton–zooplankton–detritus-type model that is an extension of the previous model (Watanabe et al., 2011). Although only an overview of OECO2 is presented here, a detailed description can be found in Appendix B.

290 In OECO2, ocean biogeochemical dynamics are simulated based on 13 types of oceanic tracer. Three of them are associated with cycles of macronutrients (nitrate and phosphate) and a micronutrient (dissolved Fe). The model has four organic tracers of “ordinary” nondiazotrophic phytoplankton, diazotrophic phytoplankton (nitrogen fixer), zooplankton, and particulate detritus. All OM in these four tracers is assumed to have identical nutrient, oxygen, and micronutrient iron composition following the Redfield ratio concept with a constant elemental stoichiometric ratio for carbon, i.e., C:N:P:O = 106:16:1:138 (Takahashi et al., 1985) and C:Fe = $150 \cdot 10^{-3}$ (Gregg et al., 2003). Four other types of tracer are associated

295



with carbon and/or calcium, i.e., dissolved inorganic carbon (DIC), total alkalinity, calcium, and calcium carbonate. The two other tracers are oxygen and nitrous oxide.

The nitrogen cycle processes in OECO2 are similar to those in the previous version (Yoshikawa et al., 2008; Watanabe et al., 2011), except the new model accounts for nitrogen influxes such as nitrogen deposition from the atmosphere (as
300 external forcing), input of inorganic nitrogen from land via rivers, and BNF by diazotrophic phytoplankton. In addition, denitrification processes are also modeled as the dominant process of oceanic nitrogen loss, with explicit distinction between the gaseous forms of N₂O and N₂ (see below for nitrogen fixation and denitrification processes). Loss of nitrogen through the sedimentation process is also considered. The phosphorus cycle is newly embedded in the model to represent strong phosphorous limitation on the growth of diazotrophic phytoplankton. The structure of the phosphorus cycle is
305 generally similar to that of nitrogen, except the riverine input of phosphate is the only process that introduces phosphorus into the ocean. As the land ecosystem model cannot simulate the phosphorus cycle, the flux of phosphorous from rivers is diagnosed from the nitrogen flux, assuming that the phosphate brought to the river mouth satisfies the N:P ratio of 16:1, similar to the Redfield ratio.

The structure of the ocean iron cycle is also similar to that of nitrogen, except the following processes are modeled as
310 iron input into the ocean. Two major sources of iron deposition from the atmosphere are included in the new model: lithogenic and pyrogenic sources. Mineral dust emission is diagnosed by the aerosol component module, depending on the near-surface wind speed, soil dryness, and bare ground cover, while iron emitted from biomass burning and the consumption of fossil fuel and biofuel follows external forcing. The latter emission dataset used in this study is shown in Supplementary Fig. 4. The iron emissions from pyrogenic sources are estimated based on the iron content and emissions
315 of particulate matter (Ito et al., 2018). A shift from coal to oil combustion is considered in relation to shipping (Fletcher, 1997; Endresen et al., 2007). The iron content of mineral dust is prescribed at 3.5% (Duce and Tindale, 1991). The iron deposition from biomass burning is calculated from black carbon (BC) deposition and a ratio of 0.04 gFe gBC⁻¹ in fine particles at emission (Ito 2011). The emission, transportation, and deposition processes are simulated explicitly by the atmospheric aerosol component. The iron from different sources has different solubility in seawater and thus different
320 amounts of iron are available for phytoplankton. The solubility of iron is prescribed at 79% for oil combustion, 11% for coal combustion, and 18% for biomass burning (Ito, 2013). The solubility of iron for mineral dust is prescribed at 2% (Jickells et al., 2005).

In addition to the Fe input from the atmosphere, recent studies suggest contributions of Fe supply from sediment and hydrothermal vents to ecosystem activities (Tagliabue et al., 2017). The contributions of these two natural Fe sources to
325 the determination of atmospheric CO₂ concentration and export production are similar to or greater than that of dust (Tagliabue et al., 2014). Therefore, these three Fe sources are also considered in the new ESM (Appendix B).

Ocean ecosystem dynamics are simulated based on the nutrient cycles of nitrate, phosphorous, and iron. Nutrient concentration, in conjunction with the controls of seawater temperature and availability of light, regulates the primary productivity of the two types of phytoplankton. The model assumes that diazotrophic phytoplankton can prosper in regions
330 where phosphate is available but nitrate concentration is small (<0.05 μmol L⁻¹). In the model, zooplankton is assumed independent of abiotic conditions (e.g., seawater temperature) and dependent on biotic conditions (phytoplankton and zooplankton concentrations), as in the previous model. The denitrification process is modeled to occur only in suboxic waters (<5 μmol L⁻¹) (Schmittner et al., 2008) and it is suppressed in water with low nitrate concentration (<1 μmol L⁻¹). Detritus contains nitrate, phosphorus, iron, oxygen, and carbon, most of which is remineralized while sinking downward.



335 The detritus that reaches the ocean floor is removed from the system; however, a fraction of OM in the sediment is assumed to return to the bottom layer of the water column at a constant rate in each location (Kobayashi and Oka, 2018).

The ocean carbon cycle is formed by atmosphere–ocean CO₂ exchange, inorganic carbon chemistry, OM dynamics driven by marine ecosystem activities, and transportation and reallocation processes of ocean carbon within the interior. The formulations of atmosphere–ocean gas exchange, carbon chemistry, and related parameters follow protocols from the Ocean Model Intercomparison Project (OMIP; Orr et al., 2017). Production of DIC and total alkalinity is controlled by changes in inorganic nutrients and CaCO₃, following Keller et al. (2012).

345 Finally, the flux of dimethyl sulfide (DMS) from the ocean, which is produced by plankton and is a precursor of atmospheric sulfate aerosols, is diagnosed in the original aerosol module from the surface downward shortwave radiation flux. In MIROC-ES2L, this emission scheme is modified and the flux is calculated from the sea surface DMS concentration that is diagnosed from the simulated surface water chlorophyll concentrations and the corresponding mixed-layer depth (Appendix B). In the present model, this is the only pathway via which ocean biogeochemistry affects climate, except for atmosphere–ocean CO₂ exchange.

2.2. Experiments, forcing, and metrics

350 2.2.1. Experiments and forcing

To evaluate the performance and sensitivities of MIROC-ES2L, we conducted four groups of experiments comprising eleven experiments in total (Tables 1 and 2). The first group was a control run that consisted of two types of experiment: a normal control run (CTL) in which the external forcing was set to preindustrial conditions and an alternative control run (CTL-D) used for sensitivity analysis of the ocean biogeochemistry, which is described later.

355 The second group, used for historical simulations, consisted of three types of experiment during the period 1850–2014. All three experiments were driven by the Coupled Model Intercomparison Project Phase 6 (Eyring et al., 2016) official forcing datasets (version 6.2.1; details on forcing datasets used in the simulations are summarized in Appendix C), and the CO₂ concentration was prescribed in the simulations (i.e., so-called concentration-driven experiments). The first comprised a conventional historical simulation (HIST), and the simulation result is used for direct comparison with observation-based studies to evaluate model performance. The second was a special experiment named HIST-NOLUC, designed for evaluation of the impact of LUC on the climate and biogeochemistry. In this experiment, land use and agricultural management (fertilizer application) were fixed at preindustrial levels. This experimental configuration is the same as the LUMIP experiment in CMIP6 named land-noLu (Lawrence et al., 2016). The third experiment (HIST-BGC) was the same as HIST, except only carbon cycle processes detect the CO₂ increase (named in C4MIP of CMIP6 as hist-bgc; Jones et al., 2016). Thus, there was no CO₂-induced global warming in the experiment.

360 The third experimental group was used to evaluate the climate and carbon cycle feedbacks. This group comprised three types of idealized experiment, following experimental designs proposed by Eyring et al. (2016) and Jones et al. (2016). In the three experiments, CO₂ concentration was prescribed to increase at the rate of 1.0% per year from the preindustrial state throughout the 140-year period (i.e., the concentration finally reached a value of approximately 1140 ppmv), while other external forcing was maintained at the preindustrial condition. The three experiments were configured as follows: (1) 370 IPPY: a normal experiment in which both climate and biogeochemical processes respond to the CO₂ increase; (2) IPPY-BGC: the same as IPPY but only carbon cycle processes detect the CO₂ increase; and (3) IPPY-RAD: the same as IPPY



but only atmospheric radiation processes detect the CO₂ increase. In 1PPY-BGC, carbon cycle processes respond to the CO₂ increase without CO₂-induced global warming; thus, the result of this simulation is used to quantify CO₂-carbon feedback. In 1PPY-RAD, as there is no direct CO₂ stimulation on the carbon cycle, climate change is the only cause of carbon cycle variation. Thus, this simulation result is utilized for evaluating climate-carbon feedback.

The final group comprised a set of experiments for evaluating ocean biogeochemistry, focusing mainly on the processes newly introduced in MIROC-ES2L. This group consisted of three types of experiment. The first experiment (NO-NR) was configured similarly to the CTL run, except the ocean component did not receive any riverine N input. Through this experiment, the impact of riverine N on ocean biogeochemistry could be evaluated. The second experiment (NO-NRD) was the same as NO-NR, except atmospheric N deposition additionally had no effect on ocean biogeochemistry. By evaluating the difference between NO-NR and NO-NRD, the impact of nitrogen deposition on ocean biogeochemistry could be evaluated. The final experiment (NO-FD) was configured with atmospheric Fe deposition onto the ocean surface switched off. To detect slight signals of ocean biogeochemistry arising from switching off the three processes (i.e., riverine N, N deposition, and Fe deposition), it was necessary to maintain consistency in the ocean physical fields between the experiments because a slight difference of the ocean physical fields produces perturbation on ocean biogeochemistry, which would be noise in the analyses. In MIROC-ES2L, ocean DMS emission is the feedback process of ocean biogeochemistry on the atmospheric physical processes; thus, biogeochemical change induced by the switching-off manipulations must change the DMS emission, leading to inconsistency in the physical fields between the experiments. To avoid this occurrence, the DMS emission scheme in all three experiments was reverted to that used in the original aerosol component model, which is independent of the ocean ecosystem state (Appendix B). Similarly, the special control run (CTL-D), which was based on CTL, also had the DMS emission scheme changed to the same as NO-NR, NO-NRD, and NO-FD.

For conducting the experiments described above, preindustrial spin-up was performed in advance. Land and ocean biogeochemical components were decoupled from the ESM, and the spin-up run was conducted for 3000 years for the ocean component and 30,000 years for land, by prescribing model-derived physical fields and other external forcing for the component models. In the final phase of the spin-up procedure, continuous spin-up, forced by the 1850-year condition of CMIP6 forcing, was performed for the entire system for 2483 years (Supplementary Fig. 5). All the experiments listed in Table 1 were initiated from the final condition of this spin-up procedure.

Table 1

Summary of details of the experiments.



Experimental Group	Experiment	Purpose	Configurations	Duration [yrs]
Control	CTL	Control run	CO ₂ conc. and other forcings are fixed at pre-industrial level	165
	CTL-D	Control run for NO-NR, NO-NRD, and NO-FD	Same as CTL, but DMS emission follows the scheme of original aerosol module	100
Historical	HIST	Evaluation of model performance	Following CMIP6-DECK historical run	165 (1850-2014)
	HIST-NOLUC	Evaluation of land-use change impact on carbon cycle	LUC and fertilizer are fixed at pre-industrial level	165 (1850-2014)
	HIST-BGC	Evaluation of response of carbon cycle to CO ₂ increase	Same as HIST but only biogeochemical processes "see" the CO ₂ increase	165 (1850-2014)
1%CO ₂	1PPY	Evaluation of sensitivities of climate and carbon	Prescribed CO ₂ increased with 1.0 [% yr ⁻¹]	140
	1PPY-BGC	Evaluation of response of carbon cycle to CO ₂ increase	Same as 1PPY but only biogeochemical processes "see" the CO ₂ increase	140
	1PPY-RAD	Evaluation of response of carbon cycle to climate change	Same as 1PPY but only atmospheric radiative processes "see" the CO ₂ increase	140
OBGC	NO-NR	Evaluation of impacts of riverine N to ocean	Same as CTL-D but ocean doesn't get impact from riverine N	100
	NO-NRD	Evaluation of impacts of deposition N to ocean, by combining with NO-NR	Same as NO-NR but ocean doesn't get impact from Fe deposition	100
	NO-FD	Evaluation of impacts of deposition Fe to ocean	Same as CTL-D but ocean doesn't get impact from de position	100

405 **Table 2**

Biogeochemical configurations in experiments, summarized as biogeochemical process settings. Bold characters represent the major differences between experiments within an experimental group.

Experimental Group	Experiments	Impact on Land/Ocean BGC ^a			Impact on Ocean BGC [†]			DMS scheme [‡]
		CO ₂	Climate	LUC	River N	Dep. N	Dep. Fe	
Control	CTL	–	–	–	O	O	O	TypeA
	CTL-D	–	–	–	O	O	O	TypeB
Historical	HIST	O	O	O	O	O	O	TypeA
	HIST-NOLUC	O	O	–	O	O	O	TypeA
	HIST-BGC	O	–	O	O	O	O	TypeA
1%CO ₂	1PPY	O	O	–	O	O	O	TypeA
	1PPY-BGC	O	O	–	O	O	O	TypeA
	1PPY-RAD	O	–	–	O	O	O	TypeA
OBGC	NO-NR	–	–	–	–	O	O	TypeB
	NO-NRD	–	–	–	–	–	O	TypeB
	NO-FD	–	–	–	O	O	–	TypeB

*If the biogeochemical process in an experiment was affected by CO₂, climate, or land use change, the letter "O" is present; otherwise, the symbol "–" is used.



†If the ocean biogeochemistry process detected fluxes of riverine nitrogen, atmospheric nitrogen deposition, or atmospheric iron deposition, the letter “O” is present; otherwise, the symbol “–” is used.

‡The TypeA DMS emission scheme is the default scheme in MIROC-ES2L, where DMS emission is simulated as being dependent on the ocean biogeochemical status and the mixed-layer depth. TypeB is a scheme employed in the original aerosol component model in which DMS emission is calculated as independent of ocean status.

2.2.2. Evaluation of climate and carbon cycle response to CO₂

To evaluate the climate and carbon cycle response to CO₂ increase, we used the metrics of transient climate response (TCR), airborne fraction of CO₂ (AF), and TCRE, which have been utilized previously to characterize the entire climate–carbon cycle response to CO₂ increase in other models (Matthews et al., 2009; Hajima et al., 2012; Gillett et al., 2013). Similar analysis is made in this study and the result is presented in Sect. 3.2.

First, TCRE is defined as the ratio of global mean near-surface air temperature change (T) to cumulative anthropogenic carbon emission (CE) at the level of doubled CO₂ concentration from the preindustrial state (hereafter, 2xCO₂^{PI}):

$$\text{TCRE} = T/\text{CE}, \quad (1)$$

which can be written as follows:

$$\text{TCRE} = (\text{CA}/\text{CE}) \times (T/\text{CA}), \quad (2)$$

where CA is the atmospheric carbon increase until reaching 2xCO₂^{PI}. The first factor on the right-hand side (CA/CE) is identical to the definition of the cumulative airborne fraction of anthropogenic carbon emission:

$$\text{CA}/\text{CE} = \text{AF}. \quad (3)$$

The second factor (T/CA) can be represented by TCR as follows:

$$T/\text{CA} = \text{TCR}/\text{CA}, \quad (4)$$

which is because TCR is defined as T at 2xCO₂^{PI}. Thus, Eq. 2 can be expressed as follows:

$$\text{TCRE} = \text{AF} \times (\text{TCR}/\text{CA}). \quad (5)$$

The result of the 1PPY simulation was used to evaluate TCRE, TCR, and AF. As CA is prescribed in the simulation, CE can be diagnosed by CE = CA + CL + CO, where CL and CO represent the change in land and ocean carbon storage, respectively. As shown in Matthews et al. (2009), AF summarizes the carbon cycle response to anthropogenic CE. The second factor in Eq. 5 (TCR/CA) captures the global climate response to CO₂ increase in the models. TCRE quantifies the entire climate–carbon cycle response to anthropogenic CO₂ emission in the model.

To evaluate the strength of carbon cycle feedbacks in the model, the feedback strength is quantified by the so-called β and γ quantities (Friedlingstein et al., 2006; Arora et al., 2013). The former is a feedback parameter for CO₂–carbon feedback (carbon cycle response to CO₂ increase), which can be calculated as follows:

$$\beta_L = (\text{CL}^{\text{1PPY-BGC}} - \text{CL}^{\text{CTL}})/\text{CA}^{\text{1PPY}}, \quad (6)$$

$$\beta_O = (\text{CO}^{\text{1PPY-BGC}} - \text{CO}^{\text{CTL}})/\text{CA}^{\text{1PPY}}, \quad (7)$$



where subscripts L and O represent land and ocean, respectively, and the superscripts represent the experiment used for
445 the calculation.

The quantity γ is a feedback parameter for climate–carbon feedback (carbon cycle response to climate change), which
can be calculated using the results of the 1PPY-RAD and CTL simulations:

$$\gamma_L = (CL^{1PPY-RAD} - CL^{CTL})/CA^{1PPY}, \quad (8)$$

$$\gamma_O = (CO^{1PPY-RAD} - CO^{CTL})/CA^{1PPY}. \quad (9)$$

450

3. Results and discussion

3.1. Model performance in historical simulation

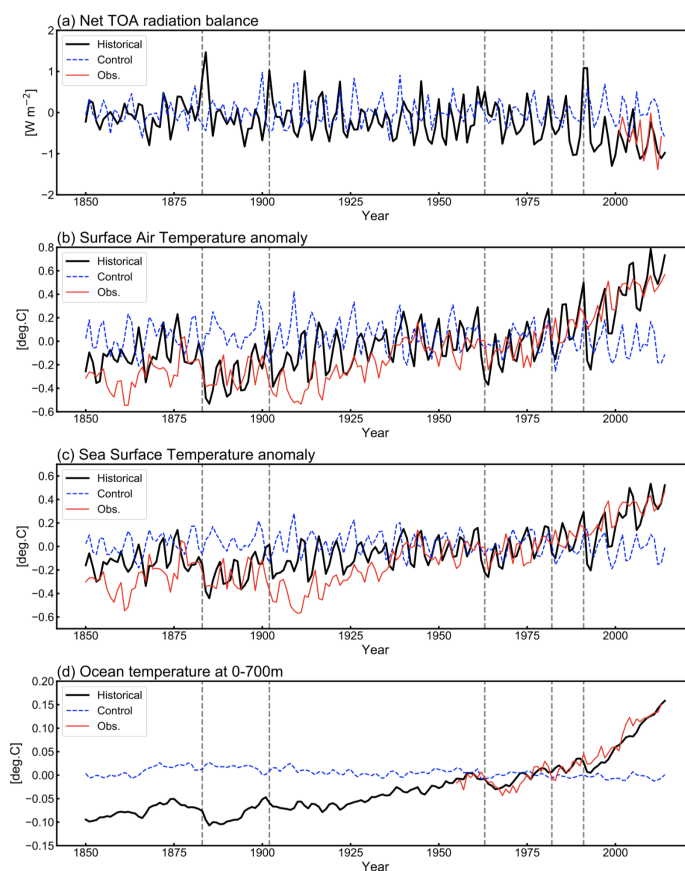
3.1.1. Global climate: net radiation balance and global temperature

To evaluate the physical fields reproduced by MIROC-ES2L, the temporal evolutions of the global mean net radiation
balance at the top of atmosphere (TOA), near-surface air temperature (SAT), sea surface temperature (SST), and upper-
ocean (0–700 m) temperature were compared with observation datasets and the results are shown in Fig. 2. The model
simulates a reasonably steady state of net TOA radiation balance in the CTL run, showing a trend of $-4.6 \times 10^{-5} \text{ W m}^{-2} \text{ yr}^{-1}$
during the 165-year period. When comparing net TOA radiation balance of the HIST simulation with satellite
460 measurement (CERES EBAF-TOA edition 4.0, constrained by in situ measurements; Loeb et al., 2012, 2018), the model
result is -0.63 W m^{-2} (negative means net incoming radiation) during 2001–2010, which is within the range of -0.5 ± 0.43
 W m^{-2} estimated by Loeb et al. (2012) for the corresponding period (Fig. 2a).

Following the net increase of incoming radiation, the SAT anomaly becomes larger in the latter half of the 20th century
(Fig. 2b). The warming trend during 1951–2011 is simulated as 0.1 K per decade, which is consistent with that of
465 HadCRUT4 (version 4.6; Morice et al., 2012) of 0.11 K per decade (Stocker et al., 2013). Observation datasets of SST
(HadSST version 3.1.1; Kennedy et al., 2011) and upper-ocean temperature (Levitus et al., 2012) clearly display
increasing trends in the corresponding period, which are reproduced successfully by the model (Fig. 2c and 2d). In
addition to the warming trend in the latter half of the 20th century, the model captures the slowdown of SAT increase both
in the 1950s and in the 1960s. These changes are likely induced by increased anthropogenic aerosol emissions and
470 resultant cooling through indirect aerosol effects, together with cooling attributable to large volcanic eruptions in the
1960s (Wilcox et al., 2013; Nozawa et al., 2005). However, distinct discrepancies between the model result and
HadCRUT4 are found for SAT and SST, in the 1860s and particularly in the 1900s. This might be due to inevitable
asynchronization between the simulation and observations on the phasing of the internal variability of climate. Kosaka et
al. (2016) reported that there should have been four major cooling events due to tropical Pacific variability in the 20th
475 century, one of which was found in the 1900s. They reported the other three events were around 1940, 1970, and 2000;
however, discrepancies arising from these three events are not so evident in this study, likely because of the single
ensemble simulation. It is also confirmed that the model exhibits short-term response of the TOA radiation balance
following episodic volcanic events (Fig. 2a, vertical dashed lines), with resultant cooling of SAT and SST (Fig. 2a–c) and
further propagation into the deeper ocean with extended cooling duration (Fig. 2d). Overall, the historical SAT increase in
480 MIROC-ES2L, taking the difference between the average of 1850–1900 and 2003–2012, is 0.69 K, while the HadCRUT4-



485 based estimate by Stocker et al. (2013) is 0.78 K for the corresponding period. It is considered that the model shows good performance in reproducing global physical fields. This is likely attributable to the inherited robust performance of the physical core of the model (MIROC5.2), because MIROC-ES2L has only two feedback pathways of biophysical processes on climate (DMS emission from the ocean and terrestrial processes associated with LAI dynamics) when the model is driven by a prescribed CO₂ concentration. Both processes are likely to change the physical fields locally.



490 **Figure 2**

Comparison of HIST simulation results by MIROC-ES2L with observations: (a) net radiation balance at the top of the atmosphere (TOA; upward positive), (b) global mean surface air temperature, (c) global mean sea surface temperature, and (d) global mean ocean temperature at 0–700 m depth. Black, red, and blue lines represent historical simulations, historical observations, and pi-control simulations, respectively. Vertical dashed lines represent the timing of major volcanic eruptions (i.e., Krakatau (1883), Santa Maria (1902), Agung (1963), El Chichon (1982), and Pinatubo (1991)). In panel (a), the simulation results are presented as anomalies from the 1850–2014 average of the CTL run. In panels (b), (c),



and (d), the results are presented as the anomaly from the 1961–1990 averages. Observation data for the radiation balance were obtained from the global product of CERES EBAF-TOA edition 4.0. Observation data for SAT and SST were obtained from HadCRUT4 (Morice et al., 2012) version 4.6 and HadSST (Kennedy et al., 2011) version 3.1.1, respectively. Ocean temperature anomaly, updated from Levitus et al. (2012), is used for the comparison of ocean temperature at 0–700 m depth during the period 1955–2014.

3.1.2. Global carbon budget

The simulated net CO₂ uptake by land and ocean in cumulative values (i.e., changes in total carbon of land and ocean) is shown in Fig. 3a and 3b, respectively. For land, the CTL run shows slight reduction of carbon of 7.6 PgC during the 165 years (i.e., 4.6 PgC per century), which is within the acceptable range for the CMIP6 exercise (10 PgC per century; Jones et al., 2016). The dashed gray line in Fig. 3a is the result from HIST-NOLUC, showing a natural land carbon sink in MIROC-ES2L of 166 PgC during 1850–2014. This is well comparable with the estimate of 185 ± 50 PgC by Le Quéré et al. (2018) for the same period (vertical gray bar in Fig. 3a), which was obtained from multiple offline terrestrial ecosystem models with fixed land use. In addition, LUC is one of the factors to change drastically the historical land carbon amount, because positive (negative) LUC emission is linked directly with reduction (increase) of land carbon. Based on bookkeeping methods, Le Quéré et al. (2018) estimated the cumulative CE derived from LUC during 1850–2014 as 195 ± 75 PgC, whereas the simulated cumulative emission by MIROC-ES2L that is diagnosed by the difference in land carbon amount between HIST-NOLUC and HIST is 156 PgC.

Through being affected by both environmental and LUCs, MIROC-ES2L demonstrates in the HIST simulation that land carbon is reduced by approximately 60 PgC from the beginning of the simulation up until the middle of the 20th century (black line in Fig. 3a). This reduction should reflect LUC during this period because HIST-NOLUC does not show such a trend of decrease in the corresponding period (dashed gray line in Fig. 3a). From the 1960s, the model shows continuous carbon sequestration on land, resulting in positive net CO₂ uptake of 2.4 PgC yr⁻¹ in the 2000s (Table 3). This continuous increase in the latter half of the 20th century is due to the combined effects of CO₂ fertilization, vegetation recovery associated with LUC, and the increase of nitrogen input via deposition and the use of fertilizer. This is displayed clearly in Fig. 3c, where the historical land carbon change is decomposed into the responses to (1) CO₂ increase (blue line, diagnosed by “HIST-NOLUC + HIST-BGC – HIST”; see Table 2), (2) climate change (red line, by “HIST – HIST-BGC”), and (3) LUC (green line, by “HIST – HIST-NOLUC”). In the latter half of the 20th century, land carbon sequestration accelerated by CO₂ stimulation is clear, while climate change and the resultant terrestrial carbon loss also become evident. In addition, land carbon reduction induced by LUC is slightly alleviated in the corresponding period. During the historical period, MIROC-ES2L simulates total land carbon change of 44 PgC. This number drops to within the range of -10 ± 90 PgC (vertical black bar in Fig. 3a), where estimation uncertainties arising from both the terrestrial natural carbon sink and LUC emission by Le Quéré et al. (2018) are considered (calculated as $(\sigma_{\text{LUC}}^2 + \sigma_{\text{SINK}}^2)^{0.5}$, where σ_{LUC} and σ_{SINK} represent the uncertainty range of LUC emission and the land sink, respectively, in Le Quéré et al., 2018).

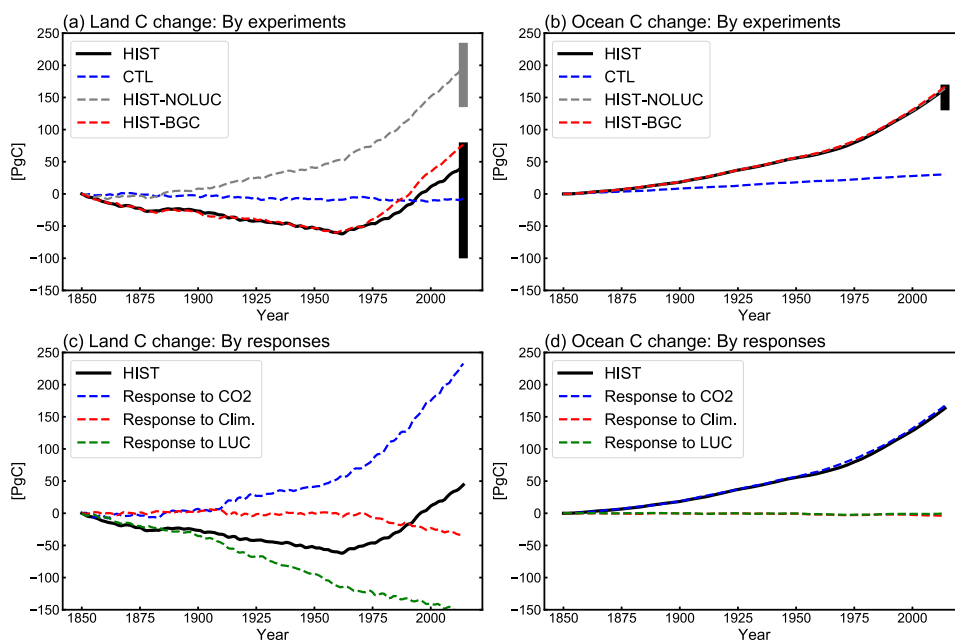
For the ocean, the model shows a trend of increase of carbon accumulation in the CTL run (Fig. 3b). This is partly due to carbon removal by the sedimentation process that is newly introduced into MIROC-ES2L. In this process, an amount of carbon is extracted from the ocean bottom, which should be compensated by an equivalent input of carbon from the atmosphere through gas exchange processes. In the CTL run, the rate of carbon extracted from the ocean bottom is 0.068 PgC yr⁻¹ (Table 4), suggesting that the process removes 11 PgC throughout the entire simulation period of CTL (165



years). It is noted that Cias et al. (2013) suggested that the ocean was a net source of CO₂ in the preindustrial era to an amount of 0.7 PgC yr⁻¹, whereas our model shows it as a net sink in the same condition. This is likely attributable to the lack of a process of riverine carbon input in our model. For example, Cias et al. (2013) estimated that rivers obtain an external input of carbon of 0.9 PgC yr⁻¹ from the lithosphere, of which 0.2 PgC yr⁻¹ is removed by sedimentation and 0.7 PgC yr⁻¹ is lost to the atmosphere via gaseous exchange. The sedimentation process cannot explain all of the increase of oceanic carbon in the CTL run (30 PgC). Therefore, the remainder should be attributed to other reasons, e.g., the shortness of the spin-up period or imperfect mass conservation in the component model.

The HIST run shows the cumulative carbon uptake by the ocean, which is driven predominantly by CO₂ increase (Fig. 3b and 3d). In comparison with land, ocean carbon shows a relatively small response to climate change (red line in Fig. 3d), which is consistent with analysis of the carbon cycle feedback in an idealized scenario (Arora et al., 2013). Furthermore, the model shows weak or almost no response against LUC (green line in Fig. 3d), although the ocean component in the model actually receives increased nitrogen input from rivers attributable to LUC and agriculture (Fig. 4, Table 4). It suggests that the increase of riverine nitrogen input due to LUC and agriculture would not have had global-scale impact on ocean carbon uptake in the historical period. The model simulates cumulative carbon uptake of 163 PgC for 1850–2014, which is within the range of 150 ± 20 PgC (vertical black bar in Fig. 3b) reported by Le Quéré et al. (2018).

Overall, MIROC-ES2L qualitatively captures well the temporal evolution of carbon dynamics in the historical period, and the cumulative carbon uptake by both land and ocean is within the range of the estimates by Le Quéré et al. (2018). However, the model might overestimate net carbon uptake by the land and/or ocean, or underestimate LUC emissions, because the diagnosed CO₂ concentration in the HIST run is 376 ppmv (Appendix D), which is lower (by 22 ppmv) than that actually monitored. This bias of diagnosed CO₂ concentration might be alleviated partially if the model were driven by anthropogenic CO₂ emissions, because in the emission-driven mode, lower atmospheric CO₂ concentration can weaken the land/ocean sink through the negative CO₂–carbon feedback. In addition, in the emission-driven mode, land and ocean are mutually interlinked via the atmospheric CO₂ concentration; thus, strong bias of CO₂ flux in one component can be modulated by the other. This mechanism might reduce the bias of CO₂ fluxes of land and ocean simultaneously, or it might exacerbate CO₂ flux by imposing the flux bias of one onto the other. For more detail, simulations and analyses based on emission-driven configurations are necessary, as designed in C4MIP (Jones et al., 2016).



565

Figure 3

Land and ocean carbon change (i.e., cumulative net carbon uptake by land and ocean) in historical simulations. Upper panels present simulation results of historical (HIST, black lines), historical without land-use change (HIST-NOLUC, 570 dashed gray), historical without global climate change (HIST-BGC, dashed red), and control (CTL, dashed blue) runs. For land calculation, carbon amount change in product pools for land use is taken into account. Vertical bars represent uncertainty ranges estimated from Le Quéré et al. (2018). Black bars correspond to HIST (1850–2014) run result, and gray bar represents the uncertainty range for natural carbon sink of land, which corresponds to HIST-NOLUC run in this study. In lower panels, HIST run result is shown again (black lines) together with decomposed response of land/ocean carbon 575 against CO₂ increase (dashed blue), climate change (dashed red), and LUC (dashed green). Note that the ocean in MIROC-ES2L takes into account carbon removal via sedimentation process onto ocean floor; thus, the model exhibits continuous carbon uptake, even in the CTL experiment.

Table 3

580 Key variables of global land biogeochemistry: preindustrial condition (165 years) and the 2000s in the historical run (HIST).

*1: Net carbon uptake is calculated as the net ecosystem productivity minus the carbon emissions from product pools for land use.

*2: BNF by agriculture is also included.

585 *3: Net nitrogen uptake is calculated by annual changes in total nitrogen storage.



	Preindustrial	2000s
Gross primary productivity (PgC yr ⁻¹)	108.8	123.8
Net primary productivity (PgC yr ⁻¹)	57.7	67.2
Heterotrophic respiration (PgC yr ⁻¹)	56.9	59.4
Net carbon uptake* ¹ (PgC yr ⁻¹)	0.0	2.4
Vegetation carbon (PgC)	538.4	543.3
Soil organic carbon (PgC)	1484.2	1491.0
Biological fixation* ² (TgN yr ⁻¹)	97.2	135.9
Deposition (TgN yr ⁻¹)	19.6	65.5
Fertilizer (TgN yr ⁻¹)	0.0	114.0
N ₂ emission (TgN yr ⁻¹)	71.5	110.8
N ₂ O emission (TgN yr ⁻¹)	9.5	13.7
NH ₃ emission (TgN yr ⁻¹)	1.9	19.5
N leaching (TgN yr ⁻¹)	17.3	33.4
Net ecosystem nitrogen uptake* ³ (TgN yr ⁻¹)	0.7	37.0
Vegetation nitrogen (PgN)	4.0	3.9
Soil total nitrogen (PgN)	74.9	75.3

Table 4

590 Key global ocean biogeochemical fluxes and concentrations under preindustrial control simulation and the 2000s.

	Preindustrial	2000s
Net primary productivity (PgC yr ⁻¹)	28.3	28.6
Sinking particulate organic carbon at 100 m (PgC yr ⁻¹)	7.8	7.9



Nitrogen fixation (TgN yr ⁻¹)	129.1	125.9
Nitrogen deposition (TgN yr ⁻¹)	14.2	35.2
Riverine nitrogen input (TgN yr ⁻¹)	17.5	33.9
Denitrification (TgN yr ⁻¹)	142.2	164.5
N ₂ O emission (TgN yr ⁻¹)	4.5	4.4
Nitrogen flux into the sediment (TgN yr ⁻¹)	0.012	0.013
N cycle imbalance (TgN yr ⁻¹)	14.1	26.1
Atmosphere–ocean CO ₂ flux (PgC yr ⁻¹)	-0.15	-2.37
Carbon flux into sediment (PgC yr ⁻¹)	0.068	0.073
Mean O ₂ concentration (mmol m ⁻³)	191	189.9
Hypoxic volume (10 ¹⁵ m ³ ; [O ₂] < 80 mmol m ⁻³)	34.2	34.3
Suboxic volume (10 ¹⁵ m ³ ; [O ₂] < 5 mmol m ⁻³)	2.3	2.7

3.1.3. Global nitrogen budget

595 MIROC-ES2L can simulate the global nitrogen cycle under interaction with climate and the carbon cycle, and the
 global N budget of land and ocean in the HIST simulation is shown in Fig. 4 as component fluxes. Comparison of the
 terrestrial nitrogen budget in the 2000s with the preindustrial condition (Table 3) reveals the inputs of nitrogen via
 deposition and fertilizer, which are controlled by forcing data, increase by 46 and 114 TgN yr⁻¹, respectively. In addition,
 BNF is also increased by 40% (39 TgN yr⁻¹), which is caused by areal expansion of agriculture for N-fixing crops (Fig. 4,
 600 Supplementary Fig. 6). Previous studies have shown similar levels of increase. For example, Gruber and Galloway (2008)
 reported a value of 35 TgN yr⁻¹, and the absolute magnitude of agricultural BNF in the present-day condition was
 estimated as 50–70 TgN yr⁻¹ by Herridge et al. (2008) and 40 TgN yr⁻¹ by Galloway et al. (2008).

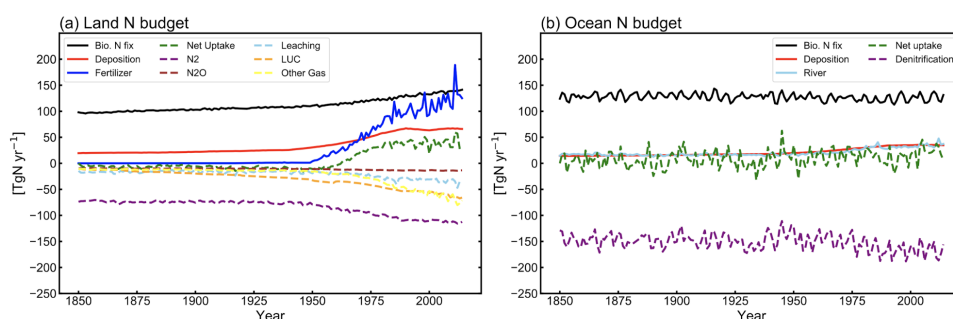
For terrestrial nitrogen efflux, Gruber and Galloway (2008) reported N₂ emission in the unperturbed state was 100 TgN
 yr⁻¹, i.e., larger than found in this study (72 TgN yr⁻¹). However, in the present-day condition, they estimated the absolute
 605 magnitude of N₂ emission as 115 TgN yr⁻¹, which is reasonably close to our model result (111 TgN yr⁻¹). MIROC-ES2L
 simulates the historical increase of N₂O emission from soil as 4.5 TgN yr⁻¹ from the preindustrial condition to the 2000s,
 which is comparable with the estimate of approximately 4 TgN yr⁻¹ for 1861–2015 derived from a model comparison
 study (Tian et al., 2018). However, the absolute magnitude of terrestrial N₂O emission fluxes in preindustrial and present-
 day conditions are likely overestimated (Table 3; Hashimoto, 2012).

610 Although it is difficult to obtain observation-based estimates on how much nitrogen was accumulated by the land
 ecosystem in the historical period, the model demonstrates net nitrogen uptake by land in the 2000s as 37 TgN yr⁻¹ (Table



3). This positive uptake is likely caused by increased total nitrogen input into the land ecosystem, as well as increased nitrogen demand by plants and soils under elevated CO₂ concentrations. Actually, 1PPY-BGC, in which nitrogen deposition, fertilizer application, and global warming are forced to maintain preindustrial levels and where only CO₂ perturbs the biogeochemistry, shows net increase of total nitrogen in the land ecosystem (data not shown), suggesting atmospheric CO₂ increase stimulates ecosystem nitrogen demand. We note that the model demonstrates nitrogen loss by LUC at a rate of >50 TgN yr⁻¹ (Fig. 4). It is because the harvested biomass in the model is translocated to product pools, and the nitrogen contained in the biomass is assumed lost with implicit chemical form, together with carbon loss as CO₂.

Compared with land, the model simulates relatively stable dynamics of the oceanic nitrogen budget but with larger interannual variation (Fig. 4b). In the 2000s, oceanic BNF is simulated as 126 TgN yr⁻¹, which is almost at the same level (slightly below) that of the preindustrial state, i.e., 129 TgN yr⁻¹ (Table 4). This number is close to previously reported estimates of approximately 130 TgN yr⁻¹ (Eugster and Gruber, 2012). The invariant behavior of BNF in the model suggests the historical change in nitrogen input into the ocean is attributable primarily to two external sources: deposition and riverine input. Nitrogen deposition into the ocean, which is prescribed in the forcing data, shows an increase from 14 TgN yr⁻¹ in the preindustrial condition to 35 TgN yr⁻¹ in the 2000s. Riverine nitrogen input is shown to increase from 18 TgN yr⁻¹ in the preindustrial condition to 34 TgN yr⁻¹ in the 2000s (this is discussed further in Sect. 3.1.6 and Sect. 3.2.3). In this study, the gross nitrogen input into the ocean in the present-day condition is simulated as 195 TgN yr⁻¹. The value is reasonably close to the estimate of 200 TgN yr⁻¹ by Wang et al. (2019) and that of 209 TgN yr⁻¹ by Galloway et al. (2004); however, it is smaller than other published estimates (e.g., 294 TgN yr⁻¹; Codispoti et al. (2001) and 270 TgN yr⁻¹; Gruber and Galloway (2008)). Denitrification, the main source of ocean nitrogen loss, is simulated as 142 TgN yr⁻¹ for the preindustrial condition and 165 TgN yr⁻¹ for the 2000s. These values are within the wide range of total denitrification rate estimated by previous studies, i.e., 145–450 TgN yr⁻¹ (Eugster and Gruber, 2012). It should be noted that the present model used in this study does not include sedimentary denitrification. Thus, the expected N flux by sedimentary denitrification is imposed on water-column denitrification, and the rate of water-column denitrification is likely overestimated. Overall, the model exhibits oceanic N imbalance of 26.1 TgN yr⁻¹ in the present-day condition (Fig. 4, Table 4).



640 **Figure 4**

Global nitrogen budget of (a) land and (b) ocean in the HIST simulation. Solid lines represent the nitrogen input into the land/ocean, and dashed lines represent its fate. Positive (negative) values mean flux into (out of) the land/ocean. In



645 panel (a), BNF (black line) takes into account both natural and agricultural fluxes. LUC (dashed orange line) is an emission derived from the decay of LUC-product pools. Other gases (yellow line) represent the sum of NH₃ emission and flux from abiotic sources. For the ocean, denitrification (purple line) includes both N₂ and N₂O emissions. The rate of nitrogen loss by the sedimentation process onto the ocean floor is not shown in the figure because of the small size of the flux (<0.015 TgN yr⁻¹). All nitrogen gas emissions are diagnosed and thus have no effect on the radiative balance in the atmosphere or on air quality change.

650 3.1.4. Climate: atmosphere and ocean physical fields

Here, we present an overview of the performance of the mean state of the physical fields, atmosphere, and land/oceanic basic variables of the model in comparison with various observational based data. The variables examined here are SAT, precipitation, SST, sea ice concentration and land snow cover, and mixed-layer depth, all of which are representative physical states associated with biogeochemical processes. Shown in Fig. 5 is the climatology of SAT (air temperature at 2-
655 m height) averaged over 1989–2009 for annual, December–February (DJF), and June–August (JJA) means, and the biases in comparison with the ERA-Interim dataset (Dee et al., 2011). The comparison suggests that the model performs well (biases <2°C) over the tropics and most of the global area in terms of both annual mean and seasonality. However, obvious warm biases exist over the Southern Ocean and Antarctica. This is a general tendency of state-of-the-art general circulation models, and both MIROC5 (Watanabe et al., 2010) and MIROC6 (Tatebe et al., 2019) also suffer this problem.
660 The warm bias in the Southern Ocean can be attributed to the difficulty of expressing cloud cover in the region (Hyder et al., 2018) and poor representations of the mixed-layer depth and deep convection in the open ocean attributable to the lack of modeled mesoscale processes in the Antarctic Circumpolar Current (Tatebe et al., 2019). A related warm bias in SST over the Southern Ocean is also confirmed, which is discussed later.

665

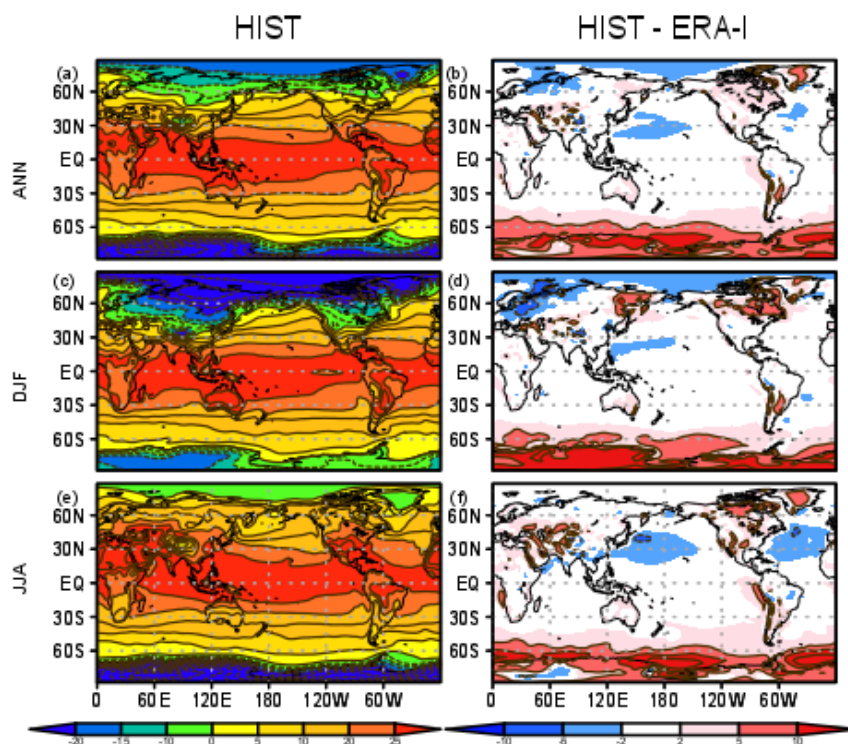


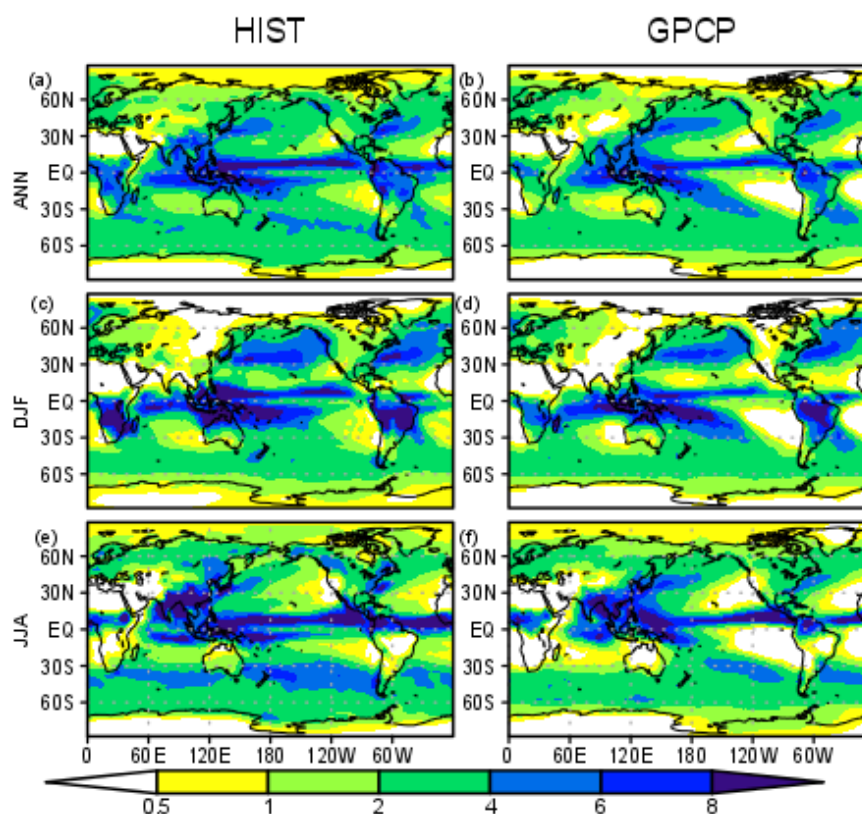
Figure 5

Air temperature at 2-m height ($^{\circ}\text{C}$) in the HIST simulation presented as 1989–2009 climatology and the bias compared with the ERA-Interim dataset (Dee et al., 2011) for (a) and (b) annual, (c) and (d) DJF, and (e) and (f) JJA means.

670

Figure 6 shows the precipitation distribution in the HIST experiment in comparison with the Global Precipitation Climatology Project (GPCP) dataset (Adler et al., 2003). In general, the precipitation distribution is reasonably well represented in the model. The Intertropical Convergence Zone (ITCZ) is reproduced well in the experiment, except that the simulated South Pacific Convergence Zone is shifted equatorward relative to the GPCP, which is the so-called double ITCZ syndrome (Bellucci et al., 2010). Over continental areas, the model is effective in capturing the spatial pattern of both the annual mean precipitation and the seasonality. However, positive precipitation biases are evident in arid and semiarid regions of central Asia, Australia, Africa, and the western side of North America.

675



680 **Figure 6**

Precipitation distributions (mm d^{-1}) in the HIST simulation and GPCP dataset, (Adler et al., 2003) for (a) and (b) annual, (c) and (d) DJF, and (e) and (f) JJA means averaged over 1981–2000.

It is important to represent SST well in terms of simulating climate change (Ohgaito and Abe-Ouchi, 2009) and reproducing biogeochemical fields on the ocean surface. Figure 7 presents the modeled SST and bias in comparison with the World Ocean Atlas 2013 (WOA2013; Locarnini et al., 2013). Generally, the model performs well, confirmed by the large extent of the area with minimal bias (colored white in Fig. 7). However, obvious bias is evident, e.g., the warm bias in the Southern Ocean, as already explained above (Fig. 5). A cold bias is also evident over the northwestern Pacific Ocean, which is attributable partially to the mixed layer being too deep (as shown in Fig. 9). One other possible reason for this bias is the resolution of the model being too coarse to reproduce properly the Western Boundary Currents and their extensions.

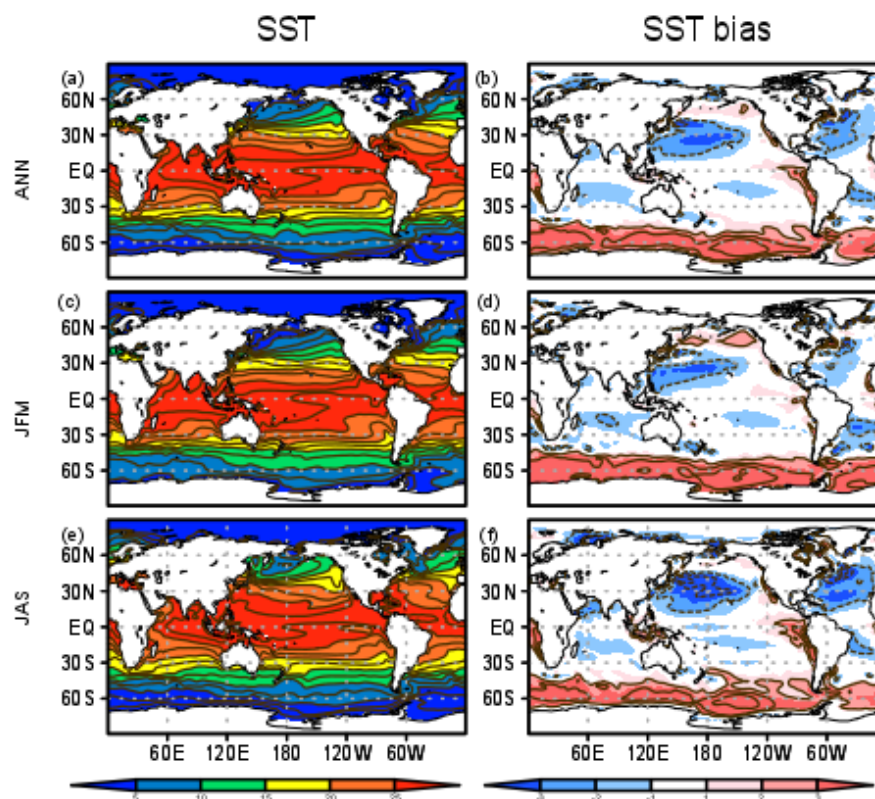
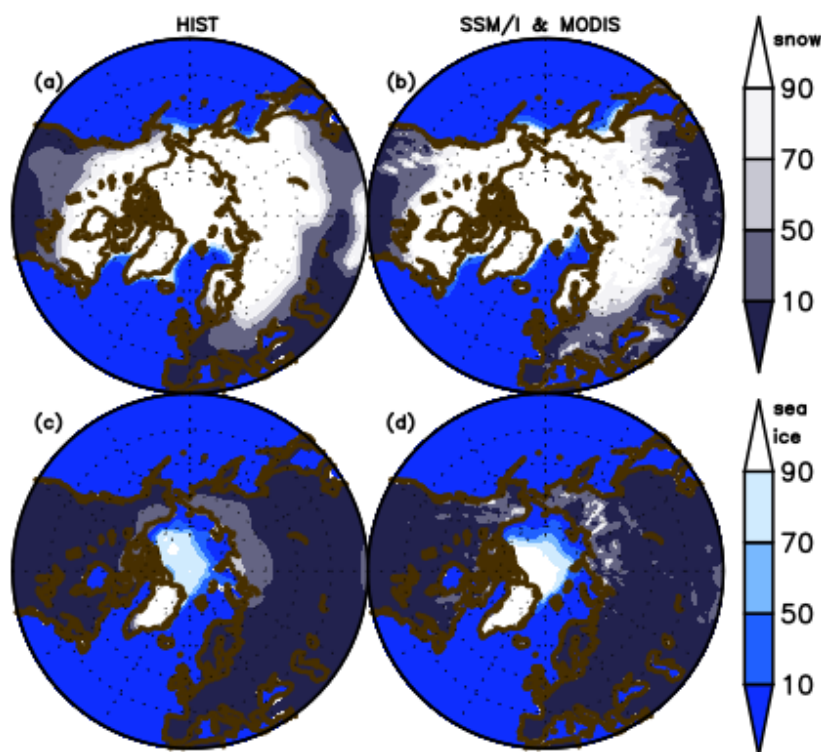


Figure 7

695 SST (°C) in the HIST simulation presented as 1955–2012 climatology and the bias in comparison with WOA2013
(Locarnini et al., 2013) for (a) and (b) annual, (c) and (d) JFM, and (e) and (f) JAS means.

The model performance in simulating sea ice concentration and snow cover over land for both March and September is shown in Fig. 8, in comparison with observational data (Special Sensor Microwave Imager (SSM/I; Kaleschke et al.,
700 2001) for sea ice concentration and Moderate-resolution Imaging Spectroradiometer (MODIS; Hall et al., 2006) for snow cover). Sea ice extent is represented well for both months, although the summertime concentration peak is slightly smaller than observed. The extent of the snow-covered area is also represented well, likely owing to the updated scheme for subgrid snow representation (Nitta et al., 2014; Tatebe et al., 2019). However, the fine structure of the snow cover is lost in the simulation, which is likely attributable to the coarse resolution of the modeled atmosphere and land. The reasonable
705 performance in reproducing land snow seasonality also implies reasonable performance in reproducing LAI seasonality in the boreal region, because snowmelt (accumulation) and leaf flush (shedding) processes are associated with each other (Supplementary Fig. 7).



710

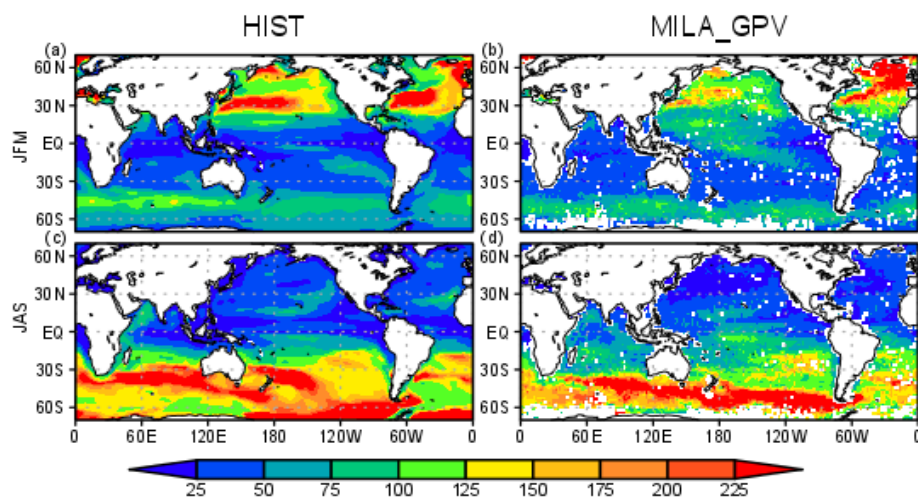
Figure 8

Northern Hemisphere sea ice concentration and land snow fraction (%) in the HIST simulation presented as 2003–2013 climatology and in comparison with SSM/I (Kaleschke et al., 2001) and MODIS (Hall et al., 2006) data for (a) and (b) March and (c) and (d) September.

715

Figure 9 shows the mixed-layer depth in comparison with the Mixed-Layer dataset of Argo, Grid Point Value (MILA_GPV; Hosoda et al., 2010). It is confirmed that the HIST simulation captures well both the spatial pattern and the seasonality change in mixed-layer depth. In the Northern Hemisphere winter, the structure of the deep mixed layer over the western North Pacific Ocean is consistent with observations, although the actual depth is overestimated. There could be various reasons for such discrepancy, e.g., wind stress or ocean temperature profile. The deep mixed layer in the high-latitude regions of the North Atlantic Ocean is also consistent with observations. In addition, the shallow mixed layer in low latitudes is generally captured well by the simulation, and the depth that is maintained at around 100 m over the Southern Ocean is consistent with observations. In austral winter, MILA_GPV shows the mixed layer develops to more than 200 m over the Indian Ocean and the Pacific sector of the Southern Ocean, whereas it is shallow (around 50 m) in the tropics and the Northern Hemisphere (Fig. 9d). The model captures the general pattern in austral winter, although the extent of the simulated deeper mixed-layer depth of more than 200 m in the Southern Ocean is larger than that of MILA_GPV (Fig. 9c).

725



730

Figure 9

Mixed-layer depth (m) in the HIST simulation presented as 2000–2010 climatology and comparison with MILA_GPV data set (Hosoda et al., 2010) for (a) and (b) JFM and (c) and (d) JAS means.

735 3.1.5. Land biogeochemistry

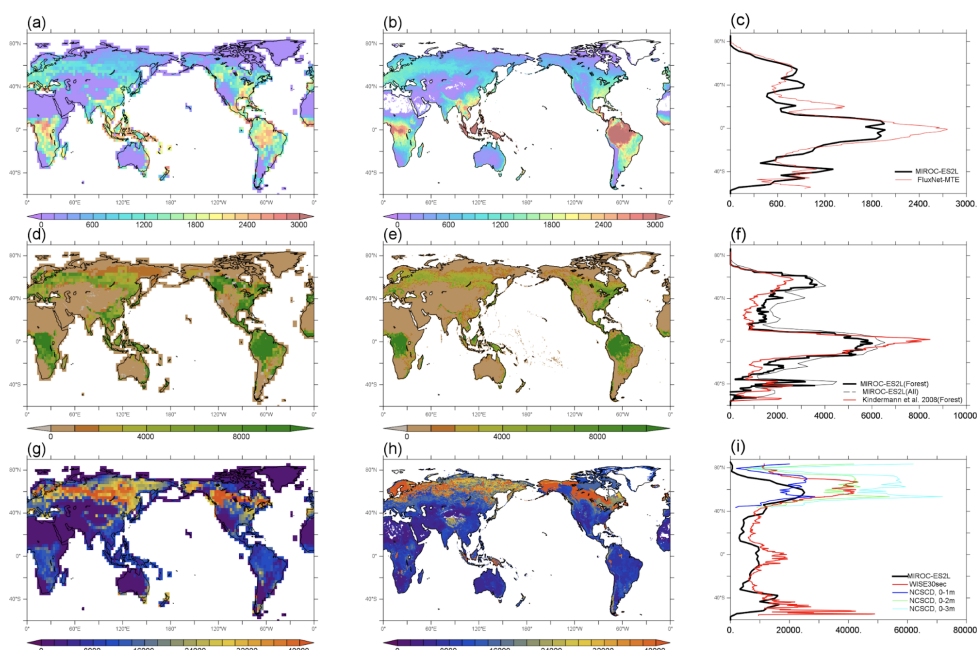
Model performance in relation to land biogeochemistry is evaluated based on the spatial distributions of three fundamental variables of the land carbon cycle in comparison with observation-based products. First, GPP in the HIST simulation is compared with the global product by Jung et al. (2011) (Fig. 10a–c). The model simulates higher productivity (>2000 gC m⁻²) in the tropical forests of central Africa, Southeast Asia, and Southern America, although the productivity in these regions is generally underestimated in comparison with the observation-based product. This underestimation is likely attributable to the use of the parameter values of photosynthetic capacities (K_{PSAT1} and K_{PSAT2} in Appendix A) from Kattge et al. (2009). This is because Kattge et al. (2009) also showed such substantial depression of photosynthetic capacity in the tropics. The model captures well the moderate productivity of vegetation in savanna regions such as the eastern side of South America and the marginal region surrounding central Africa. Moderate GPP is also found in the Northern Hemisphere in the region 20°–45°N, where a large proportion of land cover is dominated by both natural and agricultural vegetation (Supplementary Fig. 2). The GPP gradient from moderate to lower GPP in boreal to tundra regions of Eurasia and North America is captured well by the model. The model estimates global GPP at 124 PgC yr⁻¹ in the 2000s (Table 3), which is within the range of 106–140 PgC yr⁻¹ produced by the CMIP5 ESMs and is reasonably close to the value of 119 PgC yr⁻¹ derived from an observation product (1986–2005 average; Anav et al., 2013).

750 To evaluate the simulated vegetation carbon, we compare the model results of forest carbon, not total vegetation carbon, with those of Kindermann et al. (2008) (Fig. 10d–f). The model reproduces the reasonably high density of biomass in tropical forests, although the values are smaller than the observation product (Fig. 10f). This is attributable partly to the



underestimation of GPP in this region, as described above. In high-latitude regions of the Northern Hemisphere (around 50°N), the model overestimates biomass density, particularly in terms of the evergreen coniferous forests that extend across western Siberia and North America. Considering the GPP in these regions is captured reasonably well by the model (Fig. 10a and 10b), the overestimation of boreal forest biomass is likely due to the underestimated turnover rate of forest carbon. Slight overestimation of biomass is also found in the region where intensive cultivation has occurred, i.e., Europe, Southeast–East Asia, and eastern America. The model estimates global vegetation carbon including all types of vegetation at 543 PgC (Table 3).

In Fig. 10g–i, the model results of soil organic carbon (SOC) are compared with two different types of SOC product: harmonized soil property values for broadscale modeling (WISE30sec) by Batjes (2016) and NCSCDv2 by Hugelius et al. (2013). The former is a global dataset that represents soil column SOC down to the depth of 2 m, whereas the latter targets only the high-latitude region of the Northern Hemisphere at different soil depths (~1, ~2, and ~3 m). Comparison with WISE30sec confirms that the model successfully captures the spatial distribution of lower carbon accumulation in arid and tropical regions and higher SOC in boreal regions in the Northern Hemisphere. However, the simulated zonal mean SOC in the boreal regions is about half that of WISE30sec (Fig. 10i). This is likely attributable to different treatment of the vertical profile of SOC, i.e., WISE30sec covers the total SOC down to 2 m depth, while the model simulates SOC dynamics with an implicit vertical profile, considering only the difference of upper SOC as litter form and lower SOC as humus. The model result in the boreal region is comparable with the NCSCDv2 estimation for 1-m depth. We note, as mentioned by Todd-Brown et al. (2012), large uncertainty remains in the estimation of SOC amount, especially in boreal regions. Globally, SOC is simulated as 1491 PgC (Table 3) in this study, which is smaller than the value of 2060 ± 215 PgC of WISE30sec (Batjes, 2016) but comparable with the range of 890–1660 PgC, as estimated by Todd-Brown et al. (2012) based on the Harmonized World Soil Database v1.2 (FAO/IIASA/ISRIC/ISS-CAS/JRC, 2012).



775



Figure 10

Comparison of carbon flux and storage of the land ecosystem between the HIST simulation by MIROC-ES2L and an observation-based dataset. Upper panels show comparison of GPP ($\text{gC m}^{-2} \text{yr}^{-1}$) averaged over 1982–2011: (a) model result, (b) FluxNet-MTE of Jung et al. (2011), and (c) zonally averaged distributions. Middle panels show vegetation carbon (gC m^{-2}): (d) model result of forest carbon (obtained by masking the total vegetation carbon where forest coverage is $<5\%$), (e) forest carbon estimated by Kindermann et al. (2008), and (f) zonally averaged distributions, where solid black and red lines represent forest carbon, and the dashed thin line is the total vegetation carbon simulated by the model. Lower panels show SOC: (g) model result, (h) observation-based product of harmonized soil property values for broadscale modeling (WISE30sec) by Batjes (2016), and (i) zonally averaged distributions, where the model result and WISE30sec are shown by black and red lines, respectively. Blue, green, and light blue lines in panel (h) are NCSCDv2 by Hugelius et al. (2013), which is an independent estimate of SOC in the high-latitude region of the Northern Hemisphere at different soil depths (blue: 0–1 m, green: 0–2 m, and light blue: 0–3m).

3.1.6. Ocean biogeochemistry

In this section, we evaluate the simulated surface and vertical distributions of nitrate, phosphate, dissolved Fe, NPP, oxygen, DIC, and alkalinity against observations (Fig. 11). The observations comprise the World Ocean Atlas 2013 (WOA2013; Garcia et al., 2014a, 2014b) for macronutrients and oxygen, GEOTRACES dataset (updated to its 2015 version; Tagliabue et al., 2012) for dissolved iron, Global Ocean Data Analysis Project version 2 (GLODAPv2; Lauvset et al., 2016) for DIC and alkalinity, and SeaWiFS (Behrenfeld and Falkowski, 1997) satellite observations for NPP.

The simulated surface distributions of nitrate and phosphate are generally in agreement with the WOA2013 datasets (Fig. 11a and 11b). The surface macronutrient concentrations in high nitrate, low chlorophyll (HNLC) regions (e.g., the Southern Ocean, North Pacific Ocean, and eastern equatorial Pacific Ocean) are higher than produced by the ocean biogeochemical component of our previous model (Watanabe et al., 2011) and they are more consistent with observed values. This increase of macronutrients in HNLC regions is reasonable because implementation of both the iron cycle and the iron limitation on phytoplankton growth can reduce macronutrient utilization in these regions. Ocean circulation influences the distribution of nutrient concentrations. In the Southern Ocean, the deep mixed-layer depths simulated by the model can cause overestimation of entrainment of nutrients to the surface water and thus produce high nutrient bias (Fig. 9). The simulated vertical nitrate concentrations compare reasonably well with observed values (Fig. 11a). This is the result of the near balance between nitrogen cycle sources (i.e., nitrogen fixation, atmospheric nitrogen deposition, and riverine nitrogen input) and sinks (i.e., denitrification, N_2O emission, and sedimentary loss) over the long spin-up period.

The concentration of dissolved iron in the open ocean is highest in the subtropical North Atlantic Ocean and in the Arabian Sea (Fig. 11c), which is consistent with the pattern observed in GEOTRACES. Such high concentrations are caused by enhanced dust deposition from the Sahara Desert. In the remainder of the open ocean, dissolved iron concentrations are generally $<0.2 \mu\text{mol m}^{-3}$, especially in HNLC regions. The model captures well the main observed patterns in the surface ocean. The very high iron concentrations ($>1 \mu\text{mol m}^{-3}$) both observed and simulated along coasts and over continental margins are the result of iron input from sediment. The average simulated dissolved Fe concentration in the surface ocean (0–100 m) is $0.39 \mu\text{mol m}^{-3}$, which is lower than observed ($0.52 \mu\text{mol m}^{-3}$) but within the range of the iron model intercomparison project (FeMIP; Tagliabue et al., 2016). One factor not accounted for in our model is the



815 variation in the solubility of iron in aerosols, which depend not only on the source chemical composition but also on
atmospheric processing during transport (Ito et al., 2019). Consideration of different degrees of atmospheric Fe processing
could reduce the overestimations of dissolved Fe concentration in the North Atlantic Ocean and North Pacific Ocean (Ito
et al., accepted). Our model also neglects variations in sedimentary iron flux. Observations found iron release or burial in
820 sediment is dependent on the oxygen concentration of bottom water (Noffke et al., 2012), ambient temperature (Sanz-
Lázaro et al., 2011), and amount of OM that reaches the sea floor and is remineralized therein (Elrod et al., 2004). To
simulate more realistic iron distributions, these processes should be considered in future studies.

Reproducing the spatial pattern of nutrient limitation on phytoplankton growth is crucial for accurate prediction of
primary production and for reflecting in the simulations the consequences of ongoing anthropogenic perturbations to
oceanic nutrient cycles (Moore et al., 2013). The model reasonably reproduces the HNLC regions because of the iron
825 limitation in the subarctic North Pacific Ocean, equatorial Pacific Ocean, and Southern Ocean (Supplementary Fig. 8),
although the subarctic North Pacific Ocean and equatorial Pacific have larger HNLC zones than observed upwelling
regions. This is likely due to underestimation of surface iron concentrations and/or a relatively high half-saturation
constant for iron uptake (Appendix B). Nitrogen limitation occurs throughout much of the surface low-latitude ocean
where nitrogen supply from the subsurface is relatively slow.

830 Based on the distribution pattern of nutrients and the limitations, annual NPP is simulated as 28.6 PgC yr^{-1} (Table 4).
This value is lower than a satellite-based estimate of $35\text{--}78 \text{ PgC yr}^{-1}$ (Carr et al., 2006) and it is also lower than the range
of $30.9\text{--}78.7 \text{ PgC yr}^{-1}$ derived from the CMIP5 models (Bopp et al., 2013). This is likely attributable to the high half-
saturation constant for iron uptake, as mentioned above. Although intense primary productivity in coastal regions is not
resolved by the coarse grid, the modeled NPP agrees with the basin-scale patterns of observation-based NPP. The values
835 of both modeled and observed NPP are high in regions of equatorial upwelling, the North Atlantic Ocean, and the
Southern Ocean north of the polar front, whereas they are low in subtropical gyres (Fig. 11g). Global export production is
estimated as 7.9 PgC yr^{-1} , which is the upper bound of the CMIP5 models ($4.9\text{--}7.9 \text{ PgC yr}^{-1}$; Bopp et al., 2013).

Simulated surface distribution of dissolved oxygen compares reasonably well with observations (not shown). This is
because the surface oxygen concentration is close to its solubility value and it is strongly constrained by SST. At depth,
840 oxygen minimum zones (OMZs) in the eastern equatorial Pacific Ocean, eastern tropical Atlantic Ocean, Arabian Sea, and
Bay of Bengal are reproduced well (Fig. 11f). However, the model produces oxygen concentration values higher than
observed; thus, it underestimates the hypoxic volume ($[\text{O}_2] < 80 \text{ mmol m}^{-3}$) by a factor of three in comparison with data-
based estimates (Bianchi et al., 2012). Note that existing global ocean biogeochemical models have difficulty in
reproducing OMZs owing to coarse resolution and simple globally tuned parameterizations of vertical fluxes of OM
845 (Cocco et al., 2013; Bopp et al., 2013). The positive bias in oxygen might be driven by wintertime mixing in the Southern
Ocean and North Pacific Ocean that is too intense (Fig. 9) and transports too much surface oxygen to depth.

The model also captures the global-scale patterns of observed DIC and alkalinity (Fig. 11d and 11e). High values of
these parameters in subtropical gyres (and also in the Southern Ocean for DIC) are found in the model output and
observations. Overestimation of alkalinity in subtropical gyres leads to overestimation of DIC because alkalinity affects
850 the capacity of the ocean to take up and store atmospheric CO_2 .

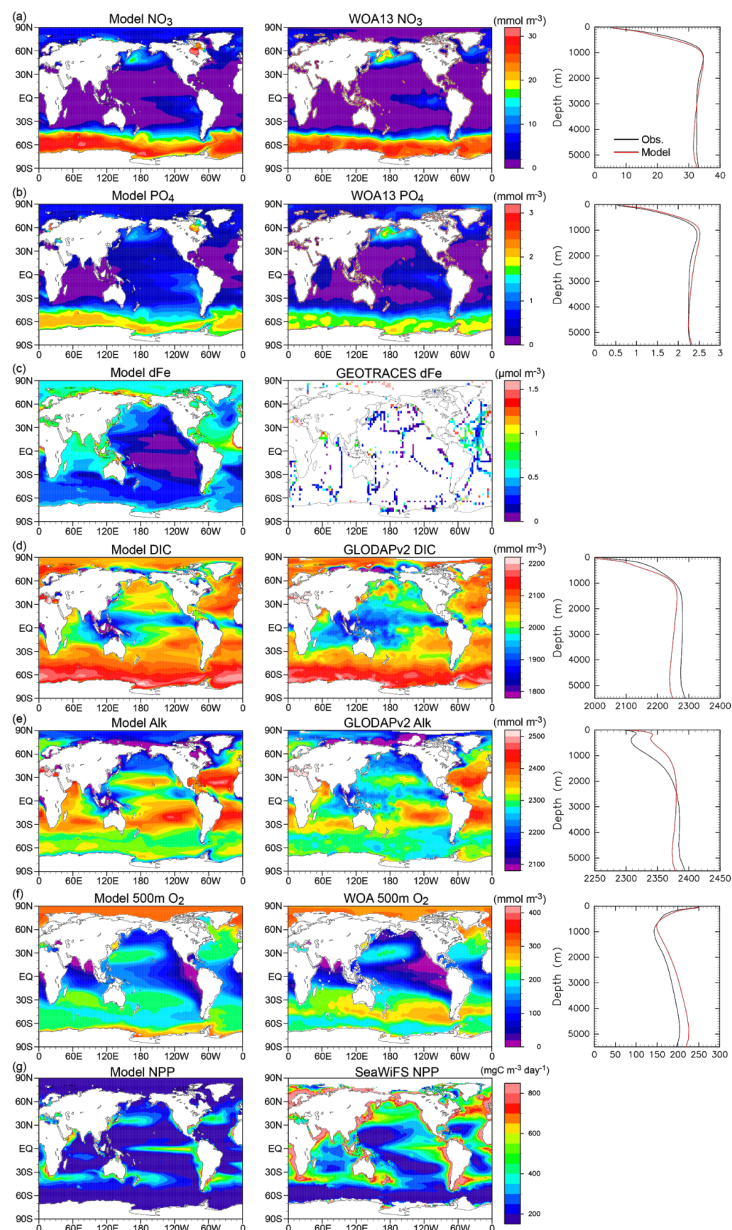


Figure 11

Comparison between model output and observations for key oceanic biogeochemical tracers. Simulated annual mean surface (a) nitrate, (b) phosphate, (c) DIC, (d) alkalinity, (e) dissolved oxygen at 500 m depth, and (f) surface NPP for the 2000s are compared with observations from the WOA2013 (Garcia et al., 2014a, 2014b) and GLODAPv2 datasets (Lauvset et al., 2016), as well as SeaWiFS (Behrenfeld and Falkowski, 1997) satellite observations. Left and central panels show horizontal distributions of model output and observations. Right panels show vertical distributions of model output (red lines) and observations (black lines).



860

3.2. Sensitivity analysis

3.2.1. Sensitivity of land biogeochemistry

To evaluate the sensitivities of modeled land biogeochemistry, we focus on GPP and its response to external forcing in the terrestrial system because this carbon flux is the primary driver of land carbon input. GPP change was calculated by taking the difference of the 2005–2014 averages between the HIST and CTL runs. Then, as diagnosed in Fig. 3c, the GPP change was decomposed into the response to (1) CO₂ increase, (2) climate change, and (3) LUC and agricultural change (Fig. 12) based on the simulation results of HIST, HIST-NOLUC, and HIST-BGC (Tables 1 and 2). Additionally, the GPP changes were further decomposed into the contributions from non-crop (i.e., contribution of primary/secondary vegetation, urban, and pasture) and crop tiles by weighting the GPP of each tile by their areal fractions on a grid.

In Fig. 12d–f, it can be seen that CO₂ increase in the historical period is the main driver of change in the land carbon cycle, and that the CO₂ fertilization effect prevails over most land areas except desert regions. In contrast, GPP response to climate change shows both positive and negative signs (Fig. 12g–i) with relatively smaller magnitudes. Mid- to high-latitude regions of the Northern Hemisphere shows positive change in GPP, likely due to lengthening of the vegetation growth season, enhanced plant growth following accelerated soil mineralization due to warming, and other mechanisms (e.g., soil water increase via precipitation and permafrost melting). In semiarid regions of the Southern Hemisphere (i.e., Africa, South Asia, Northern Australia, and the eastern side of South America), GPP shows slight reduction. As these regions have less precipitation in comparison with the tropics, the reduction in GPP is likely associated with precipitation change.

In addition to the responses to CO₂ increase and climate change, the model demonstrates spatial variation in the response of GPP to LUC (Fig. 12j). Historical LUC reduces the non-crop GPP contribution (Fig. 12k), while the crop contribution is enhanced (Fig. 12l). In particular, regions with intensive agriculture (Western Europe, East Asia, and Northwest America) show net positive change of GPP as grid averages (Fig. 12j), where increases in the crop contribution overcome reductions in the non-crop contribution (Fig. 12k and 12l). In the model, the crop contribution to GPP can be intensified by the following: 1) increasing the areal fraction of the crop tile following LUC forcing; 2) changing the vegetation type from natural vegetation to crop, whereby the latter has higher photosynthetic capacity than natural plant functional types (given as parameters that relate photosynthetic capacity with leaf nitrogen concentration, Appendix A); 3) applying nitrogen fertilizer to crop tiles; and 4) increasing nitrogen input via nitrogen-fixing crops, which is considered in the model as a subcategory of crop tiles. Indeed, the total area of cropland increases in the 20th century in the HIST simulation (Supplementary Fig. 2), which is reflected by the model producing an increase of nitrogen input via fertilizer application and biological fixation on the global scale (Fig. 4a).

By responding to CO₂ increase, climate change, and LUC, most land areas show increased GPP in the historical period (Fig. 12a), and regions with intensive agriculture show greater increase in GPP than induced solely by the CO₂ fertilization effect (Fig. 12a and 12d). This suggests modeled GPP is sensitive to land use and agricultural management forcing in addition to the increase of CO₂, and that this might be one of the reasons for the slowing of LUC-induced land carbon reduction in the latter half of the 20th century in the HIST simulation (green line in Fig. 3c).

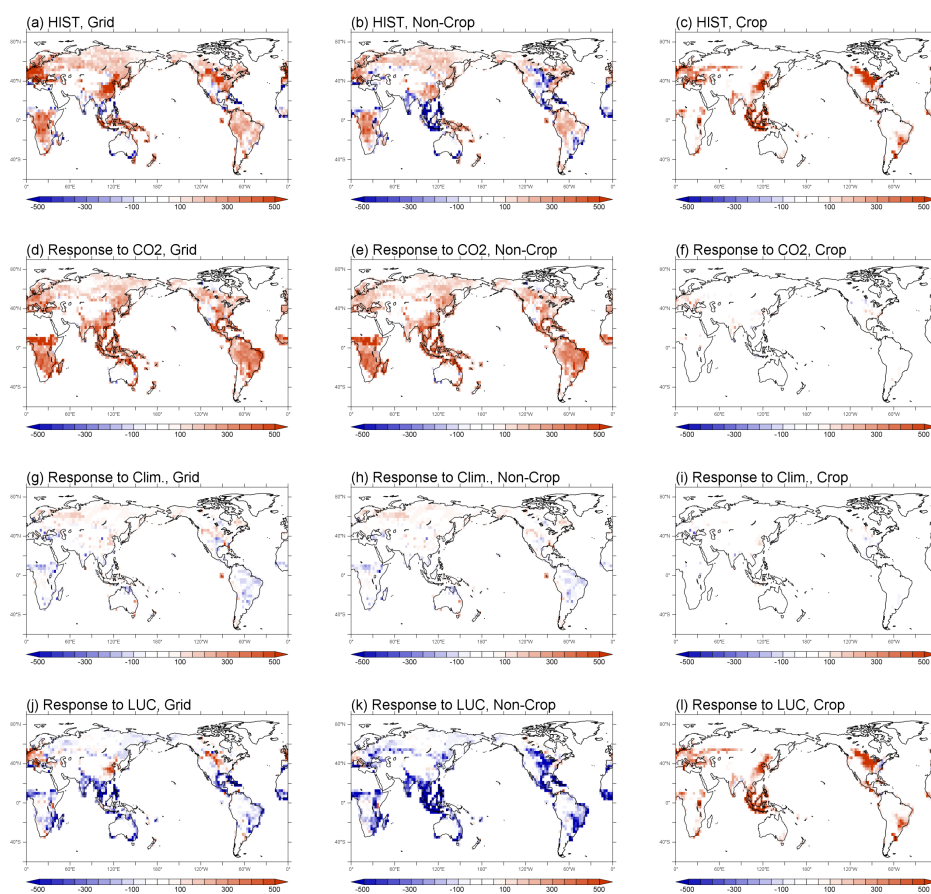


Figure 12

(Upper row) Changes in GPP ($\text{gC m}^{-2} \text{yr}^{-1}$) in HIST derived by taking the difference of the 2005–2014 averages of GPP
900 between HIST and CTL. (Second row) GPP response to CO_2 increase diagnosed from simulation results of HIST, HIST-
NOLUC, and HIST-BGC. (Third row) GPP response to climate change diagnosed by taking the difference between the
simulation results of HIST and HIST-BGC. (Lower row) GPP response to LUC obtained by taking the difference between
HIST and HIST-NOLUC. GPP changes in each left-hand panel are further decomposed into contributions from (middle
panels) non-crop tiles (primary vegetation, secondary vegetation, urban, and pasture) and (right-hand panels) crop tiles.

905

3.2.2. Sensitivity of ocean biogeochemistry

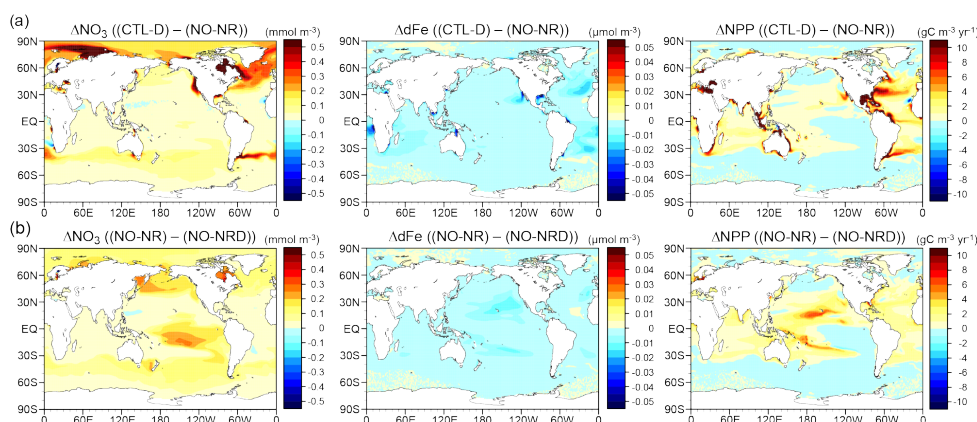
In this section, we investigate the sensitivity of oceanic NPP to external nutrient inputs from atmospheric deposition
and river discharge processes under preindustrial conditions because these processes are newly incorporated into the ESM.
Through combination of the simulation results of CTL-D, NO-NR, NO-NRD, and NO-FD (Tables 1 and 2), the impacts of
910 nutrient input on both nutrient concentration and primary productivity are analyzed (Fig. 13 for N input assessment and



Fig. 14 for Fe), and the spatial patterns of simulated nutrient limitation on NPP in the four experiments are examined (Fig. 15).

First, the impacts of riverine N input on the surface nutrient concentration and NPP are assessed by subtracting the zero-input scenario NO-NR from the control experiment CTL-D (Tables 1 and 2). Surface NPP is increased by riverine N input (by $>10 \text{ gC m}^{-3} \text{ yr}^{-1}$) in coastal areas such as the North Brazil Shelf and Gulf of Mexico (Fig. 13a). In comparison with the pattern of distribution of nutrient limitation (Fig. 15a and 15b), it is clear that NPP increase occurs in N-limited regions in the open ocean. Conversely, NPP decreases in Fe-limited regions because the NPP increase in N-limited regions consumes surface dissolved Fe. Surface NO_3 concentrations increase only slightly in N-limited regions because NO_3 is immediately consumed locally by phytoplankton. Remarkable increase in surface NO_3 concentrations is found in Fe-limited regions such as the Kara Sea, North Atlantic Ocean, Hudson Bay, and Subantarctic Ocean. Global NPP increases by 0.7 PgC yr^{-1} (by 2.5% in comparison with NO-NR). This value is comparable with the finding of da Cunha et al. (2007), who estimated a 5% increase in primary production due to riverine nutrient input. Note that nutrient retention in estuarine areas is not considered in our model. Thus, most nitrogen supplied from river mouths can easily be conveyed to the open ocean. Given that a recent modeling study estimated that approximately 75% of riverine nitrogen globally escapes from shelf areas to the open ocean (Sharples et al., 2016), our results on the impact of riverine N on NPP should be viewed as an upper limit for the estimation.

Second, the effects of atmospheric N deposition on surface nutrient concentration and NPP are evaluated by subtracting the zero-input scenario NO-NRD from the NO-NR experiment (Tables 1 and 2). Similar to riverine N input, atmospheric N deposition causes an increase of NPP in N-limited regions and a global increase in NO_3 (Figs. 13b, 15a, and 15c). According to deposition flux, significant changes in NPP are found in coastal areas and low-latitude regions of the Pacific Ocean. Global NPP increases by 0.3 PgC yr^{-1} (by 1% in comparison with NO-NR), which is consistent previous estimates (Duce et al., 2008; Moore et al., 2013).



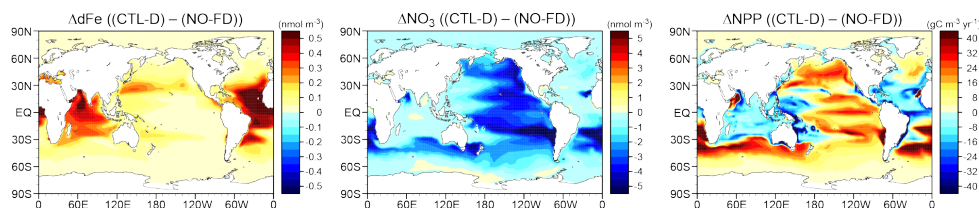
935

Figure 13

Changes in (left) surface nitrate, (center) dissolved iron, and (right) NPP driven by nitrogen input from (a) rivers (CTL-D – NO-NR) and (b) atmospheric deposition (NO-NR – NO-NRD).



940 Finally, changes in surface nutrient concentration and NPP, driven by atmospheric Fe deposition, are calculated by
subtracting the zero-input scenario NO-FD from the control experiment CTL-D (Tables 1 and 2). In contrast to N input,
atmospheric Fe deposition causes an increase of NPP in Fe-limited regions and a decrease in N-limited regions (Figs. 14,
15a, and 15d). Significant Fe increase is found in N-limited regions. Global NPP and export production increase by 1.8
and 0.8 PgC yr⁻¹, respectively (by 6.7% and 11%, respectively, in comparison with NO-FD). These percentage increases
945 are consistent with previous estimations by Moore et al. (2013). However, the sensitivity of export production to Fe
deposition from dust is higher than reported by Tagliabue et al. (2014), who estimated export production increases by
0.06–0.11 PgC yr⁻¹. Therefore, it seems difficult to obtain robust sensitivity both of iron and of the biological cycle to iron
input because of the high uncertainty regarding the iron cycle among models. Although nitrogen input from both
deposition and rivers has little effect on the spatial patterns of distribution of nutrient limitation (Fig. 15a–c), iron input
950 from the atmosphere changes the pattern in low-latitude regions from one of iron limitation to nitrogen limitation (Fig. 15a
and 15d).



955 **Figure 14**

Changes in (left) surface dissolved iron, (center) nitrate, and (right) NPP driven by dissolved iron input from dust
(CTL-D – NO-FD).

960

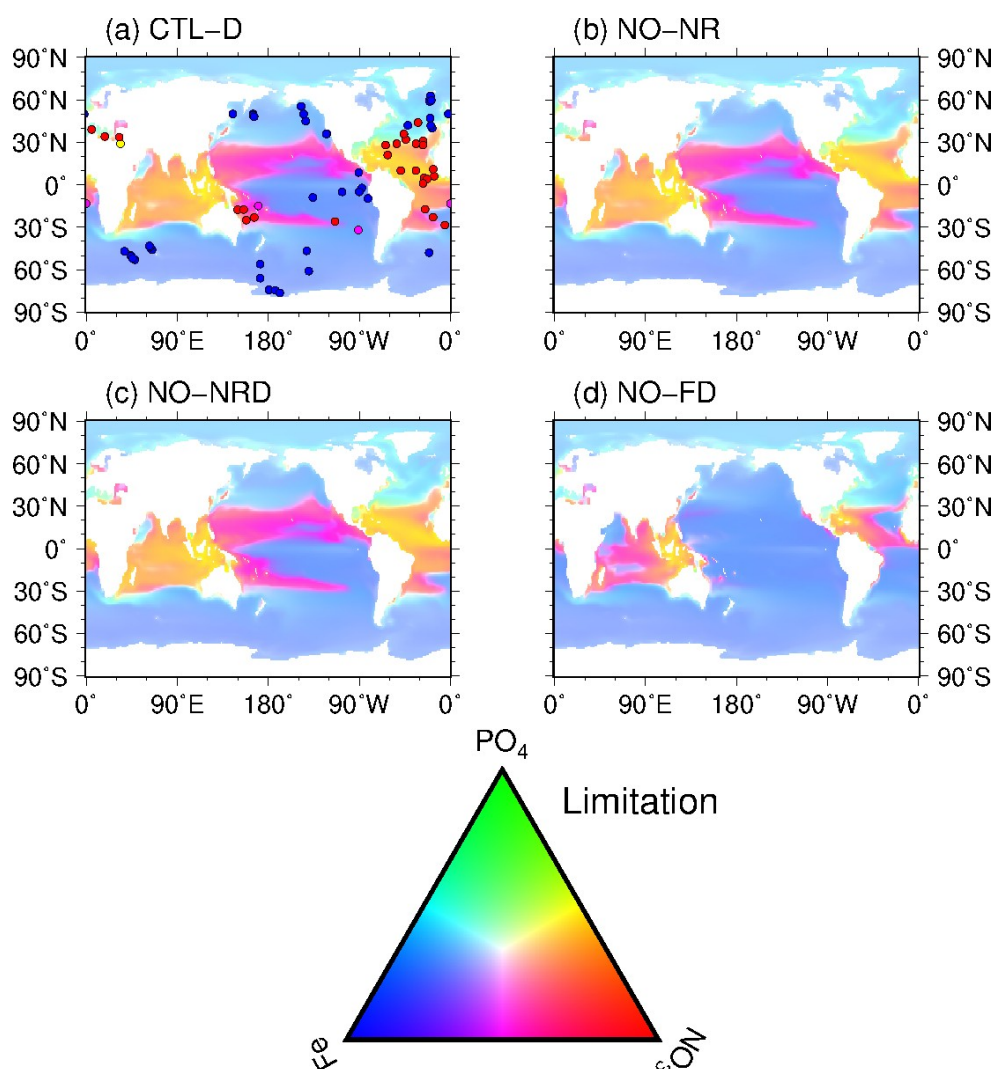


Figure 15

Limiting nutrient map for phytoplankton for (a) CTL-D, (b) NO-NR, (c) NO-NRD, and (d) NO-FD. Shading indicates limiting nutrient(s), e.g., red: N limitation, blue: Fe limitation, green: P limitation, magenta: N and Fe limitation, cyan: P and N limitation, and yellow: P and N limitation (see bottom color triangle). Circles in (a) represent observed limiting nutrients from nutrient addition experiments (Moore et al., 2013).
965

Here, we examine model sensitivity against global inputs of both N and Fe into the ocean through atmospheric deposition and river discharge in the preindustrial condition. We note, however, these two types of nutrient input have increased significantly since the preindustrial era because of human activities (Duce et al., 2008; Seitzinger et al., 2010; Krishnamurthy et al., 2010). In addition, ongoing nutrient input increase can lead to future increase in biological production, which might partly negate the production decrease driven by global warming. Conversely, the resultant
970



975 increase in export of OM would accelerate warming-induced ocean acidification and deoxygenation in subsurface waters,
leading to major environmental pressures. Thus, the combined effects of global warming and anthropogenic nutrient input
on ocean biogeochemical cycles should be explored in the future.

3.2.3. Sensitivity of riverine nitrogen

980 The coupling of land and ocean ecosystems via riverine nitrogen is one of the new features of MIROC-ES2L, and the
potential impact of the process on ocean biogeochemistry has already been examined and discussed in Sect. 3.2.2. Here,
we examine the response of river nitrogen loading itself against anthropogenic forcing by comparing the results of the
CTL, HIST-NOLUC, and HIST simulations.

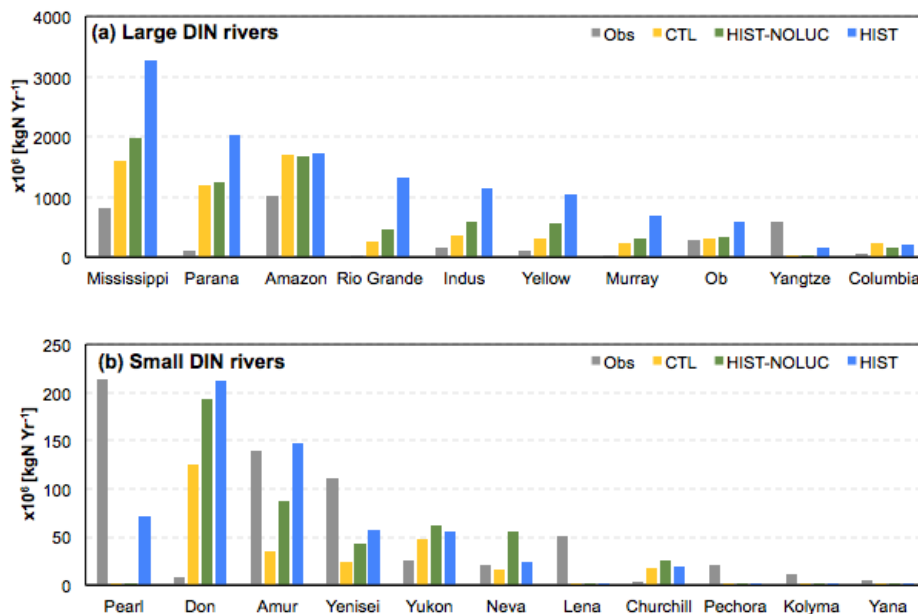
985 As already mentioned in Sect. 3.1.3, the global flux of riverine nitrogen input into the ocean is simulated at 17.5 TgN
yr⁻¹ in the CTL experiment (Table 4), and the flux is almost doubled in the 2000s at 33.9 TgN yr⁻¹ in the HIST run. This
number is larger than previous estimates of 19–25 TgN yr⁻¹ for the present-day condition (Smith et al., 2003; Mayorga et
al., 2010; Dumont et al., 2005). This overestimation might be caused by the inability of the model to simulate all forms of
nitrogen in rivers. For example, the model simulates only dissolved inorganic nitrogen (DIN) flux; thus, the expected
nitrogen flux with non-DIN forms (e.g., dissolved organic and particulate matter) might be partly imposed on the DIN flux
in the simulations. Indeed, global total nitrogen flux, including DIN, dissolved organic nitrogen, and particulate nitrogen is
estimated at 37–66 TgN yr⁻¹ (Beusen et al., 2016; Mayorga et al., 2010; Boyer et al., 2006; Seitzinger et al., 2005), which
990 is closer to the result of MIROC-ES2L.

Another possible reason for the above overestimation is precipitation bias and resultant overestimation of BNF on land.
As mentioned in Sect. 3.1.4, the model has positive precipitation bias on land, particularly in arid/desert regions (Fig. 6).
As the scheme for natural BNF flux employed in MIROC-ES2L is modeled to be controlled by the actual
evapotranspiration rate (Cleveland et al., 1999), the precipitation bias in arid regions could easily lead to overestimation of
995 the BNF flux and produce a resultant increase of riverine nitrogen loading. This is also evident when decomposing the
global riverine flux into river basins and comparing the findings with a previous study by Dumont et al. (2005) (Fig. 16).
MIROC-ES2L overestimates the DIN fluxes of large rivers such as the Amazon, Mississippi, and Yangtze rivers, even in
the CTL experiment where all anthropogenic forcings are fixed at preindustrial levels. This suggests the necessity of
improvement of the baseline flux of riverine nitrogen in the model. For more in-depth discussion, it will be necessary to
1000 simulate explicitly the organic and particulate nitrogen fluxes in rivers, and it might be necessary to simulate the explicit
sedimentary and chemical-reaction processes in freshwater and coastal zone systems.

Although bias exists in the magnitude of riverine nitrogen flux both globally and locally, we confirm the model capable
of capturing qualitatively the changes in riverine nitrogen flux during the historical period. In Fig. 16, the difference
between the results of CTL and HIST-NOLUC mainly reflect the change induced by nitrogen deposition (and historical
1005 climate change) (Table 2), and the model demonstrates that deposition has increased N fluxes in many rivers. In addition,
the difference between HIST-NOLUC and HIST demonstrates the impact of LUC and agricultural management change
(Table 2), and regions that have intensive agriculture within their watersheds (e.g., the basins of the Mississippi, Indus,
Yellow, and Yangtze rivers) are simulated as strongly affected by the forcing change. This simulated trend in the historical
period is qualitatively consistent with previous studies (Gruber and Galloway, 2008). Furthermore, the model simulates
1010 the global riverine flux to be increased by 16.4 TgN yr⁻¹ in the historical period. This value is quantitatively consistent



with previous estimates, e.g., 16 TgN yr⁻¹ by Dumont et al. (2005) for DIN flux, and 18 and 19 TgN yr⁻¹ by Beusen et al. (2016) and by Green et al. (2004), respectively, for total N flux.



1015

Figure 16

Simulated and observed DIN load per river basin: sorted by simulated (a) first 10 largest rivers and (b) second 10 largest rivers. Vertical gray bars represent observations (Dumont et al., 2005). Blue, green, and yellow bars correspond to the results of the HIST, HIST-NOLUC, and CTL experiments, respectively.

1020

3.2.4. TCR, AF, and TCRE

We have evaluated the performance of MIROC-ES2L in terms of climate and biogeochemistry using the HIST simulation results (chapter 3.1), and we have explored how the model responds to forcing by comparing the results of different simulations (chapter 3.2). Here, the model sensitivity of the global climate–carbon cycle against CO₂ increase is analyzed by calculating TCR, AF, and TCRE from the results of the 1PPY, 1PPY-BGC, and 1PPY-RAD experiments (see Sect. 2.2.2 for the method). These quantities summarize the total performance of the climate, carbon cycle, and climate–carbon cycle system in the models, which enables us to compare them with existing ESMs.

The TCR, AF, and TCRE derived from the 1PPY simulation are displayed in Table 5 and Fig. 17. The TCR of MIROC-ES2L is 1.5 K, which is lower than the multimodel mean of the CMIP5 ESMs but within the range of spread (1.8 ± 0.5 K; Gillet et al., 2013). Compared with our previous ESM (i.e., MIROC-ESM; Watanabe et al., 2011), the TCR has reduced by 32% because of the replacement of the physical core of the ESM from the MIROC3-based model to that of MIROC5 (Watanabe et al., 2010). The value of AF, which is a quantity that characterizes the carbon cycle response in an ESM but is dependent on TCR, was simulated at 0.61 in MIROC-ESM. This value is reduced to 0.52 in MIROC-ES2L, i.e., the new

1030



1035 model has a stronger carbon sink than the previous version. The value of AF in the new model is of similar magnitude to
the CMIP5 model average (0.53 ± 0.06 ; Gillett et al., 2013). The lowered TCR and the moderate AF cause the new model
to have moderate TCRC (1.3 K EgC^{-1}), which is smaller than that of the CMIP5 model average ($1.6 \pm 0.5 \text{ K EgC}^{-1}$) by
19%. Using TCRC, we can approximate the value of CE until the global temperature exceeds a specific mitigation target;
CE for the 2°C warming target should be approximately 1540 PgC for MIROC-ES2L, 910 PgC for MIROC-ESM, and
950–1820 PgC for the CMIP5 models.

1040

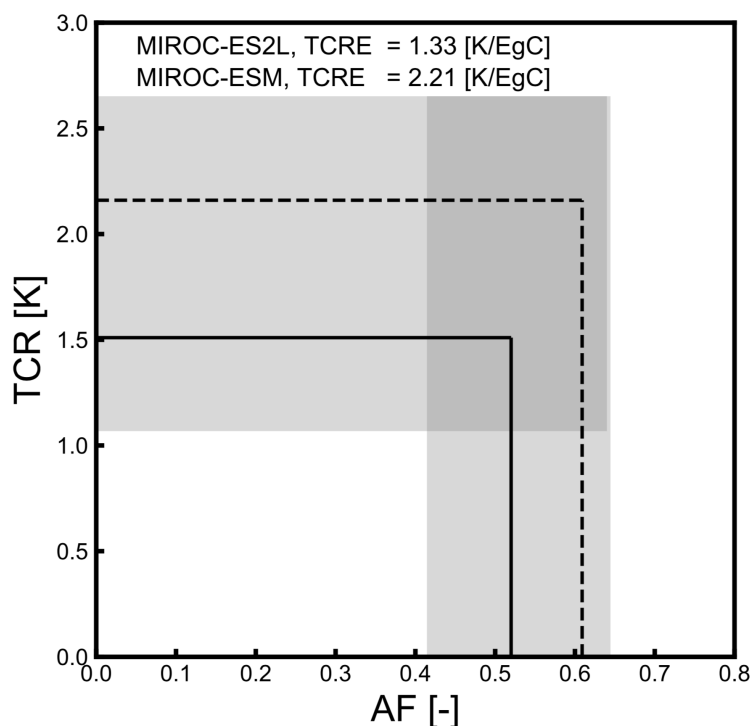


Figure 17

1045 Transient climate response (TCR), cumulative airborne fraction (AF), and transient climate response to cumulative
carbon emission (TCRC) for MIROC-ES2L (solid black lines), MIROC-ESM (dashed black lines; Watanabe et al., 2011;
Gillett et al., 2013), and CMIP5-ESMs (gray shading; Gillett et al., 2013) at the doubled CO_2 level in the 1PPY
experiment. Vertical and horizontal widths of the shaded areas represent CMIP5 multimodel mean $\pm 1.65\sigma$. TCRC is
equivalent to $(\text{TCR} \times \text{AF})/\text{CA}$, where CA is the carbon increase in the atmosphere (which is a constant of approximately
600 PgC in concentration-driven simulations).

1050



Table 5

1055 Comparison of TCR, AF, and TCRE between MIROC-ES2L, MIROC-ESM, MIROC5.2, and CMIP5 ESMs in the 1PPY simulation. For MIROC-ES2L, both TCR and AF are calculated based on 20-year means of T2, CL, and CO centered on the 70th year of the 1PPY simulation (i.e., the time when the CO₂ concentration is doubled from the preindustrial condition), and TCRE is calculated based on TCR and AF. Numbers for the CMIP5-ESMs were obtained from Gillett et al. (2013) and are presented as the multimodel mean $\pm 1\sigma$.

	TCR (K)	AF (-)	TCRE (K EgC ⁻¹)
MIROC-ES2L (This study)	1.5	0.52	1.3
MIROC-ESM (Watanabe et al., 2011; Gillett et al., 2013)	2.2	0.61	2.2
MIROC5.2 (Tatebe et al., 2018)	1.6	–	–
CMIP5 (Gillett et al., 2013)	1.8 \pm 0.5	0.53 \pm 0.06	1.6 \pm 0.5

1060

To further explore the reason why AF is lowered in MIROC-ES2L, the strengths of the carbon cycle feedbacks were analyzed using the 1PPY-BGC and 1PPY-RAD simulation results (Table 6), and the findings were compared with the CMIP5 ESMs (Arora et al., 2013). The strength of CO₂–carbon feedback (β) of land is simulated at 0.52 PgC PgC⁻¹, which is slightly higher than the CMIP5 model average (0.43 \pm 0.21 PgC PgC⁻¹) and larger than that of MIROC-ESM by 48%. The strength of oceanic CO₂–carbon feedback in the CMIP5 ESMs displays less spread among the models (0.38 \pm 0.03 PgC PgC⁻¹) and the result of MIROC-ES2L is within the spread (0.35 PgC PgC⁻¹). The absolute magnitude of the climate–carbon feedback (γ) for land and ocean in MIROC-ES2L is –71 and –4.5 PgC K⁻¹, respectively, both of which are less negative than the result of MIROC-ESM by 20% for land and 63% for ocean. Consequently, the land γ in MIROC-ES2L is within the range of the CMIP5 ESMs (–58 \pm 29 PgC K⁻¹), while the ocean γ is slightly larger than the upper range of the CMIP5 ESMs (–7.8 \pm 2.9 PgC K⁻¹).

1065
1070

As the quantities β and γ have different units, it is difficult to conclude which feedback process contributes most to the AF change. To compare them with the same unit, we used the quantity “ u ” proposed by Gregory et al. (2009). This quantity, which is defined as $u_{\beta} = \beta$ and $u_{\gamma} = \gamma \times T/CA$, has the unit PgC PgC⁻¹, and it can relate the carbon cycle feedback parameters to AF, as $AF = 1/(1 + u_{\beta L} + u_{\beta O} + u_{\gamma L} + u_{\gamma O})$ (see Appendix E for the derivation). When comparing the u quantities of MIROC-ES2L with the CMIP5 models (Fig. 18), it is evident that the ocean component of MIROC-ES2L is less sensitive than the previous model for both CO₂–carbon and climate–carbon feedbacks. These two changes almost counteract each other; thus, the ocean component does not explain the reduced AF in the new model (Table 5, Fig. 17). For land, the climate–carbon feedback (u_{γ}) in MIROC-ES2L is intermediate, while MIROC-ESM was one of the most

1075

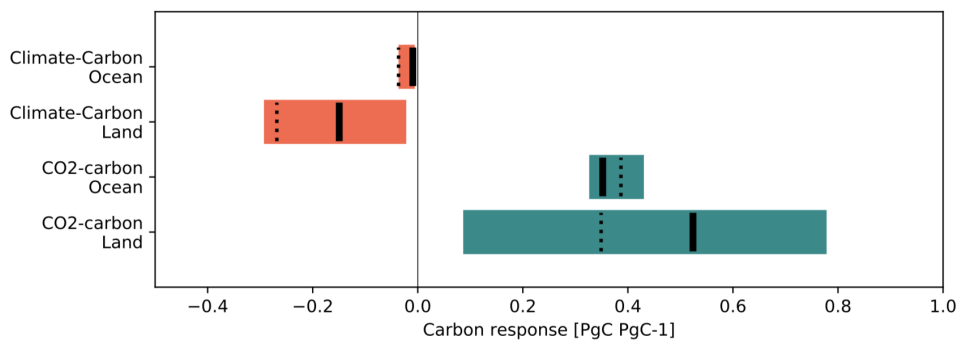


1080 sensitive models of the CMIP5 ESMs. In addition, the magnitude of the land CO₂–carbon feedback (u_{β}) is increased from
 MIROC-ESM to MIROC-ES2L by 48% ($u_{\beta} = \beta$). Therefore, the land component is the main cause of AF change, making
 the magnitude of both the CO₂–carbon and the climate–carbon feedbacks increasingly positive, i.e., strengthening the land
 carbon sink.

1085 **Table 6**

Comparison of CO₂–carbon and climate–carbon feedback parameters between MIROC-ES2L, MIROC-ESM, and the
 CMIP5 ESMs. As presented in Arora et al. (2013), TCR, AF, and TCRC are calculated at the time when CO₂
 concentration is quadrupled from the preindustrial condition (i.e., the 140th year in the 1PPY simulation) by taking the
 anomaly from the CTL run. Numbers of CMIP5 ESMs were obtained from Arora et al. (2013) and are presented as the
 1090 multimodel mean $\pm 1\sigma$.

	β land (PgC PgC ⁻¹)	β ocean (PgC PgC ⁻¹)	γ land (PgC K ⁻¹)	γ ocean (PgC K ⁻¹)
MIROC-ES2L (This study)	0.52	0.35	-71	-4.5
MIROC-ESM (Watanabe et al., 2011; Arora et al., 2013)	0.35	0.39	-89	-12
CMIP5 (Arora et al., 2013)	0.43 ± 0.21	0.38 ± 0.03	-58 ± 29	-7.8 ± 2.9



1095 **Figure 18**

Comparison of strength of CO₂–carbon and climate–carbon feedbacks between MIROC-ES2L and the CMIP5 models
 evaluated using the 1PPY, 1PPY-BGC, and 1PPY-RAD experiments. Vertical solid and dotted black bars represent
 MIROC-ES2L and MIROC-ESM, respectively, and the horizontal bars represent the range of the CMIP5 ESMs (mean \pm
 1.65 σ). To compare the two types of feedback strength with the same unit, land and ocean carbon storage change were
 1100 both normalized by dividing the atmospheric carbon change, which corresponds to the “u” quantity proposed by Gregory



et al. (2009): $CE = CA (1 + u_{\beta} + u_{\gamma})$, where $u_{\beta} = \beta$, $u_{\gamma} = \gamma \times \alpha$. If $u > 0$ ($u < 0$), the feedback sign is negative (positive). The calculations were based on the anomaly from the CTL run at the time of quadrupled CO_2 concentration from the preindustrial condition (i.e., the 140th year of the 1PPY, 1PPY-BGC, and 1PPY-RAD simulations).

1105

4. Summary and conclusions

In this study, a new Earth system model (MIROC-ES2L) was developed using a state-of-the-art climate model (MIROC5.2) as the physical core. This new ESM embeds a terrestrial biogeochemical component with explicit carbon–nitrogen interaction (VISIT-e) that accounts for the nutrient limitation of nitrogen on plant growth and the resultant change in the land carbon sink. In addition, the ocean biogeochemical component (OECO2) is largely updated to simulate the biogeochemical cycles of carbon, nitrogen, phosphorus, iron, and oxygen such that oceanic primary productivity in the model is now controlled by multiple nutrient limitations. As a new challenge, land and ocean nitrogen cycles were coupled via river discharge processes; thus, marine ecosystem productivity can now be controlled by riverine nitrogen input. Furthermore, iron-related processes such as emission, atmospheric transport, deposition, and utilization in the marine ecosystem are newly included to represent the micronutrient limitation on phytoplankton productivity. This is necessary for reproducing the HNLC regions and for simulating ecosystem variability in response to external iron inputs.

To evaluate the performance of the new model, a historical simulation following CMIP6 protocols and forcing datasets was performed for the 1850–2014 period, and the results were compared with observation-based products. We confirmed the model reasonably reproduces the global changes in net TOA radiation balance, SAT, SST and upper-ocean temperature. Considering the few biophysical feedbacks on climate in the model, the good performance in simulating the physical fields is inherited from the original climate model (MIROC5.2), although persistent problems remain such as the warm bias in the Southern Ocean, as found in other climate models. Global carbon and nitrogen budgets in the historical simulation were also examined and discussed by comparing the results with existing studies. It was confirmed that the model could successfully capture the historical trends of global biogeochemical budgets. The spatial distributions of fundamental variables of the land carbon cycle were also assessed by comparison with observation-based products, and the model showed reasonable patterns for primary productivity, forest carbon, and SOC. The spatial patterns of oceanic macro- and micronutrients, total inorganic carbon, alkalinity, oxygen, and primary productivity were all confirmed captured well in the historical simulation.

To assess the global climate–carbon cycle feedback in MIROC-ES2L, a sensitivity analysis was performed in which atmospheric CO_2 concentration was prescribed to increase by $1\% \text{ yr}^{-1}$. Then, the values of TCR, AF, and TCRE were calculated and compared with the CMIP5 ESMs. TCR in the new model is reduced to 1.5 K, which is approximately 70% of the previous model used for CMIP5, through the replacement of the physical core from the MIROC3-based model to that of MIROC5.2. AF is also reduced by 15%. Further feedback analysis of the carbon cycle revealed that most of the AF reduction should be attributable to the intensified land carbon sink in the new model, resulting in a level of AF that is close to the average of the CMIP5 ESMs. TCRE, which is a quantity that aggregates the response of the entire climate–carbon cycle against anthropogenic CO_2 emissions, is 1.3 K EgC^{-1} in MIROC-ES2L. This is reduced from value in the model



1140 used for CMIP5 by 32% and it is slightly smaller than the multimodel mean of the CMIP5 ESMs. Thus, MIROC-ES2L
might be an “optimistic” model in terms of simulating global climate and carbon cycle change, considering that some
CMIP6-class models are likely to have higher climate sensitivity (Voosen et al., 2019). To discuss whether the climate and
carbon cycle sensitivities in the model are realistic, it will be necessary to perform multimodel comparisons on feedback
strengths using CMIP6 ESMs and to establish constraints on each feedback process based on observation (e.g., Wenzel et
al., 2016).

1145 In the new model, the terrestrial nitrogen cycle processes and the interaction with the carbon cycle are modeled
explicitly. By performing several types of simulation, it was demonstrated clearly that agricultural management such as
fertilizer application has changed the carbon cycle (GPP) in the historical period, suggesting that the nitrogen cycle in the
model actually acts on the land carbon cycle. The model simulated change in the total land carbon during 1850–2014 at 44
PgC, which is within the estimated range of Le Quéré et al. (2018). However, historical terrestrial carbon change is highly
1150 uncertain because the change is processed by multiple responses against the external forcing of CO₂, LUC, and climate
change, each of which has its own estimation uncertainty. Thus, as performed in this study, decomposition of the impact
of these forcings in historical simulations and in multimodel comparisons would be helpful in specifying the processes that
produce the large simulation spread of the land carbon budget among the ESMs. Furthermore, although we confirmed the
nitrogen cycle actually acts on the carbon cycle in the model, this study did not quantify by how much the soil nutrient
1155 deficit could down-regulate plant growth and reduce the natural carbon sink. For this, a sensitivity analysis associated with
the carbon–nitrogen interaction is planned in CMIP6 (Jones et al., 2016), and the multimodel comparison study will reveal
the strength of the carbon–nitrogen feedback in MIROC-ES2L relative to other CMIP6-class ESMs.

In the new model, the ocean nitrogen cycle is modified to be an open system and thus the model can reflect the
influences of external sources of nitrogen inputs via atmospheric deposition and river discharge. Our sensitivity analyses
1160 under preindustrial condition suggested minor contributions of these two external sources to global primary productivity.
However, regions in which primary productivity is constrained by nitrogen availability showed a strong positive NPP
response to the relaxation of nitrogen limitation. It accelerates the use of other nutrients within the marine ecosystem in
such regions and it reduces iron and phosphorus availability in other regions. Furthermore, by switching on the process of
iron deposition into the ocean, the model showed an increase of approximately 7% in GPP under the preindustrial
1165 condition, suggesting that iron input has a relatively stronger impact than nitrogen. Coupling of iron cycle processes in the
model led to successful reproduction of HNLC regions, and it will enable the model to project future biogeochemical
changes induced by anthropogenic iron emissions associated with the use of fossil fuels and biomass burning. We note,
however, as an atmospheric chemistry module is not included in MIROC-ES2L, the atmospheric chemical reaction of
iron-containing aerosols is ignored and the iron solubility to seawater is simply assumed constant. Considering the
1170 relatively strong impact of iron deposition on marine primary productivity in the model, we need further detailed
evaluation and modification of the iron cycle processes in terms of both aerosol transport and marine biogeochemical
responses.

In addition to such improvements in terms of the iron cycle, other factors should be improved/extended in the ESM for
future simulation study. First, a freshwater biogeochemistry module is required. In the present model, the chemical form
1175 of riverine nitrogen is assumed inorganic, but actual river flow contains OM and particulate matter that undergo
biogeochemical processing during transport. Thus, inclusion of the transport of organic/inorganic matter and the modeling
of freshwater biogeochemistry might be necessary. The sensitivity analysis that showed relatively strong impact of
riverine nitrogen on regional marine ecosystem productivity supports this conclusion. Second, MIROC-ES2L can simulate



1180 natural emissions of nitrous oxide; however, the emissions did not change the radiative balance of the atmosphere in this
study. Nitrous oxide is one of the strongest greenhouse gases and it has a long lifetime. However, as diagnosed in this
study, future nitrous oxide emissions could be controlled by land use and agriculture, as well as climate change. Therefore,
full coupling of the nitrous oxide cycle with other associated atmospheric chemical processes should be incorporated in
the next-generation ESM, together with the methane cycle, as suggested in previous studies (e.g., Collins et al., 2018).
1185 Third, a mechanistic model for the denitrification process in ocean sediment should be included in a future model. The
present model simulates only the denitrification rate of water column, and the flux from sediment is likely imposed on the
water-column denitrification. As the timescale of the sedimentary process is likely longer than that of water-column
denitrification, explicit modeling of sedimentary denitrification will be important, particularly for long-term simulations
over timescales of millennia. Finally, we partly demonstrated the importance of external sources of nutrients for marine
productivity, although its evaluation was performed under the preindustrial condition. As anthropogenic nutrient inputs
1190 under that condition are much smaller than under the present-day condition and they could be amplified or mitigated in the
future, a similar simulation study should be undertaken for present-day and future conditions.

ESMs represent powerful tools with which to investigate interactions between climate, biogeochemistry, and human
activities, and they have facilitated climate projections and explorations of future emissions of greenhouse gases for
achieving climate change mitigation goals. Such models are also valuable for examining how Earth system components
1195 might respond to different levels of mitigation policies/scenarios spanning from the business-as-usual scenario to one
employing intensive measures such as geoengineering techniques. Furthermore, state-of-the-art ESMs can now partly
simulate environmental problems on Earth that are becoming evident/doubted in association with climate change, e.g.,
acidification and hypoxia in the ocean, global nitrogen loading, air pollution, and habitable zone changes in ecosystems.
ESMs can simulate such problems and their interactions in a holistic and consistent manner. Such simulations have
1200 potential to elucidate sustainable ways to mitigate climate change with less environmental stress. To support such
applications, further efforts should be made to evolve ESMs and to constrain model performance in collaboration with
observation studies.

5. Appendices

1205 Appendix A. Land ecosystem/biogeochemical component

A.1 Nitrogen cycle

The structure of carbon and nitrogen compartments and the flux calculations in VISIT-e mostly follow the original
version of the model (Ito and Inatomi, 2012a). For N cycle and LUC processes, some major changes were brought to
VISIT-e to couple the model with MIROC-ES2L; the details are described below.

1210

A.1.1. N compartment structure in VISIT-e

Terrestrial N dynamics in VISIT are simulated based on three major compartment groups of N storage: vegetation N
(N_{VEG}), soil organic matter (N_{SOM}), and soil inorganic matter (N_{IOM}). The component N_{VEG} is composed of canopy N
(N_{CAN}) and storage N (N_{STG}):

$$1215 \quad N_{\text{VEG}} = N_{\text{CAN}} + N_{\text{STG}}.$$



The mass conservation equations for N_{CAN} and N_{STG} are as follows:

$$dN_{CAN}/dt = FN_{SBNF, CAN} + FN_{UPTK, CAN} + FN_{RALC} - FN_{MORT, CAN}, \quad (A1)$$

$$dN_{STG}/dt = FN_{SBNF, STG} + FN_{UPTK, STG} + FN_{WTHD} - FN_{MORT, STG}, \quad (A2)$$

where FN represents nitrogen flux, and the subscripts SBNF, UPTK, RALC, WTHD, and MORT represent symbiotic biological N fixation, N uptake by plants, reallocation of storage N to the canopy, withdrawal of canopy N to storage, and loss of N by mortality, respectively. In this study, biological N input into vegetation (represented by FN_{SBNF}) is modified from the original model; the detail is described in Sect. A.1.2.

The component N_{SOM} is composed of the three nitrogen pools of litter (N_{LIT}), humus (N_{HUM}), and microbes (N_{MCR}):

$$N_{SOM} = N_{LIT} + N_{HUM} + N_{MCR}. \quad (A3)$$

The N conservation equations for the pools are as follows:

$$dN_{LIT}/dt = FN_{MORT, CAN} + FN_{MORT, STG} + FN_{NBNF} - FN_{HUMF} - FN_{MNRL, LIT}, \quad (A4)$$

$$dN_{HUM}/dt = FN_{HUMF} + FN_{MORT, MCR} - FN_{MNRL, HUM}, \quad (A5)$$

$$dN_{MCR}/dt = FN_{IMBL} - FN_{MORT, MCR}, \quad (A6)$$

where subscripts NBNF, HUMF, MNRL, and IMBL represent nonsymbiotic BNF, humification of litter, mineralization of litter/humus, and immobilization by microbes, respectively. The components FN_{NBNF} and FN_{HUMF} are new components of flux, which are described in Sect. A.1.2 and Sect. A.1.3, respectively.

The inorganic nitrogen is assumed to consist of N pools of NH_4^+ (N_{NH4}) and NO_3^- (N_{NO3}):

$$N_{IOM} = N_{NH4} + N_{NO3}. \quad (A7)$$

The budget equation for N_{NH4} is as follows:

$$dN_{NH4}/dt = FN_{DEPO, NH4} + FN_{FRTL, NH4} + FN_{MNRL, LIT} + FN_{MNRL, HUM} - FN_{UPTK, NH4} - FN_{IMBL} - FN_{N2ON} - FN_{NTRF} - FN_{NH3V} - FN_{ALOS, NH4}, \quad (A8)$$

where subscripts DEPO, FRTL, N2ON, NTRF, NH3V, and ALOS represent deposition, fertilizer, N_2O emission of nitrification process, nitrification of NH_4^+ , NH_3 volatilization, and abiotic N loss, respectively.

The budget equation for N_{NO3} is as follows:

$$dN_{NO3}/dt = FN_{DEPO, NO3} + FN_{FRTL, NO3} + FN_{NTRF} - FN_{UPTK, NO3} - FN_{N2OD} - FN_{N2} - FN_{LECH} - FN_{ALOS, NO3}, \quad (A9)$$

where subscripts N2OD and N2 represent N_2O and N_2 emissions in the denitrification process, respectively and LECH presents N leaching.

In the above two equations, FN_{DEPO} and FN_{FRTL} are forced by external datasets, while FN_{ALOS} is the process newly introduced in this study, which is described in Sect. A.1.4.

A.1.2. Biological N fixation



BNF is calculated based on the actual evapotranspiration rate (Cleveland et al., 1999). In the original version of VISIT, all nitrogen fixed through BNF (FN_{BNF}) was assumed available for plants. As this assumption makes vegetation in the model less dependent on soil nutrient availability, the model is modified in that only a portion of BNF-N is made directly available for plant. For this, FN_{BNF} is decomposed into symbiotic BNF (FN_{SBNF}) and nonsymbiotic BNF (FN_{NBNF}):

$$FN_{BNF} = FN_{SBNF} + FN_{NBNF} \quad (A10)$$

and

$$FN_{SBNF} = \alpha_{SBNF} \times FN_{BNF}, \quad (A11)$$

$$FN_{NBNF} = (1 - \alpha_{SBNF}) \times FN_{BNF}, \quad (A12)$$

where α_{SBNF} is the portion of N of symbiotic BNF. Here, α_{SBNF} is assumed as 0.5 as the landscape-level parameter. Nitrogen fixed by the symbiotic process is used directly by plants, while N fixed by nonsymbiotic microbes is assumed to directly form part of the litter. The BNF in cropland is modeled differently, as shown in Sect. A.2.3.

1260 A.1.3. Mineralization, humification, and immobilization

The mineralization rate of litter is same as that in the original version, and it is calculated as follows:

$$FN_{MNRL, LIT} = N_{LIT} \times (FC_{MNRL, LIT}/C_{LIT}), \quad (A13)$$

where $FC_{MNRL, LIT}$ is the C mineralization rate of litter and C_{LIT} is the amount of C in the litter pool.

The humus N mineralization rate is similar to that of litter but it is modified to be dependent on the humus CN ratio (CN_{HUM}):

$$FN_{MNRL, HUM} = N_{HUM} \times (FC_{MNRL, HUM}/C_{HUM}) \times (1 - f_{CN}(CN_{HUM})) \quad (A14)$$

and

$$f_{CN}(CN_{HUM}) = S_{min} \times \exp((\log S_{max} - \log S_{min}) / (R_{max} - R_{min}) \times (CN_{HUM} - R_{min})). \quad (A15)$$

Here, S_{max} and S_{min} are the maximum and minimum fractions of mineralized N that eventually move to the inorganic N pool (N_{NH4}), respectively. R_{max} and R_{min} are the maximum and minimum CN ratios in the humus pool, respectively. The term $1 - f_{CN}(CN_{HUM})$ controls the humus CN ratio to be between R_{max} and R_{min} , by accelerating humus N mineralization under a lower CN ratio and decreasing it under a higher CN ratio. Here, the values of $S_{max} = 0.95$ and $S_{min} = 0.05$ are assumed, and R_{max} and R_{min} are set to the values of 40 and 10, respectively.

Immobilization rate is simplified in VISIT-e and it is modeled as a function of the mineralization rate of litter N, depending on the CN status in the humus:

$$FN_{IMBL} = FN_{MNRL, LIT} \times f_{CN}(CN_{HUM}). \quad (A16)$$

Thus, N immobilization is accelerated if the humus has a high CN ratio and it decreases under a lower CN condition.

N flux by humification (N flow from litter to humus, $FN_{HUMF, LIT}$) is newly introduced in VISIT-e and it is modeled as follows:

$$FN_{HUMF, LIT} = N_{LIT} \times (FC_{HUMF, LIT}/C_{LIT}), \quad (A17)$$

where $FC_{HUMF, LIT}$ is the rate of C flux in the humification process, which is simulated in the C cycle part of the model.



A.1.4. Abiotic N loss

Abiotic N loss from soil ($FN_{ALOSS, NH4}$ and $FN_{ALOSS, NO3}$) is newly introduced in VISIT-e to prevent infinite N accumulation in deserts and arid regions, where much N removal thorough biotic and hydrological processes cannot be expected. This new scheme is based on the findings of McCalley and Sparks (2009) and it is modeled as follows:

$$FN_{ALOSS, NH4} = S_{ALOSS} \times \exp(K_{ALOSS}(T_{sfc} - 50)) \times N_{NH4}, \quad (A18)$$

$$FN_{ALOSS, NO3} = S_{ALOSS} \times \exp(K_{ALOSS}(T_{sfc} - 50)) \times N_{NO3}, \quad (A19)$$

where S_{ALOSS} is a specific rate of abiotic loss that is set to the value of 7.26×10^{-3} ($\text{ngN m}^{-2} \text{s}^{-1}$) (Schaeffer et al., (2003)), and K_{ALOSS} is a constant to normalize the rate at 50°C . Here, the emitted gas is assumed an inert form of N.

A.1.5. N limitation on plant productivity

To simulate soil nutrient (soil inorganic nitrogen) control on plant growth, VISIT-e is modified from the original model as follows.

First, the photosynthetic capacity (P_{CSAT}), which used to be given as the fixed parameter, is modified such that it is controlled by N concentration in the leaf (N_{FOL}):

$$P_{CSAT} = K_{PSAT1} \times N_{FOL} + K_{PSAT2} \quad (A20)$$

and

$$N_{FOL} = N_{CAN}/LAI, \quad (A21)$$

where K_{PSAT1} and K_{PSAT2} are the slope and intercept, respectively, of the empirical relationship between N_{FOL} and P_{CSAT} , and LAI is the leaf area index. In this study, the parameters K_{PSAT1} and K_{PSAT2} were obtained from a meta-analysis study of Kattge et al., (2009). The leaf-level photosynthetic capacity is upscaled using the analytical method of the Monsi–Saeki theory, assuming a vertically uniform distribution of canopy N.

Second, actual N uptake by plants (FN_{UPTK}) is determined by the balance between N demand by plants (FN_{DMND}) and the potential supply from the soil (FN_{SPPL}), which allows the model to have a flexible CN ratio in plant organs:

$$FN_{UPTK} = \min\{FN_{SPPL}, FN_{DMND}\}. \quad (A22)$$

Here, FN_{SPPL} is assumed simply as the total amount of inorganic N in soil ($=N_{NH4} + N_{NO3}$). The component FN_{DMND} is the sum of the demand from plant organs:

$$FN_{DMND} = FN_{DMND, CAN} + FN_{DMND, ROT} + FN_{DMND, STM} \quad (A23)$$

and

$$FN_{DMND, CAN} = (FC_{TRNS, CAN} - FC_{GRSP, CAN})/(C_{CAN}/N_{CAN}), \quad (A24)$$

$$FN_{DMND, ROT} = (FC_{TRNS, ROT} - FC_{GRSP, ROT})/(R_{ROT}), \quad (A25)$$

$$FN_{DMND, STM} = (FC_{TRNS, STM} - FC_{GRSP, STM})/(R_{STM}). \quad (A26)$$

In the above, FC_s represents the carbon flux of translocation of primary production (with subscript TRNS) and the carbon lost by growth respiration (GRSP). Subscripts CAN, ROT, and STM represent canopy, root, and stem, respectively.



R_{ROT} and R_{STM} are fixed parameters used as reference CN ratios in the root and stem, respectively, obtained from White et al., (2000). N_{CAN} is the canopy N that maximizes canopy productivity, which is determined numerically by considering the balance between GPP and canopy (foliage) respiration.

1320 A.2. Land use change

A.2.1. Structure of LUC tiles

LUC forced by external forcing and its impact on land biogeochemistry are simulated with five main types of tile (primary vegetation, secondary vegetation, urban, cropland, and pasture) in each land grid. The same structure of C and N compartments is shared among the tiles and each tile has its own areal fraction in a grid (f_{LUC}):

$$1325 \quad f_{LUC, PV} + f_{LUC, SV} + f_{LUC, UR} + f_{LUC, CR} + f_{LUC, PS} = 1 \quad (A27)$$

The crop tile further holds two subtiles and their areal fractions: nitrogen-fixing crops and others.

$$f_{LUC, CR} = f_{LUC, CRN} + f_{LUC, CRO} \quad (A28)$$

where $f_{LUC, CRN}$ is the areal fraction for the N-fixing crop and $f_{LUC, CRO}$ is for the others. This subtile-level fraction is used for the estimation of nitrogen fixation by crops (see Sect. A.2.3).

1330

A.2.2. Product pool and decomposition

The carbon and nitrogen in biomass removed by crop harvesting and by land use conversion (P) are allocated to three product pools with different turnover rates (1 year, 10 years, and 100 years):

$$dM_{PROD, 1yr}/dt = \epsilon_{1yr} \times P - FM_{LUCE, 1yr}, \quad (A29)$$

$$1335 \quad dM_{PROD, 10yr}/dt = \epsilon_{10yr} \times P - FM_{LUCE, 10yr}, \quad (A30)$$

$$dM_{PROD, 100yr}/dt = \epsilon_{100yr} \times P - FM_{LUCE, 100yr}, \quad (A31)$$

where M_{PROD} is the harvested biomass of C or N stored in the three product pools and P is harvested mass of C or N. Here, ϵ is the allocation fraction among the product pools (set in this study as $\epsilon_{1yr} = 0.5$, $\epsilon_{10yr} = 0.45$, and $\epsilon_{100yr} = 0.05$). FM_{LUCE} represents the volatilization rates of carbon (as CO_2) or nitrogen (as an inert form) from the three pools, which are calculated as follows:

1340

$$FM_{LUCE, 1yr} = K_{LUCE, 1yr} \times M_{PROD, 1yr}, \quad (A32)$$

$$FM_{LUCE, 10yr} = K_{LUCE, 10yr} \times M_{PROD, 10yr}, \quad (A33)$$

$$FM_{LUCE, 100yr} = K_{LUCE, 100yr} \times M_{PROD, 100yr}, \quad (A34)$$

where K_{LUCE} is the specific emission rate in each product pool, which is set to reduce the carbon/nitrogen in each pool by 99.9% within 1 year, 10 years, and 100 years.

1345

A.2.3. LUC status-driven impact on biogeochemistry



1350 Even if the areal fraction of each land use tile were fixed in a simulation, there could still be impacts of land use on land biogeochemistry, referred to here as the status-driven impact. This impact is specific to each tile and it is summarized as follows:

- (1) prohibition of plant growth on an urban tile;
- (2) increased mortality of plants by grazing pressure on pasture tiles, assuming a 20% increase of mortality rate for foliage;
- (3) annual crop harvesting on crop tiles (assuming 10% of foliage is harvested) and loss of C and N from the product pools;
- (4) nitrogen fixation by N-fixing crop on crop tiles.

For (4), the total BNF rate on crop tiles (FN_{SBNF}) is modeled as follows:

$$FN_{\text{SBNF}} = FN_{\text{SBNF, CRO}} \times f_{\text{LUC, CRO}} + FN_{\text{SBNF, CRN}} \times f_{\text{LUC, CRN}}, \quad (\text{A35})$$

1360 where $FN_{\text{SBNF, CRO}}$ represents the rate of nitrogen fixation on non-N-fixing crop tiles, which is assumed the same as that in natural vegetation. $FN_{\text{SBNF, CRN}}$ is the rate of nitrogen fixation on N-fixing crop tiles, which is calculated simply to satisfy a fixed ratio of BNF-derived N to all N taken up by N-fixing crops (=0.66; from Herridge et al. (2008)).

A.2.4. LUC transition-driven impact on biogeochemistry

1365 When the areal fractions of tiles are made to change following the forcing dataset, the apparent mass densities of C and N on a grid can be changed. For example, when a portion of a grid area is converted from category X to category Y in a year, the mass conservation between the “before (t)” and “after (t+1)” on a grid should be as follows:

$$M_X^t \times f_X^t + M_Y^t \times f_Y^t = M_X^{t+1} \times f_X^{t+1} + M_Y^{t+1} \times f_Y^{t+1} + P, \quad (\text{A36})$$

and

$$M_X^t = M_X^{t+1}, \quad (\text{A37})$$

1370 where M is the mass density per unit tile area, subscripts X and Y represent categories of land use type, and superscript t denotes time. By presenting the areal fraction change as Δf and the change in apparent mass density in category Y as ΔM_Y , these equations can be written as follows:

$$M_X^t \times f_X^t + M_Y^t \times f_Y^t = M_X^t \times (f_X^t - \Delta f) + (M_Y^t + \Delta M_Y) \times (f_Y^t + \Delta f) + P, \quad (\text{A38})$$

and

$$1375 \quad P = \Delta f \times M_X^t \times K_{\text{HARV}}, \quad (\text{A39})$$

where K_{HARV} determines the fraction of mass that enters the product pools instead of the tile of category Y. Here, K_{HARV} is always set to zero for litter and soil pools and $K_{\text{HARV}} = 1$ for vegetation pools in specific transition patterns (e.g., $K_{\text{HARV}} = 1$ if the LUC transition type is urbanization, whereas $K_{\text{HARV}} = 0$ if the LUC conversion is pasture abandonment). By solving the equations for ΔM_Y , we obtain the following:

$$1380 \quad \Delta M_Y = (\Delta f \times (M_X^t - M_Y^t) - P) / (f_Y^t + \Delta f). \quad (\text{A40})$$



If $\Delta M_Y > 0$ (< 0), the apparent mass density in tile Y is increased (decreased). The changes in apparent mass density lead to mass imbalance of C and N and therefore the storage of both C and N starts to move toward a rebalanced status under the given environmental conditions.

1385



Appendix B. Ocean ecosystem/biogeochemical component

B.1. Governing equations

The ocean ecosystem component (OECO2) embedded within the ocean circulation model is based on nutrient–phytoplankton–zooplankton–detritus (NPZD) type with four prognostic variables: nitrate (NO₃), “ordinary” nondiazotrophic phytoplankton (Phy), zooplankton (Zoo), and particulate detritus (Det). In addition, phosphate (PO₄), dissolved oxygen (O₂), dissolved iron (Fe), nitrous oxide (N₂O), and diazotrophic phytoplankton (nitrogen fixers, Diaz) are included. Biogeochemical tracers associated with the carbon cycle, i.e., dissolved inorganic carbon (DIC), alkalinity (Alk), calcium carbonate (CaCO₃), and calcium (Ca) are also included. Constant (~Redfield) stoichiometry relates the C, N, P, Fe, and O content of the biological variables and their exchanges with the inorganic variables (NO₃, PO₄, Fe, O₂, N₂O, Alk, and DIC).

Each variable changes its concentration C according to the following equation:

$$\frac{\partial C}{\partial t} = Tr + S, \quad (B1)$$

where Tr represents all transport terms associated with the physical processes, including advection, isopycnal and diapycnal diffusion, and convection, and S denotes the source minus sink terms that include the surface and bottom fluxes. Using the variables and parameters listed in Tables B1 and B2, the source minus sink terms for each prognostic variable can be obtained as follows.

First, the source minus sink term for NO₃ $S(\text{NO}_3)$ is given by the following:

$$S(\text{NO}_3) = G_{\text{NO}_3} (1 - 0.8R_{O:N} \Gamma_{\text{NO}_3} r_{\text{sox}}^{\text{NO}_3}) + \text{Dep}_{\text{NO}_3} + \text{Riv}_{\text{NO}_3}, \quad (B2)$$

where Dep_{NO_3} (Riv_{NO_3}) represents nitrogen deposition from the atmosphere (riverine input) and

$$G_{\text{NO}_3} = (\mu_D \text{Det} + \mu_P^* \text{Phy} + E_Z \text{Zoo} - J_o \text{Phy} - u_N J_D \text{Diaz}),$$

$$\Gamma_{\text{NO}_3} = \begin{cases} 1 & \text{if } \text{NO}_3 > \text{NO}_3^{\text{crit}}, \\ 0 & \text{if } \text{NO}_3 < \text{NO}_3^{\text{crit}}, \end{cases}$$

where J_o (J_D) is the growth rate of “ordinary” nondiazotrophic (diazotrophic) phytoplankton (see Appendix B2). The nitrate uptake rate is given by $u_N = \text{NO}_3 / (k_N^{\text{Diaz}} + \text{NO}_3)$ (Schmittner et al., 2005). Denitrification (Denit) can be expressed as follows:

$$\text{Denit} = G_{\text{NO}_3} (-0.8R_{O:N} \Gamma_{\text{NO}_3} r_{\text{sox}}^{\text{NO}_3}) - P_{\text{N}_2\text{O}},$$

where $P_{\text{N}_2\text{O}}$ is the source term of N₂O, which is discussed later. The source minus sink terms for Phy and Diaz, i.e., $S(\text{Phy})$ and $S(\text{Diaz})$, respectively, can be expressed as follows:

$$S(\text{Phy}) = J_o \text{Phy} - \mu_P^* \text{Phy} - m_{\text{Phy}} \text{Phy}^2 - \text{Graze}_{\text{Phy}}, \quad (B3)$$

$$S(\text{Diaz}) = J_D \text{Diaz} - m_{\text{Diaz}} \text{Diaz} - \text{Graze}_{\text{Diaz}}. \quad (B4)$$

The term $S(\text{zoo})$ is estimated as follows:

$$S(\text{Zoo}) = \gamma (\text{Graze}_{\text{Phy}} + \text{Graze}_{\text{Diaz}}) - E_Z \text{Zoo} - m_{\text{Zoo}} \text{Zoo}^2. \quad (B5)$$

Then, $S(\text{Det})$ is given by the following:



$$S(\text{Det}) = (1 - \gamma)(\text{Graze}_{\text{Phy}} + \text{Graze}_{\text{Diaz}}) + m_{\text{Phy}}\text{Phy}^2 + m_{\text{Diaz}}\text{Diaz} + m_{\text{Zoo}}\text{Zoo}^2 - \mu_D\text{Det} - \text{Fsed}_{\text{Det}} - \frac{\partial \text{Sink}_{\text{Det}}}{\partial z}, \quad (\text{B6})$$

1420

$$\text{Sink}_{\text{Det}} = \begin{cases} w_D\text{Det} & \text{if } z < 200\text{m} \\ \text{Sink}_{\text{Det}200} \left(\frac{z}{200}\right)^{0.875} & \text{if } z > 200\text{m} \end{cases}$$

where Fsed_{Det} represents the net flux of detritus between the ocean and ocean sediment (Kobayashi and Oka, 2018) and $\text{Sink}_{\text{Det}200}$ is the flux of sinking detritus at the depth of 200 m (Kawamiya et al., 2000).

Using the molar P:N ratio of organic matter, $R_{P:N}$, and the riverine input of phosphate (Riv_{PO_4}), the source minus sink term for PO4 becomes:

1425

$$S(\text{PO}_4) = R_{P:N}G_{\text{NO}_3} + \text{Riv}_{\text{PO}_4}. \quad (\text{B7})$$

As the land ecosystem model cannot simulate the phosphorus cycle, it is assumed that phosphate is brought to the river mouth at a rate to satisfy $\text{Riv}_{\text{NO}_3}:\text{Riv}_{\text{PO}_4} = 16:1$, similar to the Redfield ratio. The term $S(\text{O}_2)$ can be estimated as follows:

$$S(\text{O}_2) = -\Gamma_{\text{O}_2} R_{O:N}G_{\text{NO}_3} + \text{Fsf}c_{\text{O}_2}, \quad (\text{B8})$$

1430

$$\Gamma_{\text{O}_2} = \begin{cases} 1 & \text{if } \text{O}_2 > \text{O}_2^{\text{crit}} \\ 0 & \text{if } \text{O}_2 < \text{O}_2^{\text{crit}} \end{cases}$$

where $\text{Fsf}c_{\text{O}_2}$ is the dissolved oxygen exchange with the atmosphere, according to the OMIP protocol (Orr et al., 2017). The term $S(\text{Fe})$ can be expressed as follows:

$$S(\text{Fe}) = R_{Fe:N}G_{\text{NO}_3} + \text{Scav} + \text{Dustin} + \text{Sedin} + \text{HTin}, \quad (\text{B9})$$

where Scav represents scavenging (Moore et al., 2004; Moore and Braucher, 2008), Dustin is the iron input from dust, Sedin is the iron input from sediment following both Moore et al. (2004) and Aumont and Bopp (2006), and HTin is the hydrothermal dissolved iron flux following Tagliabue et al. (2010).

The source minus sink term for N_2O is linked to the consumption of oxygen during the remineralization of OM (Ilyina et al., 2013):

$$S(\text{N}_2\text{O}) = r_{\text{N}_2\text{O}}\Gamma_{\text{O}_2}R_{O:N}(\mu_D\text{Det} + \mu_P^*\text{Phy} + E_Z\text{Zoo}) + \text{Fsf}c_{\text{N}_2\text{O}}, \quad (\text{B10})$$

1440

where $\text{Fsf}c_{\text{N}_2\text{O}}$ is the N_2O exchange with the atmosphere according to Orr et al. (2017).

The source minus sink term for DIC can be expressed as follows:

$$S(\text{DIC}) = R_{C:N}G_{\text{NO}_3}(1 - 0.8R_{O:N}r_{\text{SOX}}^{\text{NO}_3}) - G_{\text{CaCO}_3} + \text{Fsf}c_{\text{DIC}}, \quad (\text{B11})$$

where $\text{Fsf}c_{\text{DIC}}$ is the DIC exchange with the atmosphere according to the OMIP protocol (Orr et al., 2017) and $G_{\text{CaCO}_3} = Pr_{\text{CaCO}_3} - Di_{\text{CaCO}_3}$.

1445

Then, $S(\text{Alk})$, $S(\text{CaCO}_3)$, and $S(\text{Ca})$ can be estimated, respectively, as follows:

$$S(\text{Alk}) = -2G_{\text{CaCO}_3} - G_{\text{NO}_3}, \quad (\text{B12})$$

$$S(\text{CaCO}_3) = G_{\text{CaCO}_3}, \quad (\text{B13})$$

$$S(\text{Ca}) = -G_{\text{CaCO}_3}. \quad (\text{B14})$$



1450

B.2. Growth rate of nondiazotrophic and diazotrophic phytoplankton

To simply evaluate the effect of iron limitation on the growth of “ordinary” nondiazotrophic phytoplankton and diazotrophic phytoplankton (nitrogen fixers), we modify the equations of phytoplankton growth rate by Keller et al. (2012) as follows. First, we estimate the maximum potential growth rate of phytoplankton (J_O^{\max}) and diazotrophic plankton (J_D^{\max}) that depend on temperature (T):

$$J_O^{\max} = ae^{(T/T_b)}, \quad (\text{B15})$$

$$J_D^{\max} = c_D \max(0, a(e^{(T/T_b)} - 2.61)) \quad (\text{B16})$$

(Schmittner et al., 2008).

Once the maximum potential growth rate has been calculated, the realized growth rate of phytoplankton (J_O) is then determined by irradiance (I) and the concentrations of NO_3 , Fe and PO_4 , while the growth rate of diazotrophic plankton (J_D) is determined by irradiance (I) and the concentrations of Fe and PO_4 :

$$J_O = \min\left(J_{OI}, J_O^{\max} \frac{\text{NO}_3}{k_N + \text{NO}_3}, J_O^{\max} \frac{\text{Fe}}{k_{\text{Fe}} + \text{Fe}}, J_O^{\max} \frac{\text{PO}_4}{k_P + \text{PO}_4}\right), \quad (\text{B17})$$

$$J_D = \min\left(J_{DI}, J_D^{\max} \frac{\text{Fe}}{k_{\text{Fe}} + \text{Fe}}, J_D^{\max} \frac{\text{PO}_4}{k_P + \text{PO}_4}\right). \quad (\text{B18})$$

J_{OI} and J_{DI} in (B17) and (B18) represent the light-limited growth rate of phytoplankton and diazotrophic phytoplankton, respectively, given by $J_{OI} = \frac{J_O^{\max} \alpha I}{\sqrt{(J_O^{\max})^2 + (\alpha I)^2}}$ and $J_{DI} = \frac{J_D^{\max} \alpha I}{\sqrt{(J_D^{\max})^2 + (\alpha I)^2}}$, where $\alpha = 0.1 \text{ d}^{-1}$ and I is shortwave radiation at each depth (see (14) of Keller et al. (2012)).

1470 **Table B1.**

Model parameters.

Parameter	Sym bol	Value	Unit
Fast recycling term (microbial loop)	μ_P^*	0.05	d^{-1}
Excretion of zooplankton	E_Z	0.03	d^{-1}
Critical NO_3 concentration of denitrification	$\text{NO}_3_{\text{crit}}$	1	$\mu\text{mol L}^{-1}$
Critical O_2 concentration of remineralization	O_2_{crit}	4	$\mu\text{mol L}^{-1}$
Molar O:N ratio	$R_{O:N}$	8.625	N.D.



Molar P:N ratio	$R_{P:N}$	0.0625	N.D.
Molar Fe:N ratio	$R_{Fe:N}$	4.4167×10^{-5}	N.D.
Molar C:N ratio	$R_{C:N}$	6.625	N.D.
Half-saturation constant for N uptake	k_N^{Diaz}	0.05	$\mu\text{mol L}^{-1}$
Phytoplankton mortality rate	m_{Phy}	0.05	$\text{d}^{-1} (\mu\text{mol L}^{-1})^{-1}$
Diazotroph mortality rate	m_{Diaz}	0.025	d^{-1}
Zooplankton mortality rate	m_{Zoo}	0.2	$\text{d}^{-1} (\mu\text{mol L}^{-1})^{-1}$
Assimilation efficiency coefficient	γ	0.75	N.D.
Sinking speed at the depth of 0–200 m	w_D	5	m d^{-1}
Maximum potential growth rate of nondiazotrophic phytoplankton at 0°C	α	0.8	d^{-1}
Diazotroph handicap	c_D	0.5	N.D.
E-folding temperature of biological rates	T_b	15.65	°C
Half-saturation constants for NO ₃ uptake	k_N	0.5	$\mu\text{mol L}^{-1}$
Half-saturation constant for PO ₄ uptake	k_P	0.5	$\mu\text{mol L}^{-1}$
Half-saturation constant for iron uptake	k_{Fe}	10^{-3}	nmol L^{-1}

Table B2.

1475 Definitions of parameters and variables not mentioned specifically in the text.

Parameter or variable	Definition	Reference
$r_{\text{sox}}^{\text{NO}_3}$	Oxygen-equivalent oxidation of nitrate in suboxic waters (i.e., denitrification)	Equation (A18) in Schmittner et al. (2008)
μ_D	Temperature and O ₂ dependent rate of detritus remineralization	Equation (A16) in Schmittner et al. (2008)
α	Initial slope of P–I curve	Table A1 in Schmittner et al.



		(2008)
$Graze_{phy}$	Grazing rate of zooplankton on nondiazotrophic phytoplankton	Schmitter et al. (2005)
$Graze_{Diaz}$	Grazing rate of zooplankton on diazotrophic phytoplankton	Schmitter et al. (2005)
Pr_{CaCO_3}	Production of calcium carbonate	Schmittner et al. (2008)
Di_{CaCO_3}	Dissolution of calcium carbonate	Schmittner et al. (2008)
I	Shortwave radiation at each depth	Equation (14) in Keller et al. (2012)
r_{N_2O}	N_2O production rate	Broecker and Peng (1982)

Appendix C. Forcing data

1480 External forcing used for HIST experiment is summarized in Table C1.

Table C1.

List of forcing datasets for HIST simulation: categories, variables, and references for the data creation and description of how the datasets are applied in the HIST simulation in MIROC-ES2L.

1485

Category	Variables	Reference	Treatment in MIROC-ES2L
GHG concentration	CO_2 , CH_4 , N_2O , CFC11, CFC12, CFC113, CFC114, CFC115, HCFC22, HCFC123, HCFC141b, HCFC142b, HFC32, HFC125, HFC134a, HFC143a, SF_6 , CCl_4 , C_2F_6	Meinshausen et al. (2017)	Same as Tatebe et al. (2019): given as globally averaged annual concentration
Anthropogenic SLCF emission	BC, OC, SO_2	Hoesly et al. (2018)	Same as Tatebe et al. (2019): given as monthly emissions
Open biomass burning emission	BC, OC, SO_2	van Marle et al. (2017)	Same as Tatebe et al. (2019): given as monthly emissions
Atmospheric chemical composition for aerosol scheme	H_2O_2 , OH radical, NO_3	Precalculated from atmospheric chemistry model CHASER: Sudo et al. (2002)	Same as Tatebe et al. (2019): given as three-dimensional concentration with monthly interval
Anthropogenic dissolved iron emission	Dissolved Fe	Biomass burning emission diagnosed from BC emission (van Marle et al., 2017; Ito, 2011); fossil fuel and biofuel emission (Hoesly et al., 2018; Ito et al., 2018)	Given as monthly emission of biomass burning emission and fossil fuel/biofuel emissions
Nitrogen deposition	NO_y (wet and dry), NH_y (wet and dry)	IGAC/SPARC CCMI: http://blogs.reading.ac.uk/ccmi/forcing-databases-in-support-of-cmip6/	Given as wet plus dry monthly deposition for both NO_y and NH_y
Land use	Status, transition, fertilizer	Ma et al. (2019)	Given as two types of land use status (non-agriculture and



			agriculture) for energy/hydrology processes; given as transition matrix among five land use types (primary, secondary, urban, crop, and pasture) for biogeochemistry; given as cropland fertilizer
Stratospheric aerosol	Extinction coefficient	Thomason et al. (https://www.wcrp-climate.org/)	Same as Tatebe et al. (2019): monthly vertically integrated extinction coefficients for each radiation band
Ozone concentration	O ₃	Hegglin et al. (in prep.)	Same as Tatebe et al. (2019): given as three-dimensional concentration with monthly interval
Solar	Solar spectral irradiance	Matthes et al. (2017)	Same as Tatebe et al. (2019): given as monthly solar irradiance spectra

Appendix D. Diagnosis of atmospheric CO₂ concentration

1490 The global carbon budget can be written as follows:

$$CE = CA + CL + CO,$$

where CE is the cumulative emission derived from fossil fuel and industry. CA, CL, and CO represent the changes in carbon amount in the atmosphere, land, and ocean, respectively. When models are forced with prescribed CO₂ concentration (CA), both CL and CO are diagnosed in the simulations. By expressing the prescribed CA as CA^P, the

1495 budget equation can be described as:

$$CE^D = CA^P + CL + CO, \tag{C1}$$

where CE^D is a diagnosed fossil fuel/industrial carbon emission. This diagnosis of CE^D was used in the analysis of Jones et al. (2013). If we can obtain the prescribed emission (CE^P) that is consistent with historical atmospheric CO₂ concentration change, we can diagnose CO₂ concentration (CA^D) as follows:

$$1500 \quad CA^D = CE^P - CL - CO. \tag{C2}$$

For CMIP6, CE^P during 1850–2014 is approximately 403 PgC, and the values of CL and CO in this study were 44 and 163 PgC, respectively. Thus, CA^D in this study was 193 PgC. This is equivalent to the CO₂ concentration change of 91 ppmv determined using a conversion factor of 2.12 (PgC ppmv⁻¹). Consequently, we can obtain the diagnosed CO₂ concentration at the end of simulation (2014) of 376 ppmv. We note the estimate of anthropogenic CO₂ emission of fossil fuel and industry has its uncertainty range, e.g., Le Quéré et al. (2018) estimate the cumulative emission as 400 ± 20 PgC

1505 1850–2014; however, it was not considered in this study. In addition, there is a budget imbalance of 25 PgC in Le Quéré et al. (2018), which was also ignored in this study.

Appendix E. Feedback parameters of carbon cycle with same unit

1510 As in Appendix D, the global carbon budget can be written as follows:

$$CE = CA + CL + CO. \tag{E1}$$



Following Gregory et al. (2009), this carbon budget equation can relate the feedback parameters of land and ocean to AF. First, following the definition, CL and CO can be expressed by the feedback parameters of CO₂-carbon and climate-carbon feedbacks (β and γ , respectively) as follows:

1515 $CL = \beta_L CA + \gamma_L T,$ (E2)

$$CO = \beta_O CA + \gamma_O T, \quad (E3)$$

where CA is the carbon increase in the atmosphere and T is global temperature change (T). Using Eqs. E1–E3, the global carbon budget equation can be written as follows:

$$CE = CA + CA (\beta_L + \beta_O) + T (\gamma_L + \gamma_O). \quad (E4)$$

1520 Dividing both sides of the equation by CA leads to the following:

$$CE/CA = 1 + (\beta_L + \beta_O) + T (\gamma_L + \gamma_O)/CA. \quad (E5)$$

Then, we define $T/CA = \alpha$, as used by Friedlingstein et al. (2006) or Arora et al. (2013), and we replace CE/CA by 1/AF (because $AF = CA/CE$):

$$1/AF = 1 + (\beta_L + \beta_O) + \alpha (\gamma_L + \gamma_O). \quad (E6)$$

1525 The “u” quantity proposed by Gregory et al. (2009) is $u_{\beta L} = \beta_L$; $u_{\beta O} = \beta_O$; $u_{\gamma L} = \alpha \gamma_L$; and $u_{\gamma O} = \alpha \gamma_O$. Through replacement with the u terms, Eq. E6 can be expressed as follows:

$$1/AF = 1 + u_{\beta L} + u_{\beta O} + u_{\gamma L} + u_{\gamma O}, \quad (E7)$$

and thus we obtain the following:

$$AF = 1/(1 + u_{\beta L} + u_{\beta O} + u_{\gamma L} + u_{\gamma O}). \quad (E8)$$

1530 As AF has the unit of PgC PgC⁻¹, the unit of the u parameters is also dimensionless.



6. Author contributions

TH was responsible for the development and description of MIROC-ES2L and VISIT-e, executed the spin-up and experiments, and undertook global analyses of climate–biogeochemistry and the terrestrial analysis. MW, AY, and MN contributed to the development and description of OECO2, as well as the analysis of ocean biogeochemistry. HT developed MIROC5.2 and supervised the physical modeling and engineering. MA contributed to the DMS emission modeling, preparation of the forcing dataset, and conversion and archiving of the output. RO contributed to the examination of model performance, postprocessing of the output, and analysis of the physical fields. AI¹ contributed to the development of atmospheric iron transport, preparation of iron emission forcing, and its description. DY contributed to river nitrogen modeling and its analysis. HO contributed to the coupling of OECO2. AI³ provided the original model VISIT and supervised the modeling and analysis of the terrestrial biogeochemistry. KT supervised the modeling of the terrestrial physical processes. KO supervised and supported the software engineering. SW determined the primitive design of MIROC-ES2L and supervised the entire system. MK organized the project, supervised the entire system, and contributed to the background section.

7. Competing interests

The authors declare that they have no conflict of interest.

8. Code and data availability

The code of MIROC-ES2L are not publicly archived because of the copyright policy of MIROC community. Readers are requested to contact the corresponding author if they wish to validate the model configurations of MIROC-ES2L and conduct replication experiments. The source codes, required input data, and simulation results will be provided by the modeling community to which the author belongs. The model output of the control, historical, and 1%CO2 increase simulations performed in this study will be distributed and made freely available through the Earth System Grid Federation (ESGF). Details on the ESGF can be found on the website of the CMIP Panel (<https://www.wcrp-climate.org/wgcm-cmip/wgcm-cmip6>, last access: 28 August 2019).

9. Acknowledgments

This work was supported by TOUGOU/SOUSEI, the “Integrated Research Program for Advancing Climate Models”/“Program for Risk Information on Climate Change”, by the Ministry of Education, Culture, Sports, Science, and Technology of Japan. This work was also partly supported by JSPS KAKENHI Grant Number 17K12820 and by scientific collaboration in GCOM-C RA (JX-PSPC-500211). The Earth Simulator and JAMSTEC Super Computing System were used for the simulations, and the administration staff provided much supports. The authors are grateful for the programming support provided by Tsuyoshi Hasegawa and Shinichi Toshimitsu and for the engineering advice offered by Hiroaki Kanai. Osamu Arakawa provided powerful support and services on data archiving and server management. Kengo Sudo and Tomoko Nitta kindly provided the forcing data and the forcing preparation system, respectively. Kaoru Tachiiri provided helpful and encouraging comments. This work was based on the long-term endeavor of members of the MIROC



community. We thank James Buxton MSc from Edanz Group (www.edanzediting.com/ac) for editing a draft of this manuscript.



1570 **10. References**

- Adler, R. F., Huffman, G. J., Chang, A., Ferraro, R., Xie, P., Janowiak, J., Rudolf, B., Schneider, U., Curtis, S., Bolvin, D., Gruber, A., Susskind, J. and Arkin, P.: The Version-2 Global Precipitation Climatology Project (GPCP) Monthly Precipitation Analysis (1979–Present), *J. Hydrometeorol.*, 4(6), 1147–1167, 2003.
- 1575 Allen, M. R., Frame, D. J., Huntingford, C., Jones, C. D., Lowe, J. A., Meinshausen, M. and Meinshausen, N.: Warming caused by cumulative carbon emissions towards the trillionth tonne, *Nature*, 458(7242), 1163–1166, doi:10.1038/nature08019, 2009.
- Anav, A., Friedlingstein, P., Kidston, M., Bopp, L., Ciais, P., Cox, P., Jones, C., Jung, M., Myneni, R. and Zhu, Z.: Evaluating the land and ocean components of the global carbon cycle in the CMIP5 earth system models, *J. Clim.*, 26(18), 1580 6801–6843, doi:10.1175/JCLI-D-12-00417.1, 2013.
- Arora, V. K., Boer, G. J., Friedlingstein, P., Eby, M., Jones, C. D., Christian, J. R., Bonan, G., Bopp, L., Brovkin, V., Cadule, P., Hajima, T., Ilyina, T., Lindsay, K., Tjiputra, J. F. and Wu, T.: Carbon-concentration and carbon–climate feedbacks in CMIP5 Earth system models, *J. Clim.*, 26(15), 130208091306008, doi:10.1175/JCLI-D-12-00494.1, 2013.
- Aumont, O. and Bopp, L.: Globalizing results from ocean in situ iron fertilization studies, *Global Biogeochem. Cycles*, 1585 20(2), 1–15, doi:10.1029/2005GB002591, 2006.
- Batjes, N. H.: Harmonized soil property values for broad-scale modelling (WISE30sec) with estimates of global soil carbon stocks, *Geoderma*, 269(February), 61–68, doi:10.1016/j.geoderma.2016.01.034, 2016.
- Behrenfeld, M. J. and Falkowski, P. G.: Photosynthetic rates derived from satellite-based chlorophyll concentration, *Limnol. Oceanogr.*, 42(1), 1–20, 1997.
- 1590 Bellucci, A., Gualdi, S. and Navarra, A.: The double-ITCZ syndrome in coupled general circulation models: The role of large-scale vertical circulation regimes, *J. Clim.*, 23(5), 1127–1145, doi:10.1175/2009JCLI3002.1, 2010.
- Beusen, A. H. W., Bouwman, A. F., Van Beek, L. P. H., Mogollón, J. M. and Middelburg, J. J.: Global riverine N and P transport to ocean increased during the 20th century despite increased retention along the aquatic continuum, *Biogeosciences*, 13(8), 2441–2451, doi:10.5194/bg-13-2441-2016, 2016.
- 1595 Bianchi, D., Dunne, J. P., Sarmiento, J. L. and Galbraith, E. D.: Data-based estimates of suboxia, denitrification, and N₂O production in the ocean and their sensitivities to dissolved O₂, *Global Biogeochem. Cycles*, 26(May), 1–13, doi:10.1029/2011GB004209, 2012.
- Boer, G. J. and Arora, V.: Temperature and concentration feedbacks in the carbon cycle, *Geophys. Res. Lett.*, 36, L02704, doi:10.1029/2008GL036220, 2009.
- 1600 Bopp, L., Resplandy, L., Orr, J. C., Doney, S. C., Dunne, J. P., Gehlen, M., Halloran, P., Heinze, C., Ilyina, T., Séférian, R., Tjiputra, J. and Vichi, M.: Multiple stressors of ocean ecosystems in the 21st century: Projections with CMIP5 models, *Biogeosciences*, 10(10), 6225–6245, doi:10.5194/bg-10-6225-2013, 2013.



- Boyer, E., Howarth, R., Galloway, J., Dentener, F., Green, P. and Vörösmarty, C.: Riverine nitrogen export from the continents to the coasts, *Global Biogeochem. Cycles*, 20(GB1S91), 1–9, doi:10.1029/2005GB002537, 2006.
- 1605 Broecker, W. and Peng, T.: Tracers in the Sea, in Lamont-Doherty Geol. Observatory, p. 690, Columbia University, ELDIGIO press, New York., 1982.
- Carr, M., Friedrichs, M. A. M., Schmeltz, M., Noguchi, M., Antoine, D., Arrigo, K. R., Asanuma, I., Aumont, O., Barber, R., Behrenfeld, M., Bidigare, R., Buitenhuis, E. T., Campbell, J., Ciotti, A., Dierssen, H., Dowell, M., Dunne, J., Esaias, W., Gentili, B., Gregg, W., Groom, S., Hoepffner, N., Ishizaka, J., Kameda, T., Que, C. Le, Reddy, T. E., Ryan, J., Scardi, M., Moore, K., Smyth, T., Turpie, K., Tilstone, G., Waters, K. and Yamanaka, Y.: A comparison of global estimates of marine primary production from ocean color, *Deep. Sea Res. Part II*, 53, 741–770, doi:10.1016/j.dsr2.2006.01.028, 2006.
- 1610 Ciais, P., Sabine, C., Bala, G., Bopp, L., Brovkin, V., Canadell, J., Chhabra, A., DeFries, R., Galloway, J., Heimann, M., Jones, C., Le Quéré, C., Myneni, R. B., Piao, S. and Thornton, P.: Carbon and other Biogeochemical Cycles, in *Climate Change 2013 the Physical Science Basis: Working Group I Contribution to the Fifth Assessment Report of the Intergovernmental Panel on Climate Change*, edited by T. F. Stocker, D. Qin, G.-K. Plattner, M. Tignor, S. K. Allen, J. Boschung, A. Nauels, Y. Xia, V. Bex, and P. M. Midgley, Cambridge University Press, Cambridge, United Kingdom and New York, NY, USA., 2013.
- 1620 Cleveland, C. C., Townsend, A. R., Schimel, D. S., Fisher, H., Howarth, R. W., Hedin, L. O., Perakis, S. S., Latty, E. F., Von Fischer, J. C., Hlseroad, A. and Wasson, M. F.: Global patterns of terrestrial biological nitrogen (N_2) fixation in natural ecosystems, *Global Biogeochem. Cycles*, 23, 623–645, doi:10.1002/(ISSN)1944-9224, 1999.
- Cocco, V., Joos, F., Steinacher, M., Frölicher, T. L., Bopp, L., Dunne, J., Gehlen, M., Heinze, C., Orr, J., Oschlies, A., Schneider, B., Segsneider, J. and Tjiputra, J.: Oxygen and indicators of stress for marine life in multi-model global warming projections, *Biogeosciences*, 10, 1849–1868, doi:10.5194/bg-10-1849-2013, 2013.
- 1625 Codispoti, L. A., Brandes, J. A., Christensen, J. P., Devol, A. H., Naqvi, S. W. A., Paerl, H. W. and Yoshinari, T.: The oceanic fixed nitrogen and nitrous oxide budgets: Moving targets as we enter the Anthropocene? *Sci. Mar.*, 65(S2), 85–105, doi:10.3989/scimar.2001.65s285, 2001.
- 1630 Collins, W. J., Bellouin, N., Doutriaux-Boucher, M., Gedney, N., Halloran, P., Hinton, T., Hughes, J., Jones, C. D., Joshi, M. and Liddicoat, S.: Development and evaluation of an Earth-system model—HadGEM2, *Geosci. Model Dev. Discuss*, 4, 997–1062, doi:10.5194/gmd-4-1051-2011, 2011.
- Collins, W. J., Webber, C. P., Cox, P. M., Huntingford, C., Lowe, J., Sitch, S., Chadburn, S. E., Comyn-Platt, E., Harper, A. B., Hayman, G. and Powell, T.: Increased importance of methane reduction for a 1.5 degree target, *Environ. Res. Lett.*, 13(5), 054003, doi:10.1088/1748-9326/aab89c, 2018.
- 1635 Cox, P. M., Betts, R. A., Jones, C. D., Spall, S. A. and Totterdell, I. J.: Acceleration of global warming due to carbon-cycle feedbacks in a coupled climate model, *Nature*, 408(6813), 184–187, doi:10.1038/35041539, 2000.
- Dee, D. P., Uppala, S. M., Simmons, A. J., Berrisford, P., Poli, P., Kobayashi, S., Andrae, U., Balmaseda, M. A., Balsamo, G., Bauer, P., Bechtold, P., Beljaars, A. C. M., van de Berg, L., Bidlot, J., Bormann, N., Delsol, C., Dragani, R., Fuentes, M., Geer, A. J., Haimberger, L., Healy, S. B., Hersbach, H., Hólm, E. V., Isaksen, L., Kållberg, P., Köhler, M., Matricardi, M., McNally, A. P., Monge-Sanz, B. M., Morcrette, J. J., Park, B. K., Peubey, C., de Rosnay, P., Tavolato, C.,



- 1640 Thépaut, J. N. and Vitart, F.: The ERA-Interim reanalysis: Configuration and performance of the data assimilation system, *Q. J. R. Meteorol. Soc.*, 137(656), 553–597, doi:10.1002/qj.828, 2011.
- Devries, T., Deutsch, C., Primeau, F., Chang, B. and Devol, A.: Global rates of water-column denitrification derived from nitrogen gas measurements, *Nat. Geosci.*, 5(8), 547–550, doi:10.1038/ngeo1515, 2012.
- Duce, R. A. and Tindale, N. W.: Atmospheric transport of iron and its deposition in the ocean, *Limnol. Oceanogr.*, 1645 36(8), 1715–1726, doi:10.4319/lo.1991.36.8.1715, 1991.
- Duce, R. A., La Roche, J., Altieri, K., Arrigo, K. R., Baker, A. R., Capone, D. G., Cornell, S., Dentener, F., Galloway, J., Ganeshram, R. S., Geider, R. J., Jickells, T., Kuypers, M. M., Langlois, R., Liss, P. S., Liu, S. M., Middelburg, J. J., Moore, C. M., Nickovic, S., Oschlies, A., Pedersen, T., Prospero, J., Schlitzer, R., Seitzinger, S., Sorensen, L. L., Uematsu, M., Ulloa, O., Voss, M., Ward, B. and Zamora, L.: Impacts of atmospheric anthropogenic nitrogen on the open ocean, 1650 *Science*, 320(5878), 893–897, doi:10.1126/science.1150369, 2008.
- Dumont, E., Harrison, J. A., Kroeze, C., Bakker, E. J. and Seitzinger, S. P.: Global distribution and sources of dissolved inorganic nitrogen export to the coastal zone: Results from a spatially explicit, global model, *Global Biogeochem. Cycles*, 19(4), 1–14, doi:10.1029/2005GB002488, 2005.
- Elrod, V. A., Berelson, W. M., Coale, K. H. and Johnson, K. S.: The flux of iron from continental shelf sediments: A 1655 missing source for global budgets, *Geophys. Res. Lett.*, 31(L12307), doi:10.1029/2004GL020216, 2004.
- Endresen, Ø., Sørga, E., Behrens, H. L., Brett, P. O. and Isaksen, I. S. A.: A historical reconstruction of ships' fuel consumption and emissions, *J. Geophys. Res. Atmos.*, 112(D12301), 1–17, doi:10.1029/2006JD007630, 2007.
- Eugster, O. and Gruber, N.: A probabilistic estimate of global marine N-fixation and denitrification, *Global Biogeochem. Cycles*, 26(4), 1–15, doi:10.1029/2012GB004300, 2012.
- 1660 Eyring, V., Bony, S., Meehl, G. A., Senior, C. A., Stevens, B., Stouffer, R. J. and Taylor, K. E.: Overview of the Coupled Model Intercomparison Project Phase 6 (CMIP6) experimental design and organization, *Geosci. Model Dev.*, 9, 1937–1958, doi:10.5194/gmd-9-1937-2016, 2016.
- FAO/IIASA/ISRIC/ISS-CAS/JRC: Harmonized World Soil Database (version 1.2), FAO, Rome, Italy and IIASA, Laxenburg, Austria. [online] Available from: [http://www.fao.org/soils-portal/soil-survey/soil-maps-and-](http://www.fao.org/soils-portal/soil-survey/soil-maps-and-databases/harmonized-world-soil-database-v12/en/) 1665 [databases/harmonized-world-soil-database-v12/en/](http://www.fao.org/soils-portal/soil-survey/soil-maps-and-databases/harmonized-world-soil-database-v12/en/), 2012.
- Fletcher, M. E.: *From Coal to Oil in British Shipping*, edited by D. M. Williams, Ashgate Publishing, Brookfield, UK, 1997.
- Friedlingstein, P., Cox, P., Betts, R., Bopp, L., von Bloh, W., Brovkin, V., Cadule, P., Doney, S., Eby, M., Fung, I., Bala, G., John, J., Jones, C., Joos, F., Kato, T., Kawamiya, M., Knorr, W., Lindsay, K., Matthews, H. D., Raddatz, T., 1670 Rayner, P., Reick, C., Roeckner, E., Schnitzler, K.-G., Schnur, R., Strassmann, K., Weaver, A. J., Yoshikawa, C. and Zeng, N.: Climate–carbon cycle feedback analysis: Results from the C⁴MIP model intercomparison, *J. Clim.*, 19(14), 3337–3353, doi:10.1175/JCLI3800.1, 2006.
- Friedlingstein, P., Meinshausen, M., Arora, V. K., Jones, C. D., Anav, A., Liddicoat, S. K. and Knutti, R.: Uncertainties in CMIP5 climate projections due to carbon cycle feedbacks, *J. Clim.*, 27(2), 511–526, doi:10.1175/JCLI-D-12-00579.1, 1675 2014.



- Frölicher, T. L., Sarmiento, J. L., Paynter, D. J., Dunne, J. P., Krasting, J. P. and Winton, M.: Dominance of the Southern Ocean in anthropogenic carbon and heat uptake in CMIP5 models, *J. Clim.*, 28(2), 862–886, doi:10.1175/JCLI-D-14-00117.1, 2015.
- 1680 Fu, W., Randerson, J. T. and Keith Moore, J.: Climate change impacts on net primary production (NPP) and export production (EP) regulated by increasing stratification and phytoplankton community structure in the CMIP5 models, *Biogeosciences*, 13(18), 5151–5170, doi:10.5194/bg-13-5151-2016, 2016.
- Galloway, J. N., Dentener, F. J., Capone, D. G., Boyer, E. W., Howarth, R. W., Seitzinger, S. P., Asner, G. P., Cleveland, C. C., Green, P. A., Holland, E. A., Karl, D. M., Michaels, A. F., Porter, J. H., Townsend, A. R. and Vörösmarty, C. J.: Nitrogen cycles: Past, present, and future, *Biogeochemistry*, 70, 153–226, 2004.
- 1685 Galloway, J. N., Townsend, A. R., Erisman, J. W., Bekunda, M., Cai, Z., Freney, J. R., Martinelli, L. A., Seitzinger, S. P. and Sutton, M. A.: Transformation of the nitrogen cycle: Recent trends, questions, and potential solutions, *Science*, 320(5878), 889–892, doi:10.1126/science.1136674, 2008.
- Garcia, H. E., Locamini, R. A., Boyer, T. P., Antonov, J. I., Baranova, O., Zweng, M., Reagan, J. and Johnson, D.: World Ocean Atlas 2013: Dissolved Oxygen, Apparent Oxygen Utilization, and Oxygen Saturation, Vol. 3, in Atlas NESDIS 75, edited by S. Levitus and A. Mishonov, p. 27, NOAA, US Government Printing Office, Washington DC, USA, 2014a.
- 1690 Garcia, H. E., Locamini, R. A., Boyer, T. P., Antonov, J. I., Baranova, O., Zweng, M., Reagan, J. and Johnson, D.: World Ocean Atlas 2013: Dissolved Inorganic Nutrients (phosphate, nitrate, silicate), Vol. 4, in Atlas NESDIS 76, edited by S. Levitus and A. Mishonov, p. 25, NOAA, US Government Printing Office, Washington DC, USA, 2014b.
- 1695 Gillett, N. P., Arora, V. K., Matthews, D. and Allen, M. R.: Constraining the ratio of global warming to cumulative CO₂ emissions using CMIP5 simulations, *J. Clim.*, 26(18), 6844–6858, doi:10.1175/JCLI-D-12-00476.1, 2013.
- Green, P. A., Vörösmarty, C. J., Meybeck, M., Galloway, J. N., Peterson, B. J. and Boyer, E. W.: Pre-industrial and contemporary fluxes of nitrogen through rivers: A global assessment based on typology, *Biogeochemistry*, 68(1), 71–105, doi:10.1023/B:BIOG.0000025742.82155.92, 2004.
- 1700 Gregg, W. W., Ginoux, P., Schopf, P. S. and Casey, N. W.: Phytoplankton and iron: Validation of a global three-dimensional ocean biogeochemical model, *Deep Sea Res. Part II Top. Stud. Oceanogr.*, 50(22–26), 3143–3169, doi:10.1016/j.dsr2.2003.07.013, 2003.
- Gregory, J. M., Jones, C. D., Cadule, P. and Friedlingstein, P.: Quantifying carbon cycle feedbacks, *J. Clim.*, 22(19), 5232–5250, doi:10.1175/2009JCLI2949.1, 2009.
- 1705 Gruber, N. and Galloway, J. N.: An Earth-system perspective of the global nitrogen cycle, *Nature*, 451(7176), 293–296, doi:10.1038/nature06592, 2008.
- Hajima, T., Ise, T., Tachiiri, K., Kato, E., Watanabe, S. and Kawamiya, M.: Climate change, allowable emission, and Earth system response to representative Concentration Pathway scenarios, *J. Meteorol. Soc. Japan. Ser. II*, 90(3), 417–434, doi:10.2151/jmsj.2012-305, 2012.
- 1710 Hajima, T., Kawamiya, M., Watanabe, M., Kato, E., Tachiiri, K., Sugiyama, M., Watanabe, S., Okajima, H. and Ito, A.: Modeling in Earth system science up to and beyond IPCC AR5, *Prog. Earth Planet. Sci.*, 1(1), 1–25, doi:10.1186/s40645-014-0029-y, 2014a.



- Hajima, T., Tachiiri, K., Ito, A. and Kawamiya, M.: Uncertainty of concentration–terrestrial carbon feedback in earth system models, *J. Clim.*, 27(9), 3425–3445, doi:10.1175/JCLI-D-13-00177.1, 2014b.
- 1715 Hall, D. K., Riggs, G. A. and Salomonson, V. V.: MODIS/Terra Snow Cover 5-Min L2 Swath 500m. Version 5, NASA National Snow and Ice Data Center Distributed Active Archive Center, Boulder CO, USA, 2006.
- Hashimoto, S.: A new estimation of global soil greenhouse gas fluxes using a simple data-oriented model, *PLoSOne*, 7(8), e41962, doi:10.1371/journal.pone.0041962, 2012.
- Hasumi, H.: CCSR Ocean Component Model (COCO) version 4.0, CCSR Rep. 25. 103pp. [online] Available from: 1720 <https://ccsr.ori.u-tokyo.ac.jp/~hasumi/COCO/coco4.pdf>, (last accessed: 19 September 2019) 2006.
- Hegglin, M. I., Kinnison, D., Plummer, D. et al.: Historical and future ozone database (1850–2100) in support of CMIP6, *Geosci. Model Dev.*, in prep.
- Herridge, D. F., Peoples, M. B. and Boddey, R. M.: Global inputs of biological nitrogen fixation in agricultural systems, *Plant Soil*, 311(1–2), 1–18, doi:10.1007/s11104-008-9668-3, 2008.
- 1725 Hoesly, R. M., Smith, S. J., Feng, L., Klimont, Z., Janssens-Maenhout, G., Dawidowski, L., Kholod, N., Kurokawa, J., Li, M., Liu, L. and Lu, Z.: Historical (1750–2014) anthropogenic emissions of reactive gases and aerosols from the Community Emissions Data System (CEDS), *Geosci. Model Dev.*, 11, 369–408, doi:https://www.geosci-model-dev.net/11/369/2018/, 2018.
- Hosoda, S., Ohira, T., Sato, K. and Suga, T.: Improved description of global mixed-layer depth using Argo profiling floats, *J. Oceanogr.*, 66(6), 773–787, 2010.
- 1730 Hugelius, G., Bockheim, J. G., Camill, P., Elberling, B., Grosse, G., Harden, J. W., Johnson, K., Jorgenson, T., Koven, C. D., Kuhry, P., Michaelson, G., Mishra, U., Palmtag, J., O’Donnell, J., Schirrmeister, L., Schuur, E. A. G., Sheng, Y., Smith, L. C., Strauss, J. and Yu, Z.: A new data set for estimating organic carbon storage to 3 m depth in soils of the northern circumpolar permafrost region, *Earth Syst. Sci. Data*, 5, 393–402, doi:10.5194/essd-5-393-2013, 2013.
- 1735 Hyder, P., Edwards, J. M., Allan, R. P., Hewitt, H. T., Bracegirdle, T. J., Gregory, J. M., Wood, R. A., Meijers, A. J. S., Mulcahy, J., Field, P., Furtado, K., Bodas-Salcedo, A., Williams, K. D., Copsey, D., Josey, S. A., Liu, C., Roberts, C. D., Sanchez, C., Ridley, J., Thorpe, L., Hardiman, S. C., Mayer, M., Berry, D. I. and Belcher, S. E.: Critical Southern Ocean climate model biases traced to atmospheric model cloud errors, *Nat. Commun.*, 9, 3625, doi:10.1038/s41467-018-05634-2, 2018.
- 1740 Ilyina, T., Six, K. D., Segschneider, J. and Maier-Reimer, E.: Global ocean biogeochemistry model HAMOCC: Model architecture and performance as component of the MPI-Earth system model in different CMIP5 experimental realizations, 5, 287–315, doi:10.1029/2012MS000178, 2013.
- Ito, A.: Mega fire emissions in Siberia: potential supply of bioavailable iron from forests to the ocean, *Biogeosciences*, 8, 1679–1697, doi:10.5194/bg-8-1679-2011, 2011.
- 1745 Ito, A.: Global modeling study of potentially bioavailable iron input from shipboard aerosol sources to the ocean, *Global Biogeochem. Cycles*, 27, 1–10, doi:10.1029/2012GB004378, 2013.
- Ito, A. and Inatomi, M.: Water-use efficiency of the terrestrial biosphere: A model analysis focusing on interactions between the global carbon and water cycles, *J. Hydrometeorol.*, 13(2), 681–694, doi:10.1175/JHM-D-10-05034.1, 2012a.



- Ito, A. and Inatomi, M.: Use of a process-based model for assessing the methane budgets of global terrestrial ecosystems and evaluation of uncertainty, *Biogeosciences*, 9(2), 759–773, doi:10.5194/bg-9-759-2012, 2012b.
- Ito, A. and Oikawa, T.: A simulation model of the carbon cycle in land ecosystems (Sim-CYCLE): A description based on dry-matter production theory and plot-scale validation, *Ecol. Model.*, 151(2–3), 143–176, doi:10.1016/S0304-3800(01)00473-2, 2002.
- Ito, A., Inatomi, M., Huntzinger, D. N., Schwalm, C., Michalak, A. M., Cook, R., King, A. W., Mao, J., Wei, Y., Mac Post, W., Wang, W., Arain, M. A., Huang, S., Hayes, D. J., Ricciuto, D. M., Shi, X., Huang, M., Lei, H., Tian, H., Lu, C., Yang, J., Tao, B., Jain, A., Poulter, B., Peng, S., Ciais, P., Fisher, J. B., Parazoo, N., Schaefer, K., Peng, C., Zeng, N. and Zhao, F.: Decadal trends in the seasonal-cycle amplitude of terrestrial CO₂ exchange resulting from the ensemble of terrestrial biosphere models, *Tellus, Ser. B Chem. Phys. Meteorol.*, 68(1), doi:10.3402/tellusb.v68.28968, 2016.
- Ito, A., Nishina, K. and Noda, H. M.: Impacts of future climate change on the carbon budget of northern high-latitude terrestrial ecosystems: An analysis using ISI-MIP data, *Polar Sci.*, 10(3), 346–355, doi:10.1016/j.polar.2015.11.002, 2016.
- Ito, A., Lin, G. and Penner, J. E.: Radiative forcing by light-absorbing aerosols of pyrogenetic iron oxides, *Sci. Rep.*, 8, 1–11, doi:10.1038/s41598-018-25756-3, 2018.
- Ito, A., Myriokefalitakis, S., Kanakidou, M., Mahowald, N. M., Scanza, R. A., Hamilton, D. S., Baker, A. R., Jickells, T., Sarin, M., Bikkina, S., Gao, Y., Shelley, R. U., Buck, C. S., Landing, W. M., Bowie, A. R., Perron, M. M. G., Guieu, C. and Meskhidze, N.: Pyrogenic iron: The missing link to high iron solubility in aerosols, *Sci. Adv.*, 5, 13–15, doi:10.1126/sciadv.aau7671, 2019.
- Ito, A., Ye, Y., Yamamoto, A., Watanabe, M., and Aita M. N.: Responses of ocean biogeochemistry to atmospheric supply of lithogenic and pyrogenic iron-containing aerosols, *Geol. Mag.*, accepted.
- Jickells, T. D., Baker, A. R., Brooks, N., Liss, P. S., An, Z. S., Cao, J. J., Andersen, K. K., Bergametti, C., Boyd, P. W., Hunter, K. A., Duce, R. A., Kawahata, H., Kubilay, N., Laroche, J., Mahowald, N., Prospero, J. M., Ridgwell, A. J., Tegen, I. and Torres, R.: Global iron connections between desert dust, ocean biogeochemistry, and climate, *Science*, 308(5718), 67–71, 2005.
- Jones, C., Robertson, E., Arora, V., Friedlingstein, P., Shevliakova, E., Bopp, L., Brovkin, V., Hajima, T., Kato, E., Kawamiya, M., Liddicoat, S., Lindsay, K., Reick, C. H., Roelandt, C., Segschneider, J. and Tjiputra, J.: Twenty-first-century compatible CO₂ emissions and airborne fraction simulated by CMIP5 earth system models under four representative concentration pathways, *J. Clim.*, 26(13), 4398–4413, doi:10.1175/JCLI-D-12-00554.1, 2013.
- Jones, C. D., Arora, V., Friedlingstein, P., Bopp, L., Brovkin, V., Dunne, J., Graven, H., Hoffman, F., Ilyina, T., John, J. G., Jung, M., Kawamiya, M., Koven, C., Pongratz, J., Raddatz, T., Randerson, J. and Zaehle, S.: The C4MIP experimental protocol for CMIP6, *Geosci. Model Dev. Discuss.*, (1), 1–52, doi:10.5194/gmd-2016-36, 2016.
- Jung, M., Reichstein, M., Margolis, H. A., Cescatti, A., Richardson, A. D., Arain, M. A., Armeth, A., Bernhofer, C., Bonal, D., Chen, J., Gianelle, D., Gobron, N., Kiely, G., Kutsch, W., Lasslop, G., Law, B. E., Lindroth, A., Merbold, L., Montagnani, L., Moors, E. J., Papale, D., Sottocornola, M., Vaccari, F. and Williams, C.: Global patterns of land–atmosphere fluxes of carbon dioxide, latent heat, and sensible heat derived from eddy covariance, satellite, and meteorological observations, *J. Geophys. Res. Biogeosciences*, 116(3), G00J07, doi:10.1029/2010JG001566, 2011.
- Kaleschke, L., Lupkes, C., Vihma, T., J. H., Bochert, A., Hartmann, J. and Heygster, G.: SSM/I sea ice remote sensing for mesoscale ocean–atmosphere interaction analysis, *Can. J. Remote Sens.*, 27, 526–537, 2001.



- Kattge, J., Knorr, W., Raddatz, T. and Wirth, C.: Quantifying photosynthetic capacity and its relationship to leaf nitrogen content for global-scale terrestrial biosphere models, *Glob. Chang. Biol.*, 15(4), 976–991, doi:10.1111/j.1365-2486.2008.01744.x, 2009.
- 1790 Kawamiya, M., Kishi, M. J. and Suginothara, N.: An ecosystem model for the North Pacific embedded in a general circulation model Part I: Model description and characteristics of spatial distributions of biological variables, *J. Mar. Syst.*, 25, 129–157, 2000.
- Keller, D. P., Oeschlies, A. and Eby, M.: A new marine ecosystem model for the University of Victoria earth system climate model, *Geosci. Model Dev.*, 5(5), 1195–1220, doi:10.5194/gmd-5-1195-2012, 2012.
- 1795 Kennedy, J. J., Rayner, N. A., Smith, R. O., Parker, D. E. and Saunby, M.: Reassessing biases and other uncertainties in sea surface temperature observations measured in situ since 1850: 1. Measurement and sampling uncertainties, *J. Geophys. Res. Atmos.*, 116(14), doi:10.1029/2010JD015218, 2011.
- Kindermann, G. E., McCallum, I., Fritz, S. and Obersteiner, M.: A global forest growing stock, biomass and carbon map based on FAO statistics, *Silva Fenn.*, 42(3), 387–396, 2008.
- 1800 Kobayashi, H. and Oka, A.: Response of atmospheric pCO₂ to glacial changes in the Southern Ocean amplified by carbonate compensation, *Paleoceanogr. Paleoclim.*, 33, 1206–1229, doi:10.1029/2018PA003360, 2018.
- Kosaka, Y. and Xie, S.: The tropical Pacific as a key pacemaker of the variable rates of global warming, *Nat. Geosci.*, 9, 669–674, doi:10.1038/NGEO2770, 2016.
- 1805 Krishnamurthy, A., Moore, J. K., Mahowald, N., Luo, C. and Zender, C. S.: Impacts of atmospheric nutrient inputs on marine biogeochemistry, *J. Geophys. Res.*, 115(G01006), doi:10.1029/2009JG001115, 2010.
- Laufkotter, C., Vogt, M., Gruber, N., Aita-Noguchi, M., Aumont, O., Bopp, L., Buitenhuis, E., Doney, S. C., Dunne, J., Hashioka, T., Hauck, J., Hirata, T., John, J., Le Quere, C., Lima, I. D., Nakano, H., Seferian, R., Totterdell, I., Vichi, M. and Volker, C.: Drivers and uncertainties of future global marine primary production in marine ecosystem models, *Biogeosciences*, 12(23), 6955–6984, doi:10.5194/bg-12-6955-2015, 2015.
- 1810 Lauvset, S. K., Key, R. M., Olsen, A., Heuven, S. van Velo, A., Lin, X., Schirnick, C., Kozyr, A., Tanhua, T., Hoppema, M. and Jutterström, S.: A new global interior ocean mapped climatology : the 1×1 GLODAP version 2, *Earth Syst. Sci. Data*, 8, 325–340, doi:10.5194/essd-8-325-2016, 2016.
- 1815 Lawrence, D. M., Hurtt, G. C., Arneeth, A., Brovkin, V., Calvin, K. V., Jones, A. D., Jones, C. D., Lawrence, P. J., Noblet-Ducoudré, N. De, Pongratz, J., Seneviratne, S. I. and Shevliakova, E.: The Land Use Model Intercomparison Project (LUMIP) contribution to CMIP6: Rationale and experimental design, *Geosci. Model Dev.*, 9(9), 2973–2998, doi:10.5194/gmd-9-2973-2016, 2016.
- 1820 Le Quéré, C., Andrew, R. M., Canadell, J. G., Sitch, S., Korsbakken, J. I., Peters, G. P., Manning, A. C., Boden, T. A., Tans, P. P., Houghton, R. A., Keeling, R. F., Alin, S., Andrews, O. D., Anthoni, P., Barbero, L., Bopp, L., Chevallier, F., Chini, L. P., Ciais, P., Currie, K., Delire, C., Doney, S. C., Friedlingstein, P., Gkritzalis, T., Harris, I., Hauck, J., Haverd, V., Hoppema, M., Klein Goldewijk, K., Jain, A. K., Kato, E., Körtzinger, A., Landschützer, P., Lefèvre, N., Lenton, A., Lienert, S., Lombardozzi, D., Melton, J. R., Metzl, N., Millero, F., Monteiro, P. M. S., Munro, D. R., Nabel, J. E. M. S., Nakaoka, S. I., O’Brien, K., Olsen, A., Omar, A. M., Ono, T., Pierrot, D., Poulter, B., Rödenbeck, C., Salisbury, J., Schuster, U., Schwinger, J., Séférian, R., Skjelvan, I., Stocker, B. D., Sutton, A. J., Takahashi, T., Tian, H., Tilbrook, B.,



- van der Laan-Luijkx, I. T., van der Werf, G. R., Viovy, N., Walker, A. P., Wiltshire, A. J. and Zaehle, S.: Global Carbon Budget 2016, *Earth Syst. Sci. Data*, 8(2), 605–649, doi:10.5194/essd-8-605-2016, 2016.
- LeQuéré, C., Andrew, R., Friedlingstein, P., Sitch, S., Hauck, J., Pongratz, J., Pickers, P., Korsbakken, J. I., Peters, G., Canadell, J., Armeth, A., Arora, V., Barbero, L., Bastos, A., Bopp, L., Ciais, P., Chini, L., Ciais, P., Doney, S., Gkritzalis, T., Goll, D., Harris, I., Haverd, V., Hoffman, F., Hoppema, M., Houghton, R., Hurtt, G., Ilyina, T., Jain, A., Johannessen, T., Jones, C., Kato, E., Keeling, R., Klein Goldewijk, K., Landschützer, P., Lefèvre, N., Lienert, S., Liu, Z., Lombardozzi, D., Metz, N., Munro, D., Nabel, J., Nakaoka, S. I., Neill, C., Olsen, A., Ono, T., Patra, P., Peregon, A., Peters, W., Peylin, P., Pfeil, B., Pierrot, D., Poulter, B., Rehder, G., Resplandy, L., Robertson, E., Rocher, M., Rödenbeck, C., Schuster, U., Skjelvan, I., Séférian, R., Skjelvan, I., Steinhoff, T., Sutton, A., Tans, P., Tian, H., Tilbrook, B., Tubiello, F., van der Laan-Luijkx, I., van der Werf, G., Viovy, N., Walker, A., Wiltshire, A., Wright, R., Zaehle, S. and Zheng, B.: Global Carbon Budget 2018, *Earth Syst. Sci. Data*, 10, 2141–2194, doi:10.5194/essd-10-2141-2018, 2018.
- Levitus, S., Antonov, J. I., Boyer, T. P., Baranova, O. K., Garcia, H. E., Locarnini, R. A., Mishonov, A. V., Reagan, J. R., Seidov, D., Yarosh, E. S. and Zweng, M. M.: World ocean heat content and thermocline sea level change (0–2000 m), 1955–2010, *Geophys. Res. Lett.*, 39(10), 1–5, doi:10.1029/2012GL051106, 2012.
- Lin, B., Sakoda, A., Shibasaki, R., Goto, N. and Suzuki, M.: Modelling a global biogeochemical nitrogen cycle in terrestrial ecosystems, *Ecol. Model.*, 135, 89–110, 2000.
- Locarnini, R. A., Mishonov, A. V., Antonov, J. I., Boyer, T. P., Garcia, H. E., Baranova, O. K., Zweng, M. M., Paver, C. R., Reagan, J. R., Johnson, D. R., Hamilton, M. and Seidov, D.: World Ocean Atlas 2013, Volume 1: Temperature, in Atlas NESDIS 75, edited by A. M. S. Levitus, p. 40, NOAA, US Government Printing Office, Washington DC, USA, 2013.
- Loeb, N. G., Lyman, J. M., Johnson, G. C., Allan, R. P., Doelling, D. R., Wong, T., Soden, B. J. and Stephens, G. L.: Observed changes in top-of-the-atmosphere radiation and upper-ocean heating consistent within uncertainty, *Nat. Geosci.*, 5(2), 110–113, doi:10.1038/ngeo1375, 2012.
- Loeb, N. G., Doelling, D. R., Wang, H., Su, W., Nguyen, C., Corbett, J. G., Liang, L., Mitrescu, C., Rose, F. G. and Kato, S.: Clouds and the Earth’s Radiant Energy System (CERES) Energy Balanced and Filled (EBAF) top-of-atmosphere (TOA) edition-4.0 data product, *J. Clim.*, 31(2), 895–918, doi:10.1175/JCLI-D-17-0208.1, 2018.
- Ma, L., Hurtt, G. C., Chini, L. P., Sahajpal, R., Pongratz, J., Frohling, S., Stehfest, E., Klein Goldewijk, K., O’Leary, D. and Doelman, J. C.: Global transition rules for translating land-use change (LUH2) to land-cover change for CMIP6 using GLM2, *Geosci. Model Dev. Discuss.*, (July), 1–30, doi:10.5194/gmd-2019-146, 2019.
- Mahowald, N. M., Engelstaedter, S., Luo, C., Sealy, A., Artaxo, P., Benitez-Nelson, C., Bonnet, S., Chen, Y., Chuang, P. Y., Cohen, D. D., Dulac, F., Herut, B., Johansen, A. M., Kubilay, N., Losno, R., Maenhaut, W., Paytan, A., Prospero, J. M., Shank, L. M. and Siefert, R. L.: Atmospheric iron deposition: global distribution, variability, and human perturbations, *Ann. Rev. Mar. Sci.*, 1(1), 245–278, doi:10.1146/annurev.marine.010908.163727, 2009.
- Maksyutov, S., Takagi, H., Valsala, V. K., Saito, M., Oda, T., Saeki, T., Belikov, D. A., Saito, R., Ito, A., Yoshida, Y., Morino, I., Uchino, O., Andres, R. J. and Yokota, T.: Regional CO₂ flux estimates for 2009–2010 based on GOSAT and ground-based CO₂ observations, *Atmos. Chem. Phys.*, 13(18), 9351–9373, doi:10.5194/acp-13-9351-2013, 2013.
- Manabe, S. and Bryan, K.: Climate calculations with a combined ocean–atmosphere model, *J. Atmos. Sci.*, 26, 786–789, 1969.



- Manabe, S., Smagorinsky, J. and Strickler, R. F.: Simulated climatology of a general circulation model with a hydrologic cycle, *Mon. Weather Rev.*, 93(12), 769–798, doi:10.1109/TIM.1986.6499065, 1965.
- Martin, J. H. and Gordon, R. M.: Northeast Pacific iron distributions in relation to phytoplankton productivity, *Deep Sea Res.*, 35(2), 177–196, 1988.
- Matthes, K., Funke, B., Andersson, M. E., Barnard, L., Beer, J., Charbonneau, P., Clilverd, M. A., de Wit, T. D., Haberreiter, M., Hendry, A., Jackman, C. H., Kretzschmar, M., Kruschke, T., Kunze, M., Langematz, U., Marsh, D. R., Maycock, A. C., MisiOS, S., Rodger, C. J., Scaife, A. A., Seppälä, A., Shangguan, M., Sinnhuber, M., Tourpali, K., Usoskin, I., van de Kamp, M., Verronen, P. T. and Versick, S.: Solar forcing for CMIP6 (v3.2), *Geosci. Model Dev.*, 10(6), 2247–2302, doi:10.5194/gmd-10-2247-2017, 2017.
- Matthews, H. D., Gillett, N. P., Stott, P. A. and Zickfeld, K.: The proportionality of global warming to cumulative carbon emissions, *Nature*, 459(7248), 829–832, doi:10.1038/nature08047, 2009.
- Mayorga, E., Seitzinger, S. P., Harrison, J. A., Dumont, E., Beusen, A. H. W., Bouwman, A. F., Fekete, B. M., Kroeze, C. and van Drecht, G.: Global Nutrient Export from WaterSheds 2 (NEWS 2): Model development and implementation, *Environ. Model. Softw.*, 25(7), 837–853, doi:10.1016/j.envsoft.2010.01.007, 2010.
- McCalley, C. K. and Sparks, J. P.: Abiotic gas formation drives nitrogen loss from a desert ecosystem, *Science*, 326(5954), 837–841, 2009.
- Meehl, G. A. and Washington, W. M.: Cloud albedo feedback and the super greenhouse effect in a global coupled GCM, *Clim. Dyn.*, 11(7), 399–411, doi:10.1007/BF00209514, 1995.
- Meinshausen, M., Vogel, E., Nauels, A., Lorbacher, K., Meinshausen, N., Etheridge, D. M., Fraser, P. J., Montzka, S. A., Rayner, P. J., Trudinger, C. M., Krummel, P. B., Beyerle, U., Canadell, J. G., Daniel, J. S., Enting, I. G. and Law, R. M.: Historical greenhouse gas concentrations for climate modelling (CMIP6), *Geosci. Model Dev.*, 10, 2057–2116, doi:10.5194/gmd-10-2057-2017, 2017.
- Monsi, M. and Saeki, T.: Über den Lichtfaktor in den Pflanzengesellschaften und seine Bedeutung für die Stoffproduktion, *Japanese J. Bot.*, 14, 22–52, 1953.
- Moore, J. K., Doney, S. C. and Lindsay, K.: Upper ocean ecosystem dynamics and iron cycling in a global three-dimensional model, *Global Biogeochem. Cycles*, 18(4), 1–21, doi:10.1029/2004GB002220, 2004.
- Moore, C. M., Mills, M., Arrigo, K. and Berman-Frank, I.: Processes and patterns of oceanic nutrient limitation, *Nat. Geosci.*, 6, 701–710, *Nat. Geosci.*, 701–710, doi:10.13339/j.cnki.sglc.20150901.022, 2013.
- Moore, J. K. and Braucher, O.: Sedimentary and mineral dust sources of dissolved iron to the world ocean, *Biogeosciences*, 5, 631–656, 2008.
- Morice, C. P., Kennedy, J. J., Rayner, N. A. and Jones, P. D.: Quantifying uncertainties in global and regional temperature change using an ensemble of observational estimates: The HadCRUT4 data set, *J. Geophys. Res.*, 117(D08101), doi:10.1029/2011JD017187, 2012.
- Nitta, T., Yoshimura, K., Takata, K., Oishi, R., Sueyoshi, T., Kanae, S., Oki, T., Abe-Ouchi, A. and Liston, G. E.: Representing variability in subgrid snow cover and snow depth in a global land model: Offline validation, *J. Clim.*, 27(9), 3318–3330, doi:10.1175/JCLI-D-13-00310.1, 2014.



- 1900 Nitta, T., Yoshimura, K. and Abe-Ouchi, A.: Impact of Arctic wetlands on the climate system: Model sensitivity simulations with the MIROC5 AGCM and a snow-fed wetland scheme, *J. Hydrometeorol.*, 18(11), 2923–2936, doi:10.1175/jhm-d-16-0105.1, 2017.
- Niwa, Y., Fujii, Y., Sawa, Y., Iida, Y., Ito, A., Satoh, M., Imasu, R., Tsuboi, K., Matsueda, H. and Saigusa, N.: A 4D-Var inversion system based on the icosahedral grid model (NICAM-TM 4D-Var v1.0) - Part 2: Optimization scheme and identical twin experiment of atmospheric CO₂ inversion, *Geosci. Model Dev.*, 10(6), 2201–2219, doi:10.5194/gmd-10-2201-2017, 2017.
- 1905 Noffke, A., Hensen, C., Sommer, S., Scholz, F., Bohlen, L., Mosch, T. and Graco, M.: Benthic iron and phosphorus fluxes across the Peruvian oxygen minimum zone, *Limnol. Oceanogr.*, 57(3), 851–867, doi:10.4319/lo.2012.57.3.0851, 2012.
- Norby, R. J., Warren, J. M., Iversen, C. M., Medlyn, B. E. and McMurtrie, R. E.: CO₂ enhancement of forest productivity constrained by limited nitrogen availability, *Proc. Natl. Acad. Sci.*, 107(45), 19368–19373, doi:10.1073/pnas.1006463107, 2010.
- 1910 Nozawa, T., Nagashima, T., Shiogama, H. and Crooks, S. A.: Detecting natural influence on surface air temperature change in the early twentieth century, *Geophys. Res. Lett.*, 32, L20719, doi:10.1029/2005GL023540, 2005.
- Numaguti, A., Sugata, S., Takahashi, M., Nakajima, T. and Sumi, A.: Study on the climate system and mass transport by a climate model, *Cent. Glob. Environ. Res. Supercomput. Monogr. Rep.*, 3, 1–48, 1997.
- 1915 Ohgaito, R. and Abe-Ouchi, A.: The effect of sea surface temperature bias in the PMIP2 AOGCMs on mid-Holocene Asian monsoon enhancement, *Clim. Dyn.*, 33(7–8), 975–983, doi:10.1007/s00382-009-0533-8, 2009.
- Ohgaito, R., Sueyoshi, T., Abe-Ouchi, A., Hajima, T., Watanabe, S., Kim, H.-J., Yamamoto, A., and Kawamiya, M.: Can an Earth System Model simulate better climate change at mid-Holocene than an AOGCM? A comparison study of MIROC-ESM and MIROC3, *Clim. Past*, 9, 1519–1542, <https://doi.org/10.5194/cp-9-1519-2013>, 2013.
- 1920 Ono, T., Shiimoto, A. and Saino, T.: Recent decrease of summer nutrients concentrations and future possible shrinkage of the subarctic North Pacific high-nutrient low-chlorophyll region, *Global Biogeochem. Cycles*, 22(3), 1–11, doi:10.1029/2007GB003092, 2008.
- Orr, J. C., Najjar, R. G., Aumont, O., Bopp, L., Bullister, J. L., Danabasoglu, G., Doney, S. C., Dunne, J. P., Dutay, J. C., Graven, H., Griffies, S. M., John, J. G., Joos, F., Levin, I., Lindsay, K., Matear, R. J., McKinley, G. A., Mouchet, A., 1925 Oschlies, A., Romanou, A., Schlitzer, R., Tagliabue, A., Tanhua, T. and Yool, A.: Biogeochemical protocols and diagnostics for the CMIP6 Ocean Model Intercomparison Project (OMIP), *Geosci. Model Dev.*, 10(6), 2169–2199, doi:10.5194/gmd-10-2169-2017, 2017.
- Oschlies, A., Brandt, P., Stramma, L. and Schmidtko, S.: Drivers and mechanisms of ocean deoxygenation, *Nat. Geosci.*, 11(July), 467–473, doi:10.1038/s41561-018-0152-2, 2018.
- 1930 Parton, W. J., Mosier, A. R., Ojima, D. S., Valentine, D. W., Schimel, D. S., Weier, K. and Kulmala, A. E.: Generalized model for N₂ and N₂O production from nitrification and denitrification, *Global Biogeochem. Cycles*, 10(3), 401–412, doi:10.1029/96GB01455, 1996.
- Sanz-Lázaro, C., Valdemarsen, T., Marín, A. and Holmer, M.: Effect of temperature on biogeochemistry of marine organic-enriched systems: implications in a global warming scenario, *Ecol. Appl.*, 21, 2664–2677, 2011.



- 1935 Saunois, M., Bousquet, P., Poulter, B., Peregon, A., Ciais, P., Canadell, J. G., Dlugokencky, E. J., Etiope, G., Bastviken, D., Houweling, S., Janssens-Maenhout, G., Tubiello, F. N., Castaldi, S., Jackson, R. B., Alexe, M., Arora, V. K., Beerling, D. J., Bergamaschi, P., Blake, D. R., Brailsford, G., Brovkin, V., Bruhwiler, L., Crevoisier, C., Crill, P., Covey, K., Curry, C., Frankenberg, C., Gedney, N., Höglund-Isaksson, L., Ishizawa, M., Ito, A., Joos, F., Kim, H. S., Kleinen, T., Krummel, P., Lamarque, J. F., Langenfelds, R., Locatelli, R., Machida, T., Maksyutov, S., McDonald, K. C., Marshall, J., Melton, J.
- 1940 R., Morino, I., Naik, V., O'Doherty, S., Parmentier, F. J. W., Patra, P. K., Peng, C., Peng, S., Peters, G. P., Pison, I., Prigent, C., Prinn, R., Ramonet, M., Riley, W. J., Saito, M., Santini, M., Schroeder, R., Simpson, I. J., Spahni, R., Steele, P., Takizawa, A., Thornton, B. F., Tian, H., Tohjima, Y., Viovy, N., Voulgarakis, A., van Weele, M., van der Werf, G. R., Weiss, R., Wiedinmyer, C., Wilton, D. J., Wiltshire, A., Worthy, D., Wunch, D., Xu, X., Yoshida, Y., Zhang, B., Zhang, Z. and Zhu, Q.: The global methane budget 2000–2012, *Earth Syst. Sci. Data*, 8(2), 697–751, doi:10.5194/essd-8-697-2016,
- 1945 2016.
- Schaeffer, S. M., Billings, S. A. and Evans, R. D.: Responses of soil nitrogen dynamics in a Mojave Desert ecosystem to manipulations in soil carbon and nitrogen availability, *Oecologia*, 134(4), 547–553, doi:10.1007/s00442-002-1130-2, 2003.
- Schmittner, A., Oschlies, A., Giraud, X., Eby, M. and Simmons, H. L.: A global model of the marine ecosystem for long-term simulations: Sensitivity to ocean mixing, buoyancy forcing, particle sinking, and dissolved organic matter cycling, *Global Biogeochem. Cycles*, 19(3), 1–17, doi:10.1029/2004GB002283, 2005.
- Schmittner, A., Oschlies, A., Matthews, H. D. and Galbraith, E. D.: Future changes in climate, ocean circulation, ecosystems, and biogeochemical cycling simulated for a business-as-usual CO₂ emission scenario until year 4000 AD, *Global Biogeochem. Cycles*, 22(1), 1–21, doi:10.1029/2007GB002953, 2008.
- 1955 Seitzinger, S. P., Harrison, J. A., Dumont, E., Beusen, A. H. W. and Bouwman, A. F.: Sources and delivery of carbon, nitrogen, and phosphorus to the coastal zone: An overview of global Nutrient Export from Watersheds (NEWS) models and their application, *Global Biogeochem. Cycles*, 19(4), 1–11, doi:10.1029/2005GB002606, 2005.
- Seitzinger, S. P., Mayorga, E., Bouwman, A. F., Kroeze, C., Beusen, A. H. W., Billen, G., van Drecht, G., Dumont, E., Fekete, B. M., Garnier, J. and Harrison, J. A.: Global river nutrient export : A scenario analysis of past and future trends, *Global Biogeochem. Cycles*, 24(GB0A08), doi:10.1029/2009GB003587, 2010.
- 1960 Sellers, P. J., Mintz, Y., Sud, Y. C. and Dalcher, A.: A simple biosphere model (SiB) for use within general circulation models, *J. Atmos. Sci.*, 43(6), 505–531, 1986.
- Sharples, J., Middelburg, J. J., Fennel, K. and Jickells, T. D.: What proportion of riverine nutrients reaches the open ocean? *Global Biogeochem. Cycles*, 31, 39–58, doi:10.1002/2016GB005483, 2017.
- 1965 Shiozaki, T., Bombar, D., Riemann, L., Sato, M., Hashihama, F., Kodama, T., Tanita, I., Takeda, S., Saito, H., Hamasaki, K. and Furuya, K.: Linkage between dinitrogen fixation and primary production in the oligotrophic South Pacific Ocean, *Global Biogeochem. Cycles*, 32(7), 1028–1044, doi:10.1029/2017GB005869, 2018.
- Smith, S. V., Swaney, D. P., Talaue-McManus, L., Bartley, J. D., Sandhei, P. T., McLaughlin, C. J., Dupra, V. C., Crossland, C. J., Buddemeier, R. W., Maxwell, B. A. and Wulff, F.: Humans, hydrology, and the distribution of inorganic nutrient loading to the ocean, *Bioscience*, 53(3), 235, doi:10.1641/0006-3568(2003)053[0235:hhatdo]2.0.co;2, 2003.
- 1970



- Sokolov, A. P., Kicklighter, D. W., Melillo, J. M., Felzer, B. S., Schlosser, C. A. and Cronin, T. W.: Consequences of considering carbon–nitrogen interactions on the feedbacks between climate and the terrestrial carbon cycle, *J. Clim.*, 21(15), 3776–3796, doi:10.1175/2008JCLI2038.1, 2008.
- 1975 Stocker, T. F., Dahe, Q., Plattner, G.-K., Alexander, L. V., Allen, S. K., Bindoff, N. L., Bréon, F.-M., Church, J. A., Cubash, U., Emori, S., Forster, P., Friedlingstein, P., Talley, L. D., Vaughan, D. G. and Xie, S.-P.: IPCC Technical Summary AR5, *Clim. Chang. 2013 Phys. Sci. Basis. Contrib. Work. Gr. I to Fifth Assess. Rep. Intergov. Panel Clim. Chang.*, doi:10.1017/CBO9781107415324.005, 2013.
- Sudo, K., Takahashi, M., Kurokawa, J. I. and Akimoto, H.: CHASER: A global chemical model of the troposphere I. Model description, *J. Geophys. Res. Atmos.*, 107(17), doi:10.1029/2001JD001113, 2002.
- 1980 Tagliabue, A., Bopp, L., Dutay, J. C., Bowie, A. R., Chever, F., Jean-Baptiste, P., Bucciarelli, E., Lannuzel, D., Remenyi, T., Sarthou, G., Aumont, O., Gehlen, M. and Jeandel, C.: Hydrothermal contribution to the oceanic dissolved iron inventory, *Nat. Geosci.*, 3(4), 252–256, doi:10.1038/ngeo818, 2010.
- Tagliabue, A., Mtshali, T., Aumont, O., Bowie, A. R., Klunder, M. B., Roychoudhury, A. N. and Swart, S.: A global compilation of dissolved iron measurements : focus on distributions and processes in the Southern Ocean, *Biogeosciences*, 9, 2333–2349, doi:10.5194/bg-9-2333-2012, 2012.
- 1985 Tagliabue, A., Aumont, O. and Bopp, L.: The impact of different external sources of iron on the global carbon cycle, *Geophys. Res. Lett.*, 41(3), 10.1002/2013GL059059, doi:10.1002/2013GL059059. Received, 2014.
- Tagliabue, A., Aumont, O., Death, R., Dunne, J. P., Dutkiewicz, S., Galbraith, E., Misumi, K., Moore, J. K., Ridgwell, A., Sherman, E., Stock, C., Vichi, M., Völker, C. and Yool, A.: How well do global ocean biogeochemistry models simulate dissolved iron distributions? *Global Biogeochem. Cycles*, 30, 149–174, doi:10.1002/2015GB005289. Received, 2016.
- 1990 Tagliabue, A., Bowie, A. R., Boyd, P. W., Buck, K. N., Johnson, K. S. and Saito, M. A.: The integral role of iron in ocean biogeochemistry, *Nature*, 543(7643), 51–59, doi:10.1038/nature21058, 2017.
- Takahashi, T., Broecker, W. S. and Langer, S.: Redfield ratio based on chemical data from isopycnal surfaces, *J. Geophys. Res.*, 90(C4), 6907–6924, doi:10.1029/JC090iC04p06907, 1985.
- 1995 Takata, K., Emori, S. and Watanabe, T.: Development of the minimal advanced treatments of surface interaction and runoff, *Glob. Planet. Change*, 38(1–2), 209–222, doi:10.1016/S0921-8181(03)00030-4, 2003.
- Takemura, T., Okamoto, H., Maruyama, Y., Numaguti, A., Higurashi, A. and Nakajima, T.: Global three-dimensional simulation of aerosol optical thickness distribution of various origins, *J. Geophys. Res. Atmos.*, 105(D14), 17853–17873, doi:10.1029/2000JD900265, 2000.
- 2000 Takemura, T., Nozawa, T., Emori, S. and Nakajima, T. Y.: Simulation of climate response to aerosol direct and indirect effects with aerosol transport-radiation model, *J. Geophys. Res.*, 110(D02202), doi:10.1029/2004JD005029, 2005.
- Tatebe, H., Tanaka, Y., Komuro, Y. and Hasumi, H.: Impact of deep ocean mixing on the climatic mean state in the Southern Ocean, *Sci. Rep.*, 8, 14479, doi:10.1038/s41598-018-32768-6, 2018.
- 2005 Tatebe, H., Ogura, T., Nitta, T., Komuro, Y., Ogochi, K., Sudo, K., Sekiguchi, M., Abe, M., Saito, F., Chikira, M., Mori, M., Hirota, N., Kawatani, Y., Mochizuki, T., Yoshimura, K., Takata, K., Ryouta, O., Yamazaki, D., Suzuki, T., Kurogi, M., Kataoka, T., Watanabe, M. and Kimoto, M.: Description and basic evaluation of simulated mean state,



- internal variability, and climate sensitivity, *Geosci. Model Dev.*, 12, 2727–2765, 2019, doi:10.5194/gmd-12-2727-2019, 2019.
- 2010 Thomason, L., Vernier, J., Bourassa, A., Arfeuille, F., Bingen, C. and Peter, T.: Stratospheric Aerosol Data Set (SADS Version 2) Prospectus Larry, [online] Available from: <https://www.wcrp-climate.org/images/modelling/WGCM> (Accessed 7 August 2019).
- Thornley, J. H. M.: Grassland Dynamics, in *Grassland Dynamics: An Ecosystem Simulation Model*, p. 241, CAB International, Wallingford, UK, 1998.
- 2015 Thornton, P. E., Lamarque, J. F., Rosenbloom, N. A. and Mahowald, N. M.: Influence of carbon–nitrogen cycle coupling on land model response to CO₂ fertilization and climate variability, *Global Biogeochem. Cycles*, 21(4), 1–15, doi:10.1029/2006GB002868, 2007.
- Tian, H., Yang, J., Lu, C., Xu, R., Canadell, J. G., Jackson, R. B., Arneeth, A., Chang, J., Chen, G., Ciais, P., Gerber, S., Ito, A., Huang, Y., Joos, F., Lienert, S., Messina, P., Olin, S., Pan, S., Peng, C., Saikawa, E., Thompson, R. L., Vuichard, N., Winiwarter, W., Zaehle, S., Zhang, B., Zhang, K. and Zhu, Q.: The global N₂O model intercomparison project, *Bull. Am. Meteorol. Soc.*, 99(6), 1231–1251, doi:10.1175/BAMS-D-17-0212.1, 2018.
- 2020 Todd-Brown, K. E. O., Randerson, J. T., Post, W. M., Hoffman, F. M., Tarnocai, C., Schuur, E. A. G. and Allison, S. D.: Causes of variation in soil carbon predictions from CMIP5 Earth system models and comparison with observations, *Biogeosciences Discuss.*, 9(10), 14437–14473, doi:10.5194/bg-9-14437-2012, 2012.
- 2025 Todd-Brown, K. E. O., Randerson, J. T., Hopkins, F., Arora, V., Hajima, T., Jones, C., Shevliakova, E., Tjiputra, J., Volodin, E., Wu, T., Zhang, Q. and Allison, S. D.: Changes in soil organic carbon storage predicted by Earth system models during the 21st century, *Biogeosciences*, 11, 2341–2356, doi:10.5194/bg-11-2341-2014, 2014.
- van Marle, M. J. E., Kloster, S., Magi, B. I., Marlon, J. R., Daniiau, A., Field, R. D., Arneeth, A., Forrest, M., Hantson, S., Kehrwald, N. M. and Knorr, W.: Historic global biomass burning emissions for CMIP6 (BB4CMIP) based on merging satellite observations with proxies and fire models (1750–2015), *Geosci. Model Dev.*, 10, 3329–3357, doi:10.5194/gmd-10-3329-2017, 2017.
- 2030 Voosen, P.: New climate models forecast a warming surge, *Science*, 364(6437), 222–223, doi:10.1126/science.364.6437.222, 2019.
- Wang, W., Moore, J. K., Martiny, A. C. and François, W.: Convergent estimates of marine nitrogen fixation, *Nature*, 2035 566, 205–213, doi:10.1038/s41586-019-0911-2, 2019.
- Warszawski, L., Friend, A., Ostberg, S., Frieler, K., Lucht, W., Schaphoff, S., Beerling, D., Cadule, P., Ciais, P., Clark, D. B., Kahana, R., Ito, A., Keribin, R., Kleidon, A., Lomas, M., Nishina, K., Pavlick, R., Rademacher, T. T., Buechner, M., Piontek, F., Schewe, J., Serdeczny, O. and Schellnhuber, H. J.: A multi-model analysis of risk of ecosystem shifts under climate change, *Environ. Res. Lett.*, 8(4), doi:10.1088/1748-9326/8/4/044018, 2013.
- 2040 Watanabe, M., Suzuki, T., O’Ishi, R., Komuro, Y., Watanabe, S., Emori, S., Takemura, T., Chikira, M., Ogura, T., Sekiguchi, M., Takata, K., Yamazaki, D., Yokohata, T., Nozawa, T., Hasumi, H., Tatebe, H. and Kimoto, M.: Improved climate simulation by MIROC5: Mean states, variability, and climate sensitivity, *J. Clim.*, 23(23), 6312–6335, doi:10.1175/2010JCLI3679.1, 2010.



- 2045 Watanabe, S., Hajima, T., Sudo, K., Nagashima, T., Takemura, T., Okajima, H., Nozawa, T., Kawase, H., Abe, M., Yokohata, T., Ise, T., Sato, H., Kato, E., Takata, K., Emori, S. and Kawamiya, M.: MIROC-ESM 2010: Model description and basic results of CMIP5-20c3m experiments, *Geosci. Model Dev.*, 4(4), 845–872, doi:10.5194/gmd-4-845-2011, 2011.
- Wenzel, S., Cox, P. M., Eyring, V. and Friedlingstein, P.: Projected land photosynthesis constrained by changes in the seasonal cycle of atmospheric CO₂, *Nature*, 538, 449–501, doi:10.1038/nature19772, 2016.
- 2050 White, M. A., Thornton, P. E., Running, S. W. and Nemani, R. R.: Parameterization and sensitivity analysis of the BIOME–BGC terrestrial ecosystem model: Net primary production controls, *Earth Interact.*, 4(3), 1–85, doi:10.1175/1087-3562(2000)004<0003:PASAOT>2.0.CO;2, 2000.
- Whitney, F. A., Bograd, S. J. and Ono, T.: Nutrient enrichment of the subarctic Pacific Ocean pycnocline, *Geophys. Res. Lett.*, 40(10), 2200–2205, doi:10.1002/grl.50439, 2013.
- 2055 Wieder, W. R., Cleveland, C. C., Smith, W. K. and Todd-Brown, K.: Future productivity and carbon storage limited by terrestrial nutrient availability, *Nat. Geosci.*, 8(6), 441–444, doi:10.1038/NGEO2413, 2015.
- Wilcox, L. J., Highwood, E. J. and Dunstone, N. J.: The influence of anthropogenic aerosol on multi-decadal variations of historical global climate, *Environ. Res. Lett.*, 8(2), doi:10.1088/1748-9326/8/2/024033, 2013.
- 2060 Yamamoto, A., Shigemitsu, M., Oka, A., Takahashi, K., Ohgaito, R. and Yamanaka, Y.: Global deep ocean oxygenation by enhanced ventilation in the Southern Ocean under long-term global warming, *Global Biogeochem. Cycles*, 1801–1815, doi:10.1002/2015GB005181. Received, 2015.
- Yamamoto, A., Abe-Ouchi, A. and Yamanaka, Y.: Long-term response of oceanic carbon uptake to global warming via physical and biological pumps, *Biogeosciences*, 15(13), 4163–4180, doi:10.5194/bg-15-4163-2018, 2018.
- Yamamoto, A., Abe-Ouchi, A., Ohgaito, R., Ito, A., and Oka, A.: Glacial CO₂ decrease and deep-water deoxygenation by iron fertilization from glaciogenic dust, *Clim. Past*, 15, 981–996, <https://doi.org/10.5194/cp-15-981-2019>, 2019.
- 2065 Yasunaka, S., Ono, T., Nojiri, Y., Whitney, F. A., Wada, C., Murata, A., Nakaoka, S. and Hosoda, S.: Long-term variability of surface nutrient concentrations in the North Pacific, *Geophys. Res. Lett.*, 43(7), 3389–3397, doi:10.1002/2016GL068097, 2016.
- Yoshikawa, C., Kawamiya, M., Kato, T., Yamanaka, Y. and Matsuno, T.: Geographical distribution of the feedback between future climate change and the carbon cycle, *J. Geophys. Res. Biogeosciences*, 113(3), G03002, doi:10.1029/2007JG000570, 2008.
- 2070 Zaehle, S. and Friend, A. D.: Carbon and nitrogen cycle dynamics in the O-CN land surface model: 1. Model description, site-scale evaluation, and sensitivity to parameter estimates, *Global Biogeochem. Cycles*, 24(1), 1–13, doi:10.1029/2009GB003521, 2010.
- 2075 Zaehle, S., Medlyn, B. E., De Kauwe, M. G., Walker, A. P., Dietze, M. C., Hickler, T., Luo, Y., Wang, Y.-P., El-Masri, B., Thornton, P., Jain, A., Wang, S., Warlind, D., Weng, E., Parton, W., Iversen, C. M., Gallet-Budynek, A., McCarthy, H., Finzi, A., Hanson, P. J., Prentice, I. C., Oren, R. and Norby, R. J.: Evaluation of 11 terrestrial carbon–nitrogen cycle models against observations from two temperate Free-Air CO₂ enrichment studies, *New Phytol.*, 202, 803–822, doi:10.1111/nph.12697, 2014.